UNIVERSIDADE FEDERAL DE VIÇOSA

Curvature-Induced Effects on the Skyrmions Motion Along Bent Nanotubes.

Jose Ignacio Costilla Pinedo
Magister Scientiae

VIÇOSA - MINAS GERAIS
2025

JOSE IGNACIO COSTILLA PINEDO

Curvature-Induced Effects on the Skyrmions Motion Along Bent Nanotubes.

Dissertation submitted to the Physics Graduate Program of the Universidade Federal de Viçosa in partial fulfillment of the requirements for the degree of *Magister Scientiae*.

Adviser: Vagson L. de C. Santos

VIÇOSA - MINAS GERAIS
2025

Ficha catalográfica elaborada pela Biblioteca Central da Universidade Federal de Viçosa - Campus Viçosa

T
Costilla Pinedo, José Ignacio, 1996-
C842c
2025

Curvature-induced effects on the skyrmions motion along bent nanotubes / José Ignacio Costilla Pinedo. – Viçosa, MG, 2025.

1 dissertação eletrônica (78 f.): il. (algumas color.).

Texto em inglês.
Inclui apêndices.
Orientador: Vagson Luiz de Carvalho Santos.
Dissertação (mestrado) - Universidade Federal de Viçosa, Departamento de Física, 2025.
Referências bibliográficas: f. 65-69.
DOI: https://doi.org/10.47328/ufvbbt.2026.037
Modo de acesso: World Wide Web.

1. Eletromagnetismo. 2. Modelo de Skyrme. 3. Nanotubos. 4. Curvas. 5. Spintrônica. I. Santos, Vagson Luiz de Carvalho, 1977-. II. Universidade Federal de Viçosa. Departamento de Física. Programa de Pós-Graduação em Física. III. Título.

CDD 22. ed. 539.7546

Bibliotecário(a) responsável: Euzébio Luiz Pinto CRB-6/3317

JOSE IGNACIO COSTILLA PINEDO

Curvature-Induced Effects on the Skyrmions Motion Along Bent Nanotubes.

Dissertation submitted to the Physics Graduate Program of the Universidade Federal de Viçosa in partial fulfillment of the requirements for the degree of *Magister Scientiae*.

APPROVED: September 5, 2025.

Assent:

Jose Ignacio Costilla Pinedo
Author

Vagson Luiz de Carvalho Santos
Adviser

Essa dissertação foi assinada digitalmente pelo autor em 23/02/2026 às 08:18:09 e pelo orientador em 23/02/2026 às 12:43:08. As assinaturas têm validade legal, conforme o disposto na Medida Provisória 2.200-2/2001 e na Resolução nº 37/2012 do CONARQ. Para conferir a autenticidade, acesse https://siadoc.ufv.br/validar-documento. No campo 'Código de registro', informe o código **9GD6.95TQ.TFCU** e clique no botão 'Validar documento'.

I would like to express my gratitude to my family for supporting my decision to pursue this beautiful field of study, which has allowed me to meet wonderful people over the years. Among them, I would especially like to thank Rafael, who gave me great support both personally and academically, and who introduced me to the fascinating world of magnetism.

I am also grateful to my advisor Vagson for all the support he has given me since I arrived in Brazil. I learned a lot under his guidance, and thanks to him, I came to understand that the field of magnetism offers endless possibilities to explore something that motivated me even more to deepen my knowledge in this area.

I would also like to thank Mario Castro, Prof. Dora Altbir, and Prof. Volodymyr Kravchuk for their valuable support throughout this work. I learned things from them that I never imagined I would be able to do, and I am deeply thankful for their teachings and for the patience they showed me.

I am profoundly grateful to my friends from the Department of Physics. From the very beginning, they welcomed me with open arms, making me feel at home. Thank you for all the help, for the outings that allowed me to discover how beautiful Brazil is through its culture, music, and food, and for including me in so many special moments.

And of course, I cannot forget my friends from UNI. With you, it’s always possible to escape from everything: to talk about anything, to laugh for no reason, and to share moments that make life lighter. I especially thank Abel, who has always lent me a hand when I needed it, both in physics and in life.

ACKNOWLEDGMENTS

This work has been sponsored by the following Brazilian research agencies: Coordination for the Improvement of Higher Education Personnel (CAPES; Financing code 001), Minas Gerais State Foundation for Research Aid (FAPEMIG) and National Council of Scientific and Technological Development (CNPq).

An object doesn't have to be large to make a great change.

ABSTRACT

PINEDO, Jose Ignacio Costilla, M.Sc., Universidade Federal de Viçosa, September, 2025. **Curvature-Induced Effects on the Skyrmions Motion Along Bent Nanotubes.**. Adviser: Vagson Luiz de Carvalho Santos.

Traditional storage devices, such as hard disk drives and solid-state drives, face inherent limitations in speed, durability, and energy efficiency. In this context, magnetic skyrmions—topologically stable spin textures that can be manipulated with low energy—have emerged as promising candidates for next-generation memory technologies, such as racetrack memories. However, in planar geometries, the skyrmion Hall effect (SkHE) induces a transverse motion that can drive skyrmions toward device edges, compromising their stability and controllability. In this work, we propose racetrack memories based on bent magnetic nanotubes as an effective strategy to suppress the SkHE through geometric engineering. To this end, we develop a generalized theoretical framework based on an extended Thiele equation that describes current-driven skyrmion dynamics on arbitrarily curved surfaces, incorporating Zhang–Li spin-transfer torque contributions. Our results reveal that, within a certain current regime, the interplay between curvature and current gives rise to an additional curvature-induced contribution that enables the suppression of the SkHE over a broad range of damping and non-adiabaticity parameters. In a different current regime, curvature strongly modifies the skyrmion trajectory, leading to nonlinear dynamical behavior absent in planar systems.

These findings establish curvature as a powerful control parameter for tailoring skyrmion transport beyond what is achievable in planar geometries. The proposed approach provides a robust pathway for designing skyrmion-based spintronic devices with enhanced stability and controllability, paving the way toward high-density, energy-efficient magnetic memory and logic technologies.

Keywords: nanomagnetism; curvilinear magnetism; magnetic nanotubes; skyrmions

RESUMO

PINEDO, Jose Ignacio Costilla, M.Sc., Universidade Federal de Viçosa, setembro de 2025. **Efeitos Induzidos pela Curvatura na Dinâmica de Skyrmions em Nanotubos Dobrados.**. Orientador: Vagson Luiz de Carvalho Santos.

Dispositivos de armazenamento tradicionais, como discos rígidos e unidades de estado sólido, enfrentam limitações relacionadas à velocidade, durabilidade e eficiência energética. Nesse contexto, os skyrmions magnéticos, que são texturas de spin estáveis controláveis com baixa energia, surgiram como candidatos promissores para tecnologias de memória de próxima geração, como a memória racetrack. Contudo, o Efeito Hall do skyrmion faz com que eles se movam lateralmente, correndo o risco de serem aniquilados nas bordas do dispositivo. Isso limita sua estabilidade e controlabilidade em dispositivos planos. Neste trabalho, propomos memórias racetrack baseadas em nanotubos magnéticos curvos como uma estratégia eficaz para suprimir o SkHE por meio de engenharia geométrica. Para isso, desenvolvemos um arcabouço teórico generalizado baseado em uma equação de Thiele estendida, que descreve a dinâmica de skyrmions acionados por corrente em superfícies arbitrariamente curvas, incorporando as contribuições do torque de transferência de spin de Zhang–Li. Nossos resultados revelam que, em um determinado regime de corrente, a interação entre curvatura e corrente dá origem a uma contribuição adicional induzida pela curvatura, permitindo a supressão do SkHE em uma ampla faixa de parâmetros de amortecimento e não adiabaticidade. Em um regime de corrente distinto, a curvatura modifica fortemente a trajetória do skyrmion, levando a um comportamento dinâmico não linear ausente em sistemas planares.

Esses resultados estabelecem a curvatura como um poderoso parâmetro de controle para ajustar o transporte de skyrmions além do que é possível em geometrias planares. A abordagem proposta fornece um caminho robusto para o projeto de dispositivos spintrônicos baseados em skyrmions com maior estabilidade e controlabilidade, abrindo caminho para o desenvolvimento de tecnologias de memória e lógica magnéticas de alta densidade e baixo consumo de energia.

Palavras-chave: nanomagnetismo; magnetismo curvilíneo; nanotubos magnéticos; skyrmions

List of Abbreviations

HDDs	Hard disk drives
SSDs	Solid-state drives
SkHE	Skyrmion Hall effect
SOC	Spin-orbit coupling
STT	Spin-transfer torque
LLG	Landau-Lifshitz-Gilbert
AD	Adiabatic
nAD	Non-adiabatic
DMI	Dzyaloshinskii-Moriya Interaction
FDM	Finite difference method
FEM	Finite element method

Contents

Chapter 1

Introduction

Today, the world produces and stores more digital information than ever before. With the rapid development of artificial intelligence, data centers are under enormous pressure to store, access, and manage massive volumes of data in real time [1]. These centers use traditional memory technologies, such as hard disk drives (HDDs) and solid-state drives (SSDs), sharing a common principle: the detection and manipulation of electron charge.

However, these conventional devices present significant limitations: HDDs and SSDs offer limited long-term durability, and both consume substantial power while providing limited scalability. Therefore, the search for faster, more energy-efficient, and more compact data storage solutions has become a topic of growing importance.

One promising candidate is spintronics [2], a field that uses the intrinsic spin of the electron. Exploiting spin-based mechanisms allows for low-energy, non-volatile data storage and manipulation. In this context, topological spin textures, such as magnetic skyrmions, have emerged as strong candidates for next-generation memory devices [3, 4]. Discovered experimentally in 2009 [5], skyrmions are nanoscale, stable, particle-like magnetic configurations that can be manipulated using spin-polarized currents with remarkably low energy consumption [6]. These unique properties make skyrmions promising candidates for next-generation memory technologies, particularly in racetrack memories , a concept initially proposed by Parkin [7]. Unlike conventional HDDs, which depend on the rotation of magnetic disks and the movement of mechanical read/write heads, racetrack memories employ fixed magnetic nanowires along with stationary read/write ports. This design provides several advantages: enhanced mechanical robustness, significantly faster access times (approximately 10–100 nanoseconds, compared to milliseconds for HDDs and microseconds for FLASH memory), and the potential for higher data storage density through the integration of nanowire arrays [8].

However, a skyrmion cannot move strictly along the driving current direction because it experiences a Magnus force that deflects its trajectory during motion [9, 10]. This phenomenon, known as the skyrmion Hall effect (SkHE), can drive skyrmions into the edges of nanotracks where they may be annihilated, complicating the implementation of skyrmion-based devices.

One route to overcome this limitation is the exploration of magnetism in curved geometries. Curvature offers a powerful way to modify conventional functionalities or even create new ones through geometric design. For magnetic materials, for instance, curvature leads to emergent anisotropic and chiral effects [11, 12] that can act as enhanced stability of skyrmionic textures [13–15]. In closed curved geometries, such as magnetic cylinders [16], skyrmions are no longer subject to edge-induced annihilation, even in the presence of the SkHE. However, while this configuration prevents annihilation due to its periodicity, it does not suppress the SkHE. Instead, the skyrmion exhibits a helical trajectory around the tube, which still limits controllability. Moreover, this setup does not fully leverage the potential of three-dimensional integration, reducing information density and device scalability. To overcome this limitation, racetrack-like memory devices based on bent magnetic nanotubes are proposed in this work. These offer two key advantages (i) a genuine suppression of the SkHE, and (ii) increased storage capacity by enabling more compact and stable 3D skyrmion configurations.

With the intention of optimizing this racetrack proposal, it is necessary to develop a generalized theoretical model capable of predicting the motion of skyrmions in curved geometries. This involves deriving a generalized Thiele equation that incorporates the Zhang–Li spin-transfer torque for arbitrary geometries, a theoretical framework that does not yet exist. An essential part of this work is understanding how curvature influences the Zhang–Li torque, in particular how spin-polarized currents interact with curved surfaces and affect skyrmion dynamics. This forms the main motivation for this thesis.

In this chapter 1, we introduce magnetic skyrmions and discuss the concept of topological charge, as well as previous studies on skyrmions in curved surfaces. In chapter 2 we present the fundamental theoretical framework required to understand this work. We describe the micromagnetic model and the interactions considered in our study within this framework, as well as the Landau–Lifshitz–Gilbert equation with the Zhang-Li spin-transfer torque to describe the magnetization dynamics. In Chapter 3, we present an introduction to differential geometry applied to magnetism with the aim of studying skyrmions on curved surfaces, and we develop how the energy terms are modified under such geometries. In chapter 4 we present the theoretical model that describes curved nanotubes, as well as the planar approximation, which facilitates the analytical understanding of our results. In Chapter 5, we derive the generalized Thiele equation including the Zhang-Li spin-transfer torque, and we also discuss the differences compared to the flat system. In Chapter 6, we discuss the results. Chapter 7 presents the conclusions and future perspectives. Additionally, Appendix A presents the calculation of skyrmion energy in a bent nanotube, while Appendix B provides the calculation of tensors involved in the Thiele equation.

1.1 Magnetic skyrmion: topological properties

Magnetic skyrmions are non-collinear spin configurations characterized by localized swirling patterns of the magnetization. In magnetic systems, a skyrmion is a small, circular region where the magnetic moments form a swirling pattern that differs from the surrounding magnetization. As you move outward from the center, the direction of the magnetic moments gradually rotates, completing a full 360° turn in a consistent direction, as illustrated in Fig. 1.1.

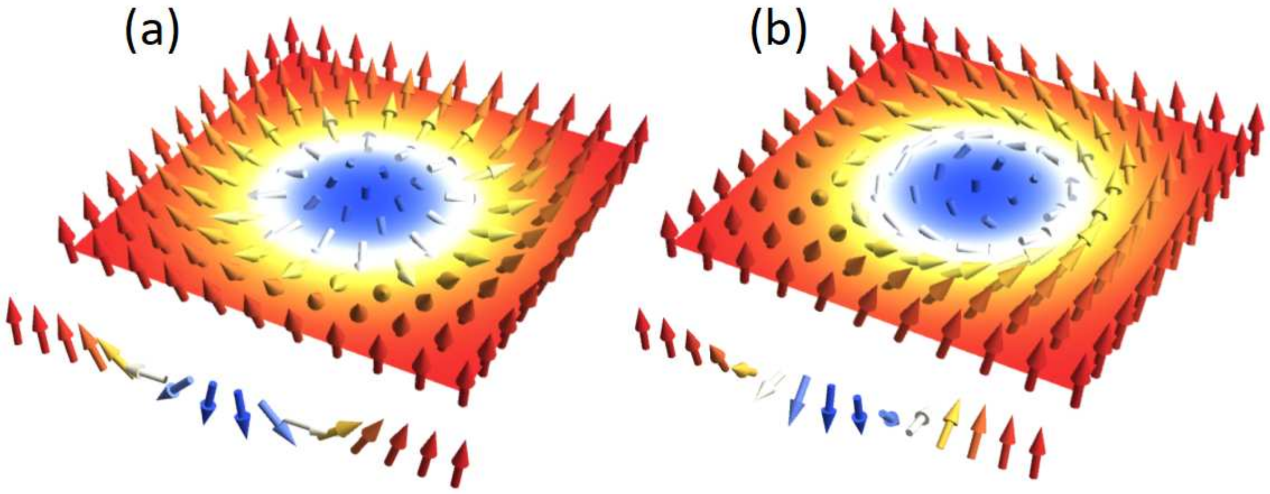

Fig. 1.1: (a) Néel skyrmion, where the spins rotate radially from the center to the edge. (b) Bloch skyrmion, where the magnetization rotates tangentially.

A skyrmion's swirling spin texture is defined by its topological charge N_{sk}, given by [9]

$$N_{sk} = \frac{1}{4\pi} \int \int \boldsymbol{m} \cdot \left(\frac{\partial \boldsymbol{m}}{\partial x} \times \frac{\partial \boldsymbol{m}}{\partial y} \right) \, dxdy. \tag{1.1}$$

This equation mean that unit magnetic vector $\boldsymbol{m}$ evolves in the unit sphere S^2. In other words, the topological charge $N_{\mathrm{sk}} = 0, \pm 1, \pm 2, \ldots,$ is quantised, meaning each value corresponds to a different homotopy class [17]. Magnetic textures within the same homotopy class can be smoothly transformed into one another, but not into textures from a different class. For instance, a skyrmion with a topological charge of $N_{\mathrm{sk}} = \pm 1$ cannot be gradually changed into a uniformly magnetized state, which has a trivial topology of $N_{\mathrm{Sk}} = 0$.

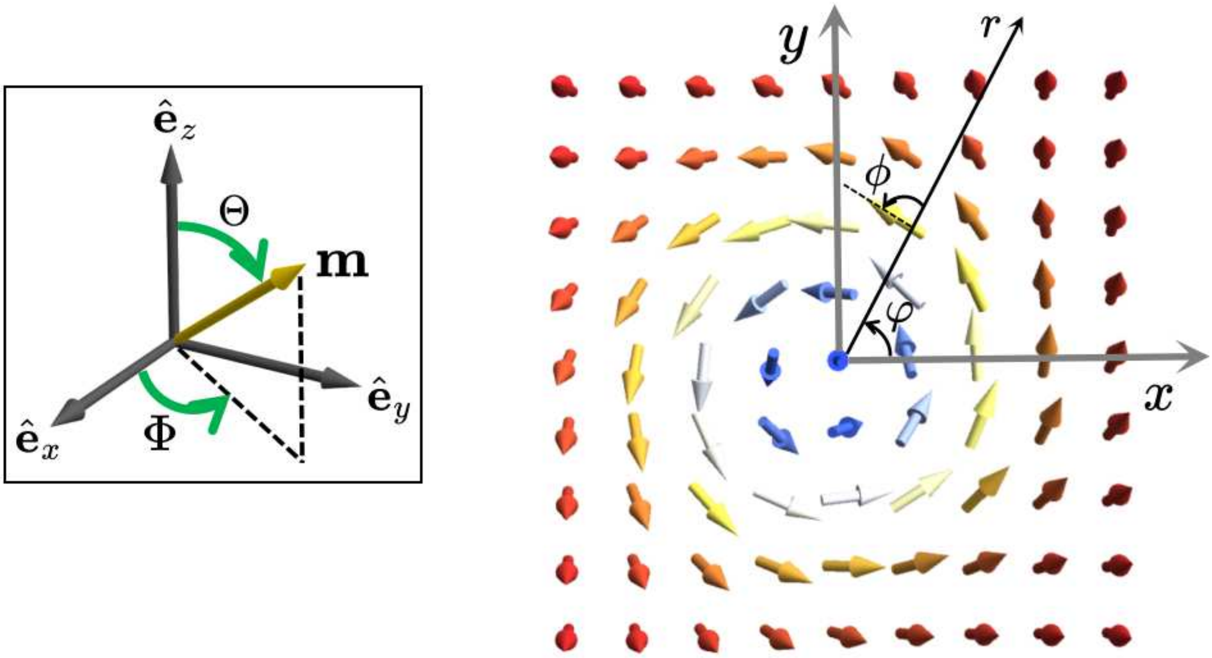

Fig. 1.2: Definition of the magnetization by (Θ, Φ) and top view of a skyrmion with helicity ϕ and core polarity $p = 1$.

In order to classify magnetization textures, we describe the unit magnetic vector $\boldsymbol{m}$ as a function of position in polar coordinates (r, φ). To simplify the analysis, we center the skyrmion at the origin of the coordinate system, as shown in Fig. 1.2. In this system, the spatial coordinates are given by $x = r\cos\varphi$, $y = r\sin\varphi$, and $z = z$. The rotation of the magnetization within the skyrmion is described using spherical coordinates as $\boldsymbol{m} = (m_x, m_y, m_z) = (\cos\Phi(\varphi)\sin\Theta(r), \sin\Phi(\varphi)\sin\Theta(r), \cos\Theta(r))$, where $\Theta(r)$ represents the radial variation of the polar angle and $\Phi(\varphi)$ determines the azimuthal dependence of the magnetization orientation. If we substitute this magnetization into Eq. (1.1), we obtain

$$N_{sk} = \frac{1}{4\pi}\int_0^\infty \sin\Theta \frac{\partial\Theta}{\partial r} \int_0^{2\pi} \frac{\partial\Phi}{\partial\varphi}\, d\varphi = \frac{1}{4\pi}[-\cos\Theta(r)]_0^\infty [\Phi(\varphi)]_0^{2\pi} = p\cdot Q, \tag{1.2}$$

where p is defined as the polarity of the skyrmion core and Q as the vorticity. Since $\cos\Theta = m_z$, then

$$p = \frac{1}{2}[m_z(0) - m_z(\infty)] = \pm 1, \tag{1.3}$$

$$Q = \frac{1}{2\pi}[\Phi(\varphi)]_0^{2\pi}. \tag{1.4}$$

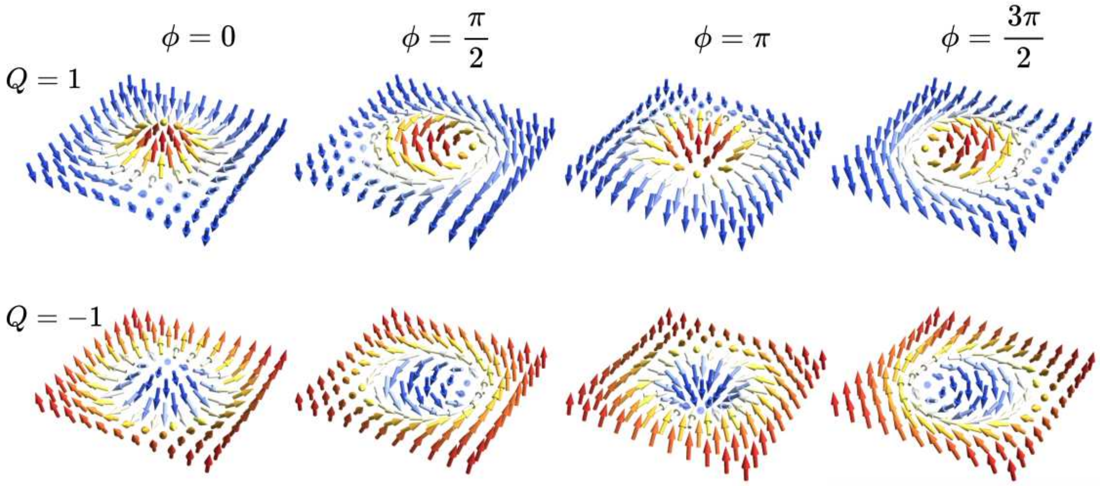

Fig. 1.3: The classification of skyrmions is illustrated using arrows to indicate the spin direction, while the color represents the out-of-plane component of the spin red corresponds to spins pointing out of the plane, white indicates in-plane spins, and blue represents spins directed into the plane.

This mean that the topological number is the product of these two terms, p and Q. If we consider that the magnetization vectors point in the $+z$ direction as $r \to \infty$, while at the center ($r = 0$) they are oriented along the $-z$ direction, then $p = -1$. In the opposite case, $p = 1$. This suggests that the value of p depends on the direction of the magnetic moment at the center of the skyrmion. On the other hand, Q indicates how many times the magnetization wraps the unit sphere. This means that a magnetic skyrmion is characterized by $Q = 1$. However, there are several possibilities for the value of $\Phi(\varphi)$, which means that different magnetic textures can still wrap the unit sphere. To distinguish between these different configurations, it is necessary to introduce an important quantity: the helicity ϕ of the skyrmion.

The helicity defines the phase shift that appears in the expression for $\Phi(\varphi)$, which is given by [9]

$$\Phi(\varphi) = Q\varphi + \phi. \tag{1.5}$$

The helicity determines the characteristic helical shape of the magnetic moments rotating inside the skyrmion structure and describes how the spins are twisted within it. This can be seen in Fig.1.3.

1.2 Skyrmion in curved surfaces

To generate and stabilize skyrmions in thin layered films for practical applications in data storage and processing devices, it is essential to induce an intrinsic Dzyaloshinskii–Moriya interaction (DMI), which favors non-collinear spin configurations.

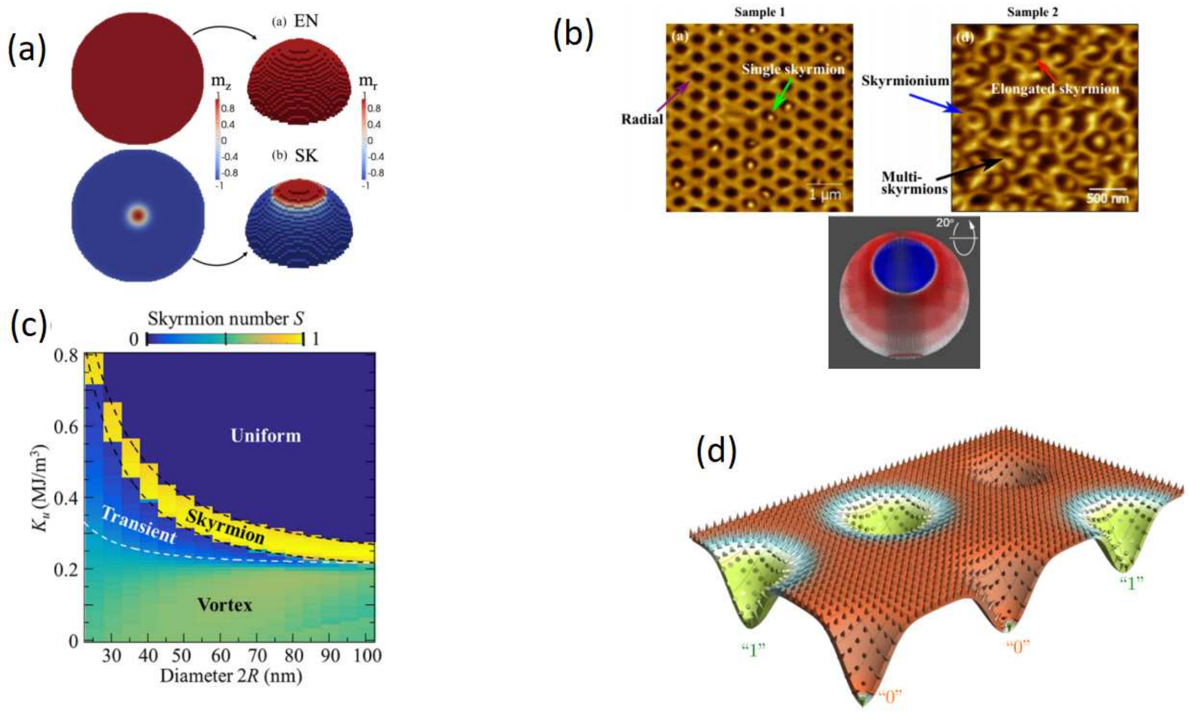

Fig. 1.4: (a) Schematic of the radial magnetization profile within a dome-shaped structure. (b) Experimental observations of various skyrmion states, including single skyrmions, skyrmioniums, multi-skyrmions, and elongated skyrmions. (c) Phase diagram showing the stability of different magnetic configurations as a function of diameter and anisotropy. (d) Schematic of curvature-induced energy landscape with spatially localized skyrmion states representing logic bits ("1" and "0"). Figure adapted from [13, 15, 18, 19]

However, in two-dimensional planar thin films with perpendicular magnetic anisotropy (PMA), the DMI strength is generally limited to values below approximately 2 mJ m^{-2} [18].

One of the most interesting properties of curved magnetic systems is the emergence of curvature-induced anisotropy and extrinsic Dzyaloshinskii–Moriya interaction (DMI), which significantly enhances skyrmion stability. In this context, Carvalho-Santos *et al.* [13] demonstrated that the mean curvature of a surface can induce an extrinsic DMI, leading to improved skyrmion stability, as illustrated in Fig. 1.4(a).

Experimentally, Dugato *et al.* [15] showed that geometric curvature enables the spontaneous formation of isolated skyrmions and mixed skyrmionic phases at room temperature in symmetric Pt/Co/Pt multilayer hemispherical shells, even in the absence of external magnetic fields, as shown in Fig. 1.4(b).

Similarly, Yang *et al.* [18] demonstrated that skyrmions can be stabilized in hemispherical shells within a specific range of perpendicular magnetic anisotropy, despite the absence of both intrinsic DMI and external magnetic fields, as depicted in Fig. 1.4(c).

Furthermore, Kravchuk *et al.* [19] reported that curvilinear defects in magnetic thin films can stabilize multiple skyrmion states with different radii, enabling the encoding of binary information in the form of localized bits, as illustrated in Fig. 1.4(d).

Chapter 2

Fundamentals of the micromagnetism

This chapter provides an overview of the fundamental principles of micromagnetism. It also offers a brief introduction and review of key concepts essential to the study of magnetic skyrmions.

2.1 Micromagnetic model

The exchange length, which defines the typical scale over which atomic magnetic moments vary, is usually on the order of 10 nm and is significantly larger than the interatomic distance (approximately 2–3 Å). This large separation of scales allows the magnetization in ferromagnetic materials to be described by the magnetization vector $\boldsymbol{M}(x, y, z)$, a smoothly varying unit vector field that represents the local orientation of the magnetization in space.

This scale separation forms the basis of the micromagnetic model [20], which is based on the assumption that in ferromagnetic transition metals, such as cobalt (Co), iron (Fe), nickel (Ni), the magnitude of atomic magnetic moments is essentially fixed, with only their direction allowed to vary. As illustrated in Fig. 2.1 (a), this transition allows one to move from a discrete atomic-scale description, where the classical spins $\boldsymbol{S}_i$ are confined to individual atoms, to a continuous micromagnetic representation shown in Fig. 2.1 (b).

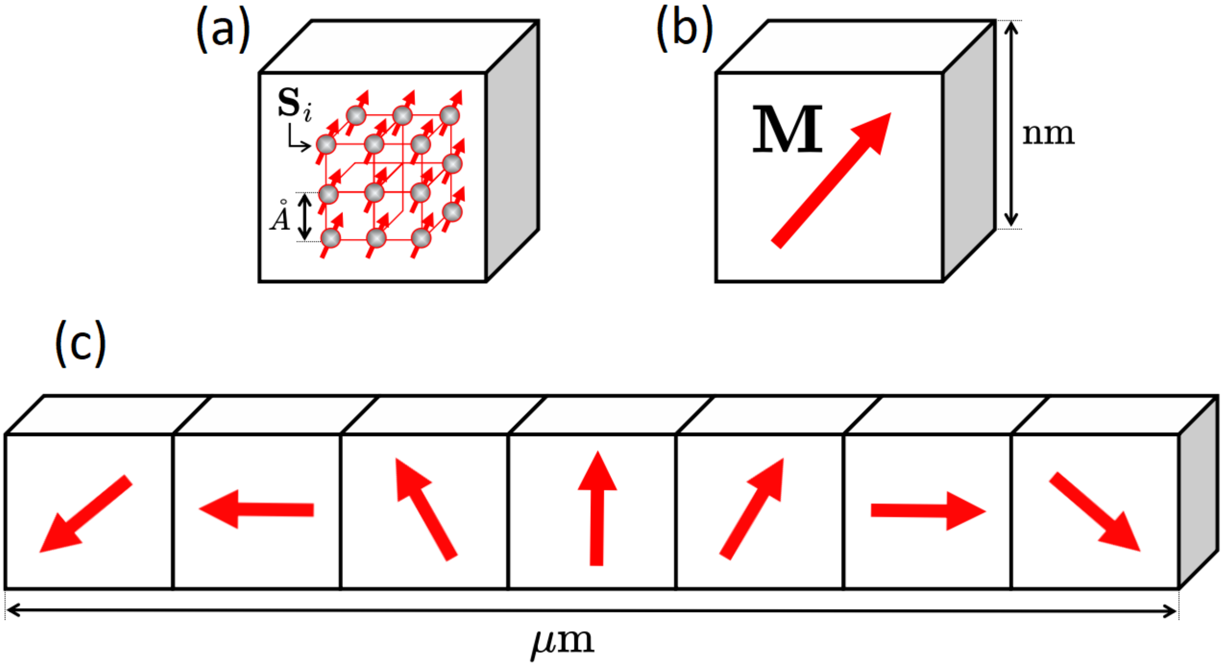

Fig. 2.1: Illustration of scale transition in micromagnetism. (a) Classical spins $\boldsymbol{S}_i$ defined on a crystal lattice (angstrom scale). (b) Averaged magnetization vector $\boldsymbol{M}$ in a micromagnetic cell (nanometer scale). (c) Smooth magnetization texture described by $\boldsymbol{M}(\mathbf{r})$ across space (micrometer scale).

The continuous vector field $\boldsymbol{M}(\mathbf{r})$ can be written in terms of the unit magnetic vector $\boldsymbol{m}$ as

$$\boldsymbol{M}(\mathbf{r}) = M_s\,\boldsymbol{m}, \tag{2.1}$$

where M_s is the saturation magnetization.

This continuous model allows us to employ differential equations that describe the interactions between neighboring magnetic moments. As shown in Fig. 2.1 (c), this framework enables the resolution and analysis of complex magnetization textures and their dynamics over mesoscopic regions. Moreover, it provides a natural way to define the various energy contributions that govern the magnetic state of the system. By expressing the total magnetic energy as a functional of vector $\boldsymbol{m}(x, y, z)$, numerical methods can then be applied to determine equilibrium configurations.

2.2 Micromagnetic interactions

The magnetic energy density terms can then be expressed in terms of the components of the unit magnetic vector $\boldsymbol{m}$ and their spatial derivatives. These expressions are derived from the original Hamiltonian that describes the magnetic interactions. In what follows, we describe the main micromagnetic energy contributions that determine the behavior of the magnetization field. These include the exchange interaction, the DMI and magnetic anisotropy, each playing a distinct role in determining the structure and dynamics of magnetic skyrmions.

2.2.1 Exchange interaction

The exchange interaction is generally the strongest magnetic interaction in ferromagnetic materials. It originates from the combined effect of the quantum-mechanical nature of electrons and their Coulomb interaction. Within the Heisenberg model, the exchange energy is described by the Hamiltonian [21]:

$$\mathcal{H}_{\text{ex}} = -\sum_{i>j} J_{ij}\, \mathbf{S}_i \cdot \mathbf{S}_j, \tag{2.2}$$

where $\mathbf{S}_i$ and $\mathbf{S}_j$ denote the classical spin vectors located at lattice sites i and j, respectively, and J_{ij} is the exchange interaction constant between them. A positive exchange constant ($J_{ij} > 0$) favors a parallel alignment of spins, corresponding to a ferromagnetic state, whereas a negative exchange constant ($J_{ij} < 0$) favors an antiparallel alignment, leading to an antiferromagnetic state. The summation over $i > j$ ensures that each spin pair is counted only once.

To establish a connection with micromagnetic theory, we consider the continuum limit of the discrete Heisenberg model. We assume that the exchange interaction is restricted to nearest-neighbor spins and that the exchange constant takes a uniform value $J_{ij} = J$ for such pairs, while it vanishes otherwise [21]. Furthermore, we focus on the ferromagnetic regime, in which neighboring spins are nearly aligned and the angle ϕ_{ij} between them is small ($\phi_{ij} \ll 1$). Under these assumptions, the scalar product between neighboring spins can be written as

$$\mathbf{S}_i \cdot \mathbf{S}_j = S^2 \cos\phi_{ij}. \tag{2.3}$$

For small angular deviations, the cosine can be expanded to second order,

$$\cos\phi_{ij} \simeq 1 - \frac{\phi_{ij}^2}{2}. \tag{2.4}$$

Substituting this expression into the exchange Hamiltonian, the exchange energy E_{ex} is given by

$$E_{\text{ex}} \simeq \frac{JS^2}{2} \sum_{\langle i,j \rangle} \phi_{ij}^2. \tag{2.5}$$

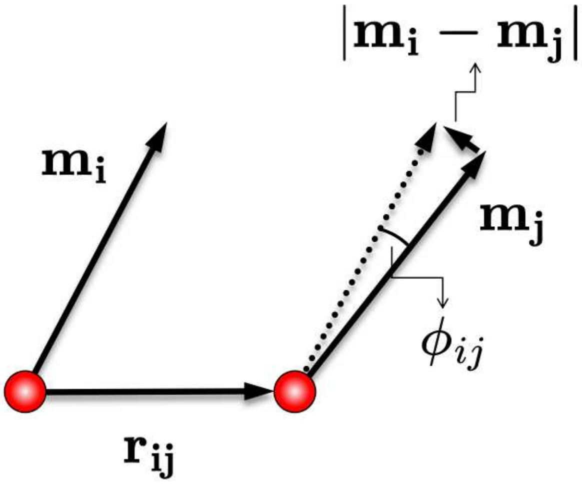

Fig. 2.2: Schematic of neighboring reduced magnetization vectors $\boldsymbol{m}_i$ and $\boldsymbol{m}_j$ separated by $\boldsymbol{r}_{ij}$ and enclosing a small angle ϕ_{ij}, illustrating the continuum approximation. Figure adapted from [21].

As illustrated in Fig. 2.2, the reduced magnetization vectors $\boldsymbol{m}_i$ and $\boldsymbol{m}_j$ at neighboring lattice sites, separated by the vector $\boldsymbol{r}_{ij}$, enclose a small angle ϕ_{ij}. In the ferromagnetic regime, where neighboring spins are nearly aligned, the angular difference between them can be approximated as

$$\phi_{ij} \simeq |\boldsymbol{m}_i - \boldsymbol{m}_j|. \tag{2.6}$$

In the limit of slowly varying magnetization, this difference between the two unit vectors can be further expressed as

$$|\boldsymbol{m}_i - \boldsymbol{m}_j| \simeq |(\boldsymbol{r}_{ij} \cdot \nabla)\boldsymbol{m}|. \tag{2.7}$$

Assuming that the magnetization varies slowly in space, the difference between neighboring sites can be expressed as

$$\boldsymbol{m}_j \simeq \boldsymbol{m}_i + (\boldsymbol{r}_{ij} \cdot \nabla)\boldsymbol{m}, \tag{2.8}$$

which leads to

$$\phi_{ij} \simeq |(\boldsymbol{r}_{ij} \cdot \nabla)\boldsymbol{m}|. \tag{2.9}$$

Replacing Eq. (2.9) into Eq. (2.5), the micromagnetic exchange energy is obtained as

$$E_{\text{ex}} = \int_V A\left[(\nabla m_x)^2 + (\nabla m_y)^2 + (\nabla m_z)^2\right] \, \mathrm{d}V. \tag{2.10}$$

Here, A is the micromagnetic exchange stiffness, which depends on the microscopic exchange constant J and the lattice geometry. For a Bravais lattice with nearest-neighbor distance a and coordination number z, it is given by [21]

$$A = \frac{JS^2 z}{2a}. \tag{2.11}$$

For transition metals such as Co, Fe, and Ni, the exchange stiffness constant A typically lies in the range of 5–30 pJ·m^{-1} [22].

2.2.2 Dzyaloshinskii–Moriya interaction

The Dzyaloshinskii–Moriya interaction originates from spin–orbit coupling (SOC) [23, 24]. This interaction arises in systems with chiral crystal structures, such as FeGe, where it is referred to as bulk DMI, as illustrated in Fig. 2.3(a) [5]. It can also emerge at the interface between a thin ferromagnetic film and a heavy metal layer, such as in the Co/Pt system, where it is known as interfacial DMI, as shown in Fig. 2.3(b) [10].

As a consequence of the competition between the exchange interaction, magnetic anisotropy, dipolar effects, and DMI, neighboring magnetic moments may cant at specific angles with respect to each other. In bulk chiral magnets, this mechanism favors the stabilization of Bloch-type skyrmions, whereas in ultrathin films with interfacial DMI it leads to the formation of Néel-type skyrmions.

The general form of the DMI can be derived from the atomic-scale DMI Hamiltonian [24, 25]. In this description, the interaction between neighboring spins is written as

$$\mathcal{H}_{\mathrm{DMI}} = -\frac{1}{2} \sum_{i,j} \boldsymbol{d}_{i,i+j} \cdot (\boldsymbol{S}_i \times \boldsymbol{S}_{i+j}). \tag{2.12}$$

Here, $\boldsymbol{S}_i$ denotes a classical spin vector at lattice site i of a three-dimensional cubic lattice. The index j labels the displacement vectors connecting site i to its nearest neighbors, and $\boldsymbol{d}_{i,i+j}$ is the Dzyaloshinskii–Moriya interaction vector associated with the bond between sites i and $i + j$, whose direction depends on the crystallographic symmetry of the non-centrosymmetric material [25].

Within the micromagnetic approximation, the DMI energy for an interfacial (Néel-type) configuration can be written as [26]

$$E_{\mathrm{DMI}}^{(i)} = \int D^{(i)} \left[m_z (\nabla \cdot \boldsymbol{m}) - (\boldsymbol{m} \cdot \nabla) m_z \right] \, dV, \tag{2.13}$$

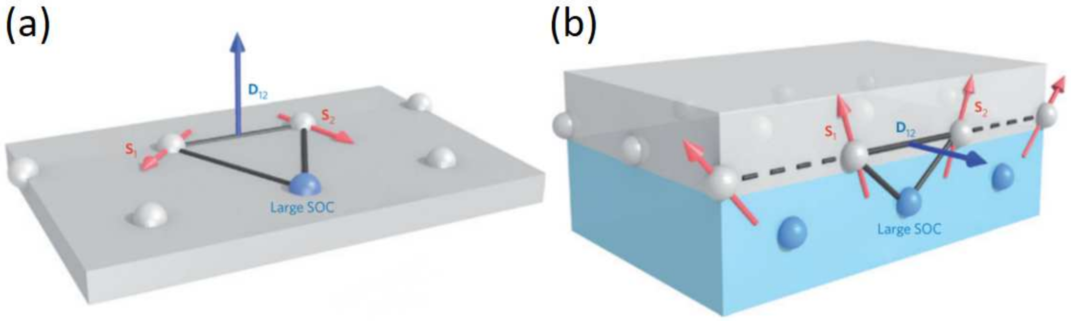

Fig. 2.3: Illustrations of (a) DMI in bulk crystals and (b) DMI at interfaces. Figure adapted from [8].

while for a bulk (Bloch-type) DMI, the corresponding energy takes the form

$$E_{DM}^{(b)} = \int D^{(b)} \ \boldsymbol{m} \cdot (\nabla \times \boldsymbol{m}) \ dV. \tag{2.14}$$

Here, $D^{(\mathrm{i})}$ and $D^{(\mathrm{b})}$ (in $\mathrm{J\,m^{-2}}$) denote the micromagnetic DMI constants for the interfacial and bulk cases, respectively, and m_z is the out-of-plane component of the reduced magnetization vector $\boldsymbol{m}$. For Co/Pt systems, typical values of the interfacial DMI constant lie in the range $D^{(\mathrm{i})} \simeq 1\text{–}3\ \mathrm{mJ\,m^{-2}}$ [27].

2.2.3 Magnetic anisotropy

Magnetic anisotropy is defined as the energy cost required to rotate the magnetization from the easy axis direction to any other direction. Magnetic anisotropy represents the tendency of the magnetization to align along specific fixed directions within a material and arises from spin-orbit interactions in the crystal lattice [21]. These preferred directions are known as easy axes, and the corresponding energy term is minimized when the magnetization aligns with them. For materials such as Fe, Co, and Ni, the anisotropy is uniaxial.

Within the micromagnetic framework, the uniaxial magnetic anisotropy energy in a material of volume V is given by

$$E_{ani} = \int_V K_u \left(1 - (\boldsymbol{m} \cdot \boldsymbol{u}_K)^2\right) dV, \tag{2.15}$$

where K_u (in $\mathrm{Jm^{-3}}$) is the anisotropy constant and $\boldsymbol{u}_K$ is the unit vector along the anisotropy axis.

In addition to this, another important contribution to the total energy is the demagnetization energy, which arises from magnetic charges induced by the divergence of the magnetization at surfaces or interfaces. In systems with small thickness, the presence of demagnetizing fields leads to a redefinition of the anisotropy through an effective anisotropy constant:

$$K = K_u - \frac{1}{2}\mu_0 M_s^2, \tag{2.16}$$

where μ_0 is the vacuum permeability.

2.3 Landau-Lifshitz-Gilbert equation

The Landau–Lifshitz–Gilbert (LLG) equation is a differential equation that describes the precessional dynamics of the magnetization vector in a magnetic system and is given by [28, 29]

$$\frac{\partial \boldsymbol{m}}{\partial t} = -\gamma \boldsymbol{m} \times \boldsymbol{H}_{\text{eff}} + \alpha \boldsymbol{m} \times \frac{\partial \boldsymbol{m}}{\partial t}. \tag{2.17}$$

Here, γ denotes the gyromagnetic ratio, α is the Gilbert damping constant, and $\boldsymbol{H}_{\text{eff}}$ represents the effective magnetic field acting on the magnetization. $\boldsymbol{H}_{\text{eff}} = -\mu_0^{-1}\partial E/\partial \mathbf{m}$ is the effective field and α is the phenomenological (dimensionless) Gilbert damping constant. For Co/Pt systems, the damping parameter has been reported to be close to $\alpha \approx 0.02$ [30]. This value can be modified by focused ion-beam irradiation [31] and allows for studies on damping variations [32].

Figure 2.4 illustrates the contributions of LLG equation. The first term on the right-hand side represents the precessional torque, which is responsible for the rotation of the magnetization $\boldsymbol{m}$ around the effective field $\boldsymbol{H}_{\text{eff}}$. The second term on the right-hand side corresponds to the damping torque, which drives the magnetization toward alignment with $\boldsymbol{H}_{\text{eff}}$.

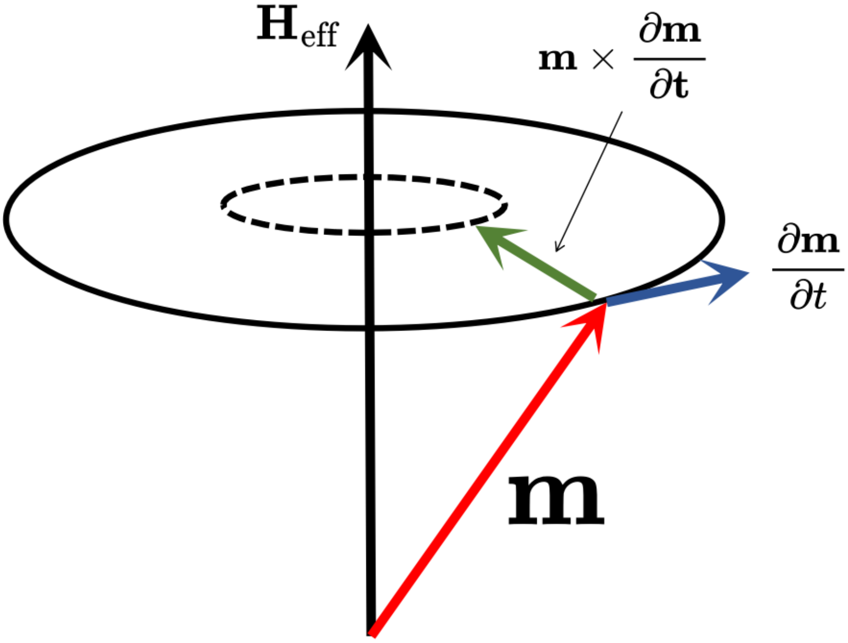

Fig. 2.4: Relationship between the terms of the LLG equation. The motion of the magnetization $\boldsymbol{m}$ is characterized by a damped precession induced by the effective field $\boldsymbol{H}_{\text{eff}}$.

2.4 Zhang-Li spin-transfer torque

When a polarized spin current is injected into a magnetic texture such as a skyrmion, the magnetization can be reoriented due to the spin-transfer torque (STT), causing the skyrmion to move. This effect can be described by the adiabatic and non-adiabatic terms of the Zhang-Li torque, expressed as [33]

$$\boldsymbol{\tau}_{\text{stt}} = -(\boldsymbol{u} \cdot \nabla)\boldsymbol{m} + \beta \boldsymbol{m} \times (\boldsymbol{u} \cdot \nabla)\boldsymbol{m}. \tag{2.18}$$

In Eq. (2.18), $\boldsymbol{u} = -\mu_B P \boldsymbol{J} / \left[e M_s (1 + \beta^2) \right]$ is the velocity vector associated with the electron flow induced by the spin-polarized current density $\boldsymbol{J}$, μ_B is the Bohr magneton, P denotes the spin polarization of the current, e is the electron charge and β is the non-adiabaticity constant. Each torque can be associated with an equivalent field, which facilitates the physical interpretation of the tendency of the magnetization to align under the action of these torques. These equivalent fields are given by

$$\begin{aligned} \boldsymbol{H}^{AD} &= \boldsymbol{m} \times (\boldsymbol{u} \cdot \nabla)\boldsymbol{m}, \\ \boldsymbol{H}^{nAD} &= -\beta \boldsymbol{m} \times \boldsymbol{m} \times (\boldsymbol{u} \cdot \nabla)\boldsymbol{m}. \end{aligned} \tag{2.19}$$

In Fig. 2.5, the equivalent field $\boldsymbol{H}^{\text{AD}}$ is responsible for dragging the magnetization along the direction of the current. It is referred to as adiabatic because it assumes that the electron spin perfectly follows the direction of the local magnetization. On the other

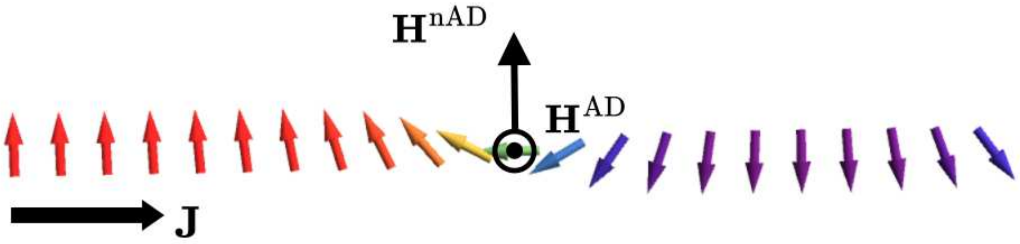

Fig. 2.5: Direction of the equivalent Zhang-Li fields in spin torque dynamics.

hand, the second field $\boldsymbol{H}^{\mathrm{nAD}}$ enables sustained and controlled motion of the magnetic texture. In this case, the electron spin fails to fully align with the local magnetization, resulting in a slight misalignment that produces an effective perpendicular force, introducing a dissipative component.

In systems such as Co/Pt, values of $\beta > 0.3$ have been reported [34], where the magnitude of β depends strongly on the material properties [35].

Chapter 3

Micromagnetism on curved surfaces

In this section, we will present the fundamental tools of differential geometry necessary to describe magnetic systems on curved surfaces. Subsequently, we will apply this formalism to reformulate the energies that constitute the micromagnetic model.

3.1 Differential geometry applied to magnetic systems

The importance of curved systems in magnetism is not limited to their technological application [36], as their study requires a theoretical framework that explicitly incorporates geometric effects into the fundamental equations of magnetism [12].

To develop this theory, we start with the following question: What happens to magnetization variations in a curved system? (See Fig. 3.1). To answer this question, we define the magnetization vector field $\boldsymbol{m}$ on a curved surface $\boldsymbol{\sigma}(\xi^1, \xi^2)$, which is parametrized by two variables $\{\xi^1, \xi^2\}$. This surface generates tangent basis vectors $\{\mathbf{g}_1, \mathbf{g}_2\}$ and a unit normal vector $\hat{\mathbf{n}}$. These tangent basis vectors induce a metric on the surface, represented by the metric tensor $g_{\alpha\beta} = \mathbf{g}_\alpha \cdot \mathbf{g}_\beta$ (where $\alpha, \beta = 1, 2$). This metric tensor contains all the necessary information about the intrinsic geometry of the surface.

In order to exploit all the local properties provided by the local reference frame, we now describe the magnetization vector field as

$$\mathbf{m} = m^\alpha \mathbf{g}_\alpha + m^3 \hat{\mathbf{n}} = m_\alpha \mathbf{g}^\alpha + m^3 \hat{\mathbf{n}}. \tag{3.1}$$

Thus, if we take into account the derivative of the magnetization, we can write it as

$$\partial_\beta \mathbf{m} = \partial_\beta m^\alpha \, \mathbf{g}_\alpha + m^\alpha \, \partial_\beta \mathbf{g}_\alpha + \partial_\beta (m^3 \hat{\mathbf{n}}). \tag{3.2}$$

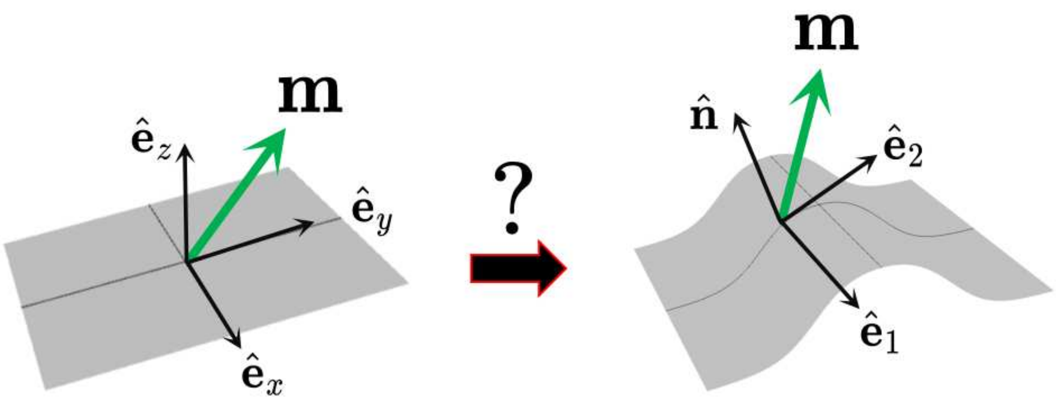

Fig. 3.1: Transition from a Cartesian coordinate system on a flat surface to a local frame on a curved geometry. In curved systems, the magnetization vector $\mathbf{m}$ is projected onto the local tangent basis $\{\hat{\boldsymbol{e}}_1, \hat{\boldsymbol{e}}_2\}$ and the normal vector $\hat{\boldsymbol{n}}$.

For now, we will focus on the second term on the right-hand side of equation (3.2). When working on a curved surface, the tangent basis vectors $\mathbf{g}_\alpha(\xi^1, \xi^2)$ are position-dependent, varying with the surface coordinates ξ^α. Consequently, the partial derivative of any vector field expressed in this basis must include contributions from the derivatives of the basis vectors themselves. The Christoffel symbols $\Gamma^\gamma_{\alpha\beta}$ are precisely the coefficients that describe this change within the tangent plane. Mathematically, this is expressed as

$$\partial_\beta \mathbf{g}_\alpha = \Gamma^\gamma_{\alpha\beta} \mathbf{g}_\gamma. \tag{3.3}$$

In other words, the derivative $\partial_\beta \mathbf{g}_\alpha$ (where $\partial_\beta \equiv \partial/\partial\xi^\beta$) can be expressed as a linear combination of the basis vectors $\mathbf{g}_\gamma$ with coefficients $\Gamma^\gamma_{\alpha\beta}$. Although the Christoffel symbols describe how the basis vectors change within the tangent plane, this information is not sufficient for curved surfaces embedded in three-dimensional space. Consequently, the simple relation $\partial_\beta \mathbf{g}_\alpha = \Gamma^\gamma_{\alpha\beta} \mathbf{g}_\gamma$ is not valid for general curved surfaces [37].

Intuitively, we can understand this by looking at Fig. 3.2, where we consider the displacement of a tangent vector from the tangent plane to a curved surface, and we observe how its direction changes. If we draw a vector parallel to the second vector, represented by a dashed line, we can see that the difference between our original vector and the displaced one corresponds to the arrow denoted by $\triangle \boldsymbol{g}_1$.

What are we doing here? By taking the partial derivative, we obtain the relationship between $\triangle \boldsymbol{g}_1$ and a small displacement $\delta\xi^1$, and in the limit $\delta\xi^1 \to 0$, we observe that this change in the vector introduces a normal component that points downward.

In other words, the change in the direction of the vector has produced a vector that is no longer purely tangent to the surface. Therefore, to correctly describe this change, we must add an additional term to the relation $\partial_\beta \mathbf{g}_\alpha = \Gamma^\gamma_{\alpha\beta} \mathbf{g}_\gamma$. If the resulting vector is not confined to the tangent plane, then we must include a term that contains the normal vector. So the corrected expression becomes

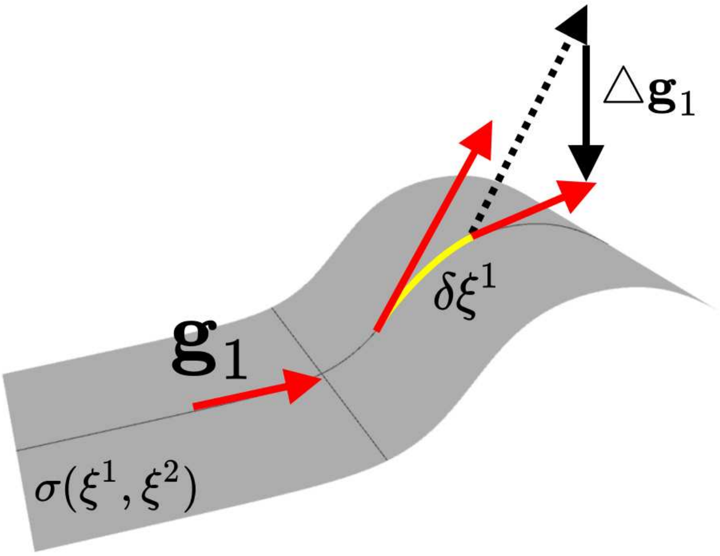

Fig. 3.2: Illustration of the variation of the tangent basis vector $\mathbf{g}_1$ along the coordinate ξ^1. Due to the curvature of the surface, the variation $\Delta\mathbf{g}_1$ includes a component normal to the surface.

$$\partial_\beta \mathbf{g}_\alpha = \Gamma^{\gamma}_{\alpha\beta}\,\mathbf{g}_\gamma + b_{\alpha\beta}\,\hat{\mathbf{n}}, \tag{3.4}$$

where $b_{\alpha\beta}$ is the magnitude of the normal vector $\hat{\mathbf{n}}$. Therefore, by substituting the Eq. (3.4) into Eq. (3.2), we obtain

$$\partial_\beta \boldsymbol{m} = (\partial_\beta m^\alpha + \Gamma^{\alpha}_{p\beta} m^p)\boldsymbol{g}_\alpha + b_{\alpha\beta}\,\hat{\mathbf{n}} + \partial_\beta(m^3\hat{\mathbf{n}}). \tag{3.5}$$

The term $\partial_\beta m^\alpha + \Gamma^{\alpha}_{p\beta} m^p$ provides a more accurate description of the rate of change of the component m^α than the partial derivative $\partial_\beta m^\alpha$ alone. We therefore define the covariant derivative of the component m^α as

$$\bar{\partial}_\beta m^\alpha = \partial_\beta m^\alpha + \Gamma^{\alpha}_{p\beta} m^p. \tag{3.6}$$

This allows us to rewrite Eq. (3.2) as

$$\partial_\beta \boldsymbol{m} = \bar{\partial}_\beta m^\alpha \boldsymbol{g}_\alpha + b_{\alpha\beta}\,\hat{\mathbf{n}} + \partial_\beta(m^3\hat{\mathbf{n}}). \tag{3.7}$$

Now, we focus on the term $b_{\alpha\beta}$, known as the curvature tensor. In its mixed form, $b^{\beta}_{\alpha} = g^{\beta\gamma} b_{\gamma\alpha}$, the values along the diagonal are called the principal curvatures, denoted by b^1_1 and b^2_2. The curvature tensor allows us to extract two key geometric quantities: the mean curvature $\mathscr{H}$ and the Gaussian curvature $\mathcal{K}$, which are defined as [37]

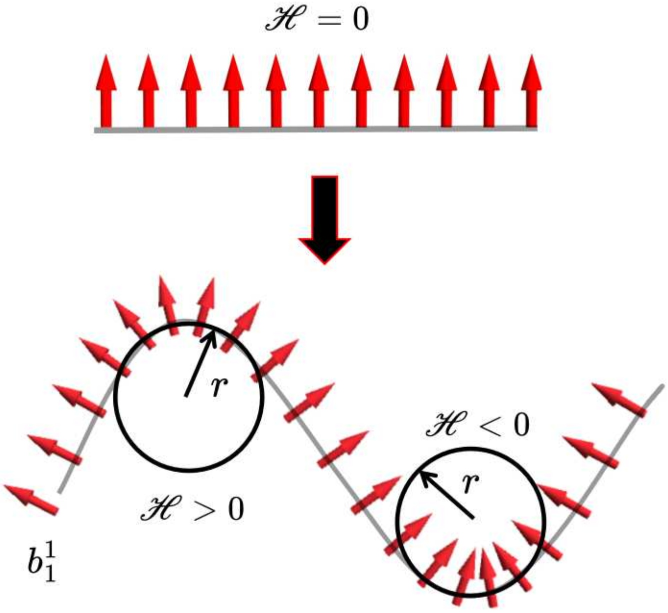

Fig. 3.3: Effect of mean curvature $\mathscr{H}$ on the orientation of normal vector.

$$\begin{aligned} \mathscr{H} &= \mathrm{Tr}(b^{\alpha}_{\beta}) = b_1^1 + b_2^2, \\ \mathcal{K} &= \det(b^{\alpha}_{\beta}) = b_1^1 b_2^2. \end{aligned} \tag{3.8}$$

In two-dimensional spaces, curvature is a property that measures how much a curve deviates from being a straight line. This idea can be extended beyond curves to entire surfaces embedded in three-dimensional space. In this context, curvature is analyzed in multiple directions through the $\mathscr{H}$ and $\mathcal{K}$, which generalize the concept of how much a surface "bends" at each point.

To develop an intuitive understanding of the mean curvature, let us consider a surface in three-dimensional space that bends only in one direction. This is equivalent to assuming that one of the principal curvatures is zero, for example, $b_2^2 = 0$. In that case, the mean curvature reduces to $\mathscr{H} = b_1^1$; that is, it depends solely on the curvature in one direction.

As an example, imagine a magnetic strip where the magnetization vectors are initially perpendicular to the plane of the strip. As we see in Fig 3.3. If we now bend the strip, it is possible to analyze $\mathscr{H}$ by observing how the normal vectors vary along the surface. If the strip is flat, all the normal vectors are parallel to each other, which implies that $\mathscr{H} = 0$. If the surface bends forming a bump upwards, the normal vectors diverge; in this case $\mathscr{H} > 0$. Conversely, if the surface bends forming a bump downwards, the normal vectors converge, which is associated with $\mathscr{H} < 0$.

On the other hand, the Gaussian curvature $\mathcal{K}$ measures how a surface bends in all possible directions around a point. To analyze it, it is more convenient to directly consider

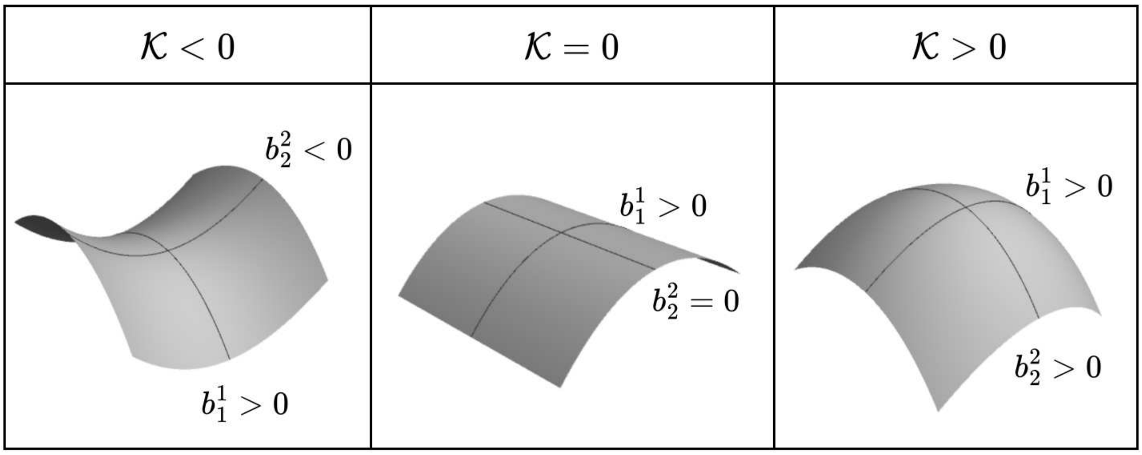

Fig. 3.4: Illustration of Gaussian curvature $\mathcal{K}$ based on the signs of the principal components of the curvature tensor b^α_β.

the intrinsic geometric properties of the surface. For example, Fig 3.4 illustrates different representative cases of Gaussian curvature.

We can see that the Gaussian curvature can be positive, negative, or zero, depending on the signs of the principal curvatures. In Fig 3.4 (a), the case of a hyperbolic paraboloid is shown, where the principal curvatures have opposite signs. In this case, $\mathcal{K} < 0$, indicating a hyperbolic geometry. On the other hand, in Fig 3.4 (b), the surface curves in one direction but remains flat in the perpendicular direction. As a consequence, $\mathcal{K} = 0$, which indicates that despite the visible curvature, the surface does not have intrinsic curvature in the two-dimensional sense. Finally, in Fig 3.4 (c), both principal curvatures are equal and positive. In this case, the $\mathcal{K} > 0$, reflecting that the surface is closed and curves in the same direction in all directions.

Now, to complete the analysis of the magnetization dynamics in curved systems, we focus on the third term on the right-hand side of Eq. (3.7), which can be expanded as

$$\partial_\beta(m^3\hat{\mathbf{n}}) = \partial_\beta m^3\hat{\mathbf{n}} + m^3\partial_\beta\hat{\mathbf{n}}. \tag{3.9}$$

The derivative of the unit normal vector $\hat{\mathbf{n}}$ with respect to a tangential direction ∂_α on a surface, denoted by $\partial_\alpha\hat{\mathbf{n}}$, describes how the local orientation of the surface changes as one moves along ∂_α. Since $\hat{\mathbf{n}}$ is a unit vector, its derivative cannot have a component in the normal direction, and therefore $\partial_\alpha\hat{\mathbf{n}}$ must lie in the tangent plane.This variation is intrinsically related to the surface curvature and is described by the Weingarten formula [37]:

$$\partial_\beta\hat{\mathbf{n}} = -b_{\alpha\beta}\mathbf{g}^\alpha = -b^\alpha{}_\beta\mathbf{g}_\alpha. \tag{3.10}$$

Substituting Eq. (3.10) into Eq. (3.9), we have that

$$\partial_\beta\left(m^3\hat{\mathbf{n}}\right) = \left(\partial_\beta m^3\right)\hat{\mathbf{n}} - m^3 b^\alpha{}_\beta \mathbf{g}_\alpha. \tag{3.11}$$

Finally, the variation of the magnetization with respect to the curvilinear coordinates of the surface can be expressed as

$$\partial_\beta \boldsymbol{m} = (\bar{\partial}_\beta m^\alpha - m^3 b^\alpha_\beta)\boldsymbol{g}_\alpha + (m^3 b_{\beta\alpha} \ + \partial_\beta m^3)\hat{\mathbf{n}}. \tag{3.12}$$

With this equation, we can substitute into the micromagnetic energy equations to determine how the energies are affected by the change in geometry. Although the expressions were derived, the steps are not shown here because they mainly involve straightforward algebra. Instead, the focus is on the physical and geometrical meaning of the results, which is more important for this study.

3.2 Micromagnetic energies in a curvilinear frame

Now that we have established the implications of expressing the magnetization vector in a curved coordinate system, we can reformulate the micromagnetic energy terms introduced in Chapter 2 within the curvilinear framework. This section presents the expression of each energy contribution adapted to curved geometries, emphasizing how curvature modifies their structure and physical interpretation.

3.2.1 Exchange interaction on a curved surface

In curved magnetic systems, the exchange energy density takes the form [12]

$$\mathscr{E}^{\mathrm{X}} = \mathscr{E}^{\mathrm{X}}_0 + \mathscr{E}^{\mathrm{X}}_A + \mathscr{E}^{\mathrm{X}}_D, \tag{3.13}$$

with

$$\mathscr{E}^{\mathrm{X}}_0 = A\,\bar{\partial}_\alpha m^\lambda\,\bar{\partial}^\alpha m_\lambda, \tag{3.14}$$

$$\mathscr{E}^{\mathrm{X}}_A = A b^\alpha{}_\gamma b^\gamma{}_\beta m_\alpha m^\beta + A b^\alpha{}_\beta b^\beta{}_\alpha m_3 m^3, \tag{3.15}$$

$$\mathscr{E}^{\mathrm{X}}_D = 2A b^\alpha{}_\beta\left(m^\beta\bar{\partial}_\alpha m_3 - m^3\bar{\partial}_\alpha m^\beta\right). \tag{3.16}$$

Here, $\lambda = 1, 2, 3$ and $\mathscr{E}^{\mathrm{X}}_0$ corresponds to the isotropic exchange contribution, which reduces to the standard expression in flat geometries. The remaining terms, $\mathscr{E}^{\mathrm{X}}_A$ and $\mathscr{E}^{\mathrm{X}}_D$, arise solely from the curvature of the system.

The term $\mathscr{E}^{\mathrm{X}}_A$ is referred to as the curvature-induced anisotropy associated with the exchange energy. An intuitive way to understand the origin of this term is by considering the transition from a flat ferromagnetic state, where the exchange energy is zero (Fig. 3.5(a)), to a curved system (Fig. 3.5(b)). When the system is curved, the magnetic moments are forced to form angles θ with each other, especially in regions of higher curvature. We observe that the magnetic moments tend to align in such a way that they follow the curvature variation. This adjustment introduces an energetic cost, which is captured by the additional term $\mathscr{E}_A^{\mathrm{X}}$. Hence the name curvature-induced anisotropy. This also explains why, in Eq. (3.15), the magnetization appears in a quadratic form, indicating that there is no intrinsic preferential direction.

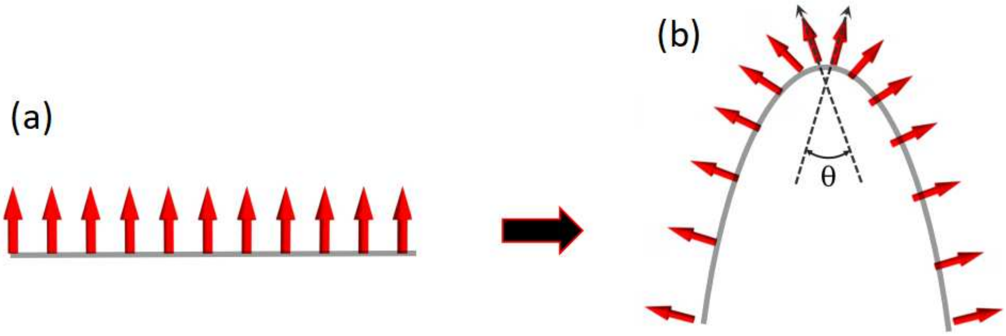

Fig. 3.5: Schematic illustration of the origin of curvature-induced anisotropy in the exchange energy. (a) In a flat system. (b) In a curved system, the magnetization vectors follow the geometry of the surface.

The term $\mathscr{E}_D^{\mathrm{X}}$ is referred to as the curvature-induced DMI. It represents a chiral interaction that favors the formation of spin textures with a specific sense of rotation. This interaction is induced by the curvature of the system and is analogous to the conventional Dzyaloshinskii–Moriya interaction, but arises purely from geometric effects. For this reason, it can be regarded as a form of extrinsic DMI.

Suppose we have a skyrmion-like magnetization texture in a ferromagnetic strip (see Fig. 3.6(a)). When the system is curved, the local spatial symmetry is broken, leading to an interaction that can twist the magnetization depending on the curvature of the surface. If the system is bent in a particular way, as shown in Fig. 3.6(b), the magnetic moments at the skyrmion core become more aligned (i.e., more parallel) than if the strip were bent in the opposite direction (see Fig. 3.6(c)). This suggests that curvature can either stabilize or destabilize skyrmions, effectively mimicking the role of intrinsic DMI.

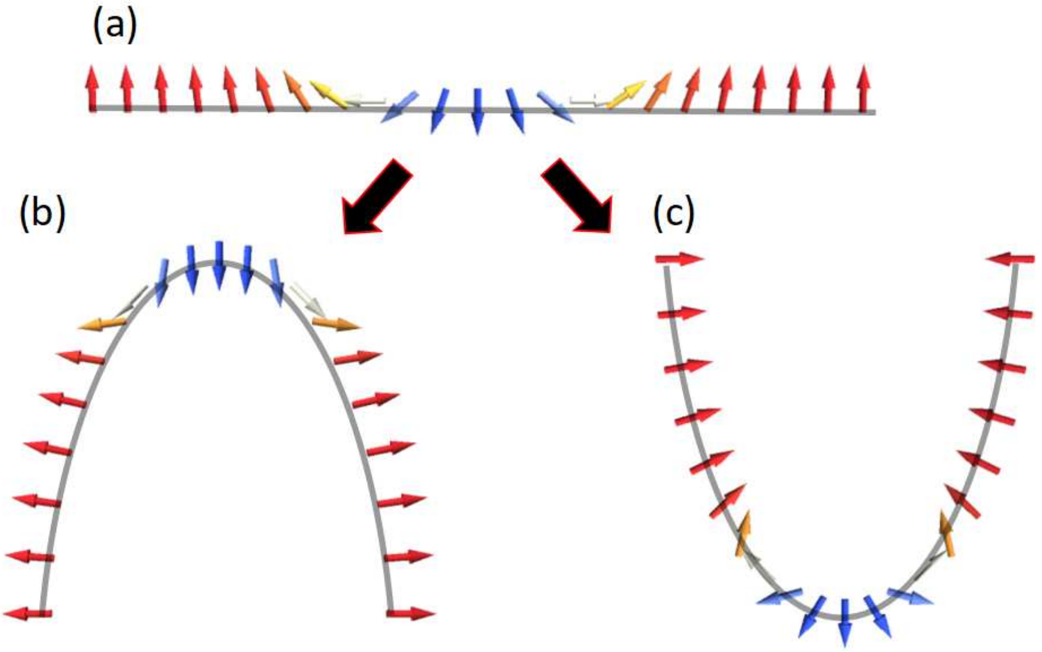

Fig. 3.6: Curvature-induced modification of a skyrmion-like texture. (a) Flat geometry; (b, c) deformed geometries.

3.2.2 DMI in curved surface

In a curved system, the interfacial DMI energy density can be written as [12]

$$\mathscr{E}^{\mathrm{DMI(i)}} = \mathscr{E}_D^{\mathrm{DMI(i)}} + \mathscr{E}_A^{\mathrm{DMI(i)}}, \tag{3.17}$$

where

$$\mathscr{E}_D^{\mathrm{DMI(i)}} = D^{(i)}(m^3\bar{\partial}_\alpha m^\alpha - m^\alpha\bar{\partial}_\alpha m^3), \tag{3.18}$$

$$\mathscr{E}_A^{\mathrm{DMI(i)}} = -D^{(i)}\mathscr{H}m_3 m^3. \tag{3.19}$$

Here, $\mathscr{E}_{\mathrm{D}}^{\mathrm{DMI(i)}}$ corresponds to the intrinsic interfacial Dzyaloshinskii–Moriya interaction generalized to a curved surface. The additional contribution $\mathscr{E}_{\mathrm{A}}^{\mathrm{DMI(i)}}$ originates from the interplay between the interfacial DMI and the surface curvature and can be interpreted as an effective geometry-induced anisotropy term that arises solely from the curvature of the magnetic surface.

A similar interpretation to that made for the term $\mathscr{E}_{\mathrm{A}}^{\mathrm{X}}$ can be extended here. If we consider a scenario in which no chiral texture is formed in a Co/Pt system, as illustrated in Fig. 3.7(a), where all spins are uniformly aligned, bending the system induces a angle θ between neighboring magnetic moments, even though no such angle exists in the planar case. This effect is schematically shown in Fig. 3.7(b).

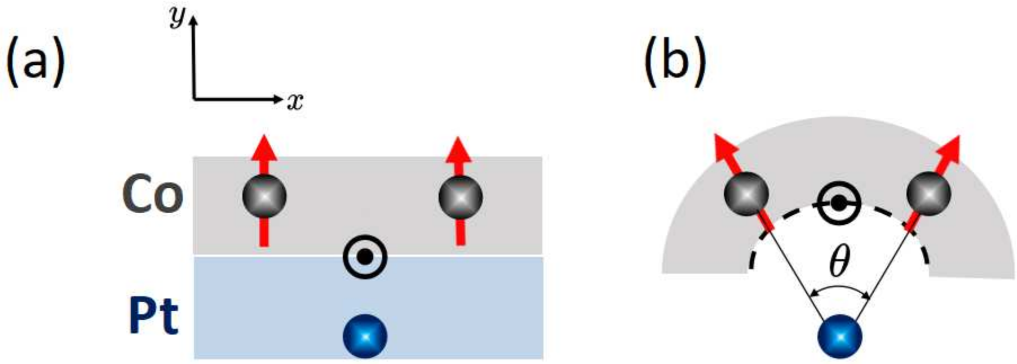

Fig. 3.7: Curvature-induced canting of magnetic moment in a Co/Pt system: (a) planar, (b) curved, showing a finite angle θ between neighboring moments.

In a curved system, the energy density of bulk DMI can be expressed as [12]

$$\mathscr{E}^{\mathrm{DMI(b)}} = \mathscr{E}_D^{\mathrm{DMI(b)}} + \mathscr{E}_A^{\mathrm{DMI(b)}}, \tag{3.20}$$

where

$$\mathscr{E}_D^{\mathrm{DMI(b)}} = D^{(b)}(m_\beta \bar{\partial}_\alpha m^3 - m^3 \bar{\partial}_\alpha m_\beta), \tag{3.21}$$

$$\mathscr{E}_A^{\mathrm{DMI(b)}} = D^{(b)} \epsilon^{\beta\alpha} b_{\gamma\beta} m_\alpha m^\beta. \tag{3.22}$$

Here, $\mathscr{E}_D^{\mathrm{DMI(b)}}$ is analogous to the planar Bloch DMI term $\mathbf{m} \cdot (\nabla \times \mathbf{m})$, but adapted to curved geometries using covariant derivatives. The term $\mathscr{E}_A^{\mathrm{DMI(b)}}$ favors configurations in which the tangential components of the spin couple to the extrinsic curvature of the surface.

Chapter 4

Theoretical model

4.1 Geometry

In our model, we consider a very thin magnetic shell of thickness h. We parameterize the bent nanotube of length L as

$$\boldsymbol{\sigma}(\xi^1,\xi^2) = (R + r\sin(\xi^2/r))\sin(\xi^1/R)\hat{\boldsymbol{e}}_x + (R + r\sin(\xi^2/r))\cos(\xi^1/R)\hat{\boldsymbol{e}}_y + r\cos(\xi^2/r)\hat{\boldsymbol{e}}_z, \tag{4.1}$$

where ξ^1 and ξ^2 denote the arc-length coordinates in the toroidal and poloidal directions, respectively. The minor and major radii of the bent nanotube are indicated by r and R, as shown in Fig. 4.1(a). Examples of bent nanotubes obtained by varying the angle ψ and substituting the relation $R = L/2\psi$ into the parametric equation are shown in Fig. 4.1(b).

This surface defines and orthonormal curvilinear basis $\hat{\boldsymbol{e}}_1 = \boldsymbol{g}_1/|\boldsymbol{g}_1|$, $\hat{\boldsymbol{e}}_2 = \boldsymbol{g}_2/|\boldsymbol{g}_2|$ and $\hat{\boldsymbol{n}} = \hat{\boldsymbol{e}}_1 \times \hat{\boldsymbol{e}}_2$, with $\boldsymbol{g}_1 = \partial_{\xi^1}\boldsymbol{\sigma}$ and $\boldsymbol{g}_2 = \partial_{\xi^2}\boldsymbol{\sigma}$.

Under this parametrization, we can obtain the metric tensor $g_{\alpha\beta} = \boldsymbol{g}_\alpha \cdot \boldsymbol{g}_\beta$ as

$$g_{\alpha\beta} = \begin{pmatrix} \left(1 + \frac{r}{R}\sin(\xi^2/r)\right)^2 & 0 \\ 0 & 1 \end{pmatrix}, \tag{4.2}$$

the curvature tensor $b_{\alpha\beta} = \hat{\boldsymbol{n}} \cdot \partial_\alpha \boldsymbol{g}_\beta$:

$$b_{\alpha\beta} = \begin{pmatrix} -\frac{R+r\sin(\xi^2/r)}{R^2}\sin(\xi^2/r) & 0 \\ 0 & -1/r \end{pmatrix}, \; b^\alpha_\beta = \begin{pmatrix} -\frac{\sin(\xi^2/r)}{R+r\sin(\xi^2/r)} & 0 \\ 0 & -1/r \end{pmatrix} \tag{4.3}$$

and the Christoffel symbols:

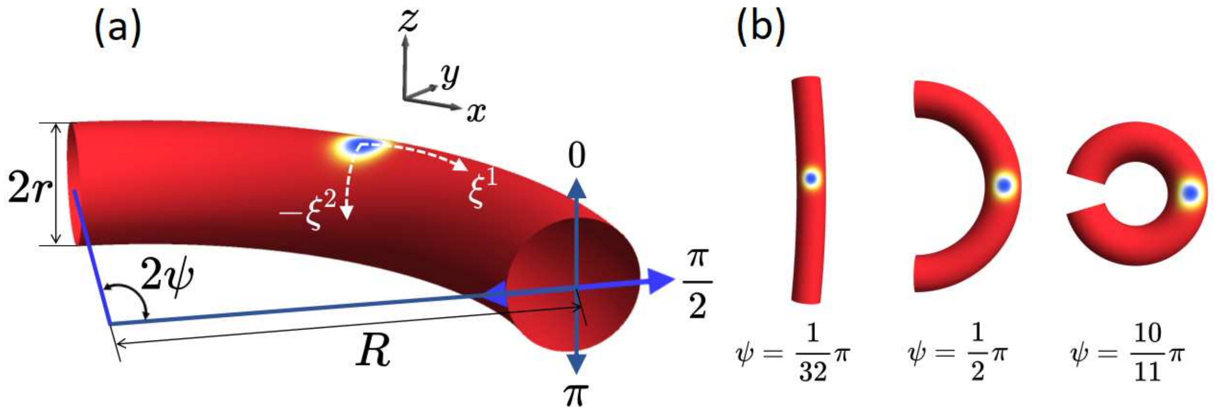

Fig. 4.1: (a) Geometry of the bent nanotube and definition of the toroidal ξ^1 and poloidal ξ^2 coordinates. (b) Nanotube configurations for different bending curvatures ψ.

$$\begin{aligned}\Gamma^1_{12} = \Gamma^1_{21} &= -\frac{\sin(\xi^2/r)}{R + r\cos(\xi^2/r)},\\ \Gamma^2_{11} &= \frac{(R + r\cos(\xi^2/r))\sin(\xi^2/r)}{R^2}.\end{aligned} \tag{4.4}$$

From the curvature tensor, the mean curvature $\mathscr{H}(\xi^2) = b^1_1 + b^2_2$ and the Gaussian curvature $\mathcal{K}(\xi^2) = b^1_1 b^2_2$ can be obtained as

$$\begin{aligned}\mathscr{H}(\xi^2) &= -\frac{\sin(\xi^2/r)}{(R + r\sin(\xi^2/r))} - \frac{1}{r},\\ \mathcal{K}(\xi^2) &= \frac{\sin(\xi^2/r)}{r(R + r\sin(\xi^2/r))}.\end{aligned} \tag{4.5}$$

4.2 Skyrmion anzats

The unit magnetization vector $\boldsymbol{m}$ can be expressed using an angular parametrization in the surface basis as

$$\boldsymbol{m} = \cos\Phi\,\sin\Theta\,\hat{\boldsymbol{e}}_1 + \sin\Phi\,\sin\Theta\,\hat{\boldsymbol{e}}_2 + \cos\Theta\,\hat{\boldsymbol{n}}.$$

Here, Θ and Φ denote the angular fields defining the magnetization texture through an ansatz. For a skyrmion on a curved surface, these angles can be expressed as [38]

$$\begin{aligned}\Theta(\xi^1,\xi^2) &= \Theta_{pl}\left(\sqrt{g_{11}(\xi^1 - X^1)^2 + g_{22}(\xi^2 - X^2)^2}\right),\\ \Phi(\xi^1,\xi^2) &= \arctan\left(\frac{\sqrt{g_{22}}(\xi^2 - X^2)}{\sqrt{g_{11}}(\xi^1 - X^1)}\right) + \phi_0,\end{aligned} \tag{4.6}$$

which depend on the surface coordinates ξ^1 and ξ^2, with (X^1, X^2) denoting the collective coordinates that describe the position of the skyrmion center. The function Θ_{pl} represents the planar skyrmion profile; in this thesis, we adopt the Braun ansatz [39], given by

$$\Theta_{pl}(s) = 2\arctan\left(\frac{\sinh(R_s/w)}{\sinh(s/w)}\right), \tag{4.7}$$

where the parameter $w = \pi D/(4K)$ corresponds to the skyrmion domain-wall width, while R_s denotes the skyrmion radius. This ansatz is adopted due to its accuracy in predicting theoretical results that are in good agreement with numerical simulations.

4.3 Planar approximation

To investigate how surface curvature affects the skyrmion energy, we assume that the skyrmion profile remains unchanged [38]. This assumption is valid as long as the skyrmion radius is much smaller than the typical curvature scales of the surface

Within this approximation, the metric tensor can be evaluated at the skyrmion center, $g_{\alpha\beta}(\xi^1,\xi^2) \approx g_{\alpha\beta}(X^1,X^2)$. It is then convenient to introduce the change of variables $\sqrt{g_{11}}(\xi^1 - X^1) = \rho\cos\chi$ and $\sqrt{g_{22}}(\xi^2 - X^2) = \rho\sin\chi$. Furthermore, the curvature functions $\mathscr{H}(\xi^2)$ and $\mathcal{K}(\xi^2)$ are expanded about a fixed reference point X^2 using a Taylor series [40]:

$$\mathscr{H}(\xi^2) = \mathscr{H}(X^2) + \frac{\rho\sin\chi}{\sqrt{g_{22}}}\,\mathscr{H}'(X^2) + \frac{1}{2}\left(\frac{\rho\sin\chi}{\sqrt{g_{22}}}\right)^2 \mathscr{H}''(X^2) + \cdots \tag{4.8}$$

$$\mathcal{K}(\xi^2) = \mathcal{K}(X^2) + \frac{\rho\sin\chi}{\sqrt{g_{22}}}\,\mathcal{K}'(X^2) + \frac{1}{2}\left(\frac{\rho\sin\chi}{\sqrt{g_{22}}}\right)^2 \mathcal{K}''(X^2) + \cdots \tag{4.9}$$

In this expansion, we retain only the zeroth-order term. This is sufficient to describe the influence of curvature on the skyrmion energy, while higher-order terms are negligible either due to their small magnitude or because they cancel out by symmetry (cf. Appendix A). Throughout this thesis, we adopt the notation $\mathscr{H}(X^2) = \mathscr{H}$ and $\mathcal{K}(X^2) = \mathcal{K}$. This change permits the skyrmion ansatz to be written in polar coordinates, as illustrated in Fig. 4.2, as

$$\begin{aligned} \Theta_{pl}(\rho) &= 2\arctan\left(\frac{\sinh(R_s/w)}{\sinh(\rho/w)}\right), \\ \Phi(\chi) &= \chi + \phi_0. \end{aligned} \tag{4.10}$$

The magnetization components can then be expressed in polar coordinates as

$$\begin{aligned} m^1 &= \frac{\sin\Theta(\rho)\cos\Phi(\chi)}{\sqrt{g_{11}}} = \frac{m_\rho\cos\Phi(\chi)}{\sqrt{g_{11}}} \\ m^2 &= \frac{\sin\Theta(\rho)\sin\Phi(\chi)}{\sqrt{g_{22}}} = \frac{m_\rho\sin\Phi(\chi)}{\sqrt{g_{22}}} \\ m^3 &= \cos\Theta(\rho) = m_z \end{aligned} \tag{4.11}$$

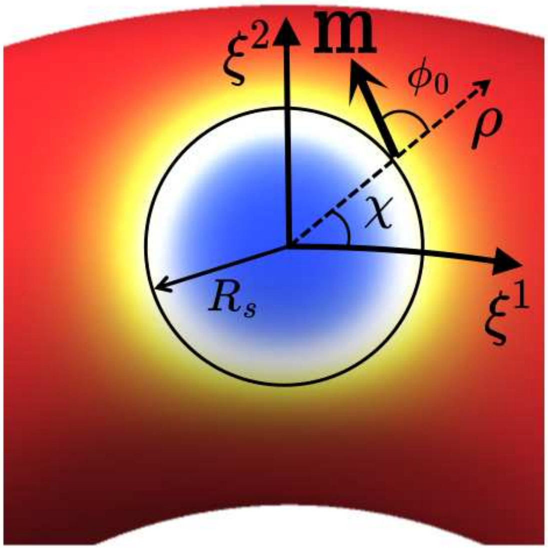

Fig. 4.2: Local planar approximation of the curved surface around the skyrmion core. Within this approximation, the skyrmion profile can be defined in terms of polar coordinates (ρ, χ). This approximation remains valid provided that the skyrmion does not undergo significant deformation.

The importance of this approximation lies in the fact that it enables the skyrmion energy contributions to be expressed in an analytical form, thereby providing direct physical insight into the role of curvature and significantly simplifying the theoretical analysis.

Chapter 5

Curvature-induced modification of the current driven skyrmions on motion

In this chapter, we derive the generalized Thiele equation for arbitrary curved surfaces, incorporating the effects of Zhang–Li spin-transfer torques. We begin by discussing the Thiele equation for a planar geometry and then analyze the differences that arise when extending it to a curved surface.

5.1 Current-driven skyrmion dynamics on a plane

A key factor for advancing skyrmion-based technologies and enabling skyrmion displacement operations is the precise control of skyrmion movement driven by spin-transfer torques. In flat geometries, the theoretical understanding of this motion has been thoroughly investigated, especially in systems such as FeGe [41–43] that stabilize Bloch skyrmions, as well as in systems like Co/Pt [6, 10], where Néel skyrmions are favored.

The Thiele equation [44] offers a comprehensive framework to describe skyrmion motion driven by spin-transfer torques. In this approach, the skyrmion is treated as a rigid spin structure, allowing the analysis to concentrate on the dynamics of its center of mass. Within this formalism, the skyrmion velocity $\boldsymbol{v} = (v_x, v_y)$ can be obtained from the competition between the different forces acting on it. The thiele equation in a plane is given by

$$\boldsymbol{G} \times (\boldsymbol{v} - \boldsymbol{u}) + \boldsymbol{\mathcal{D}}(\beta \boldsymbol{u} - \alpha \boldsymbol{v}) = 0. \tag{5.1}$$

Here, $\boldsymbol{G}$ is the gyroscopic vector (or gyrovector) and $\boldsymbol{\mathcal{D}}$ is the dissipative tensor, which are defined respectively by

$$\mathbf{G} = \begin{pmatrix} 0 \\ 0 \\ G \end{pmatrix}, \quad G = -\frac{\mu_0 M_s t}{\gamma} \iint dx\, dy\, \mathbf{m} \cdot \left(\frac{\partial \mathbf{m}}{\partial x} \times \frac{\partial \mathbf{m}}{\partial y} \right), \tag{5.2}$$

$$\boldsymbol{\mathcal{D}} = \begin{pmatrix} D_{xx} & D_{xy} \\ D_{yx} & D_{yy} \end{pmatrix}, \quad D_{ij} = \frac{M_s t}{\gamma} \iint dx\, dy \left(\frac{\partial \mathbf{m}}{\partial x_i} \cdot \frac{\partial \mathbf{m}}{\partial x_j} \right). \tag{5.3}$$

By assuming the skyrmion with rotational symmetry, we consider that the magnetization texture satisfies $\partial \mathbf{m}/\partial x \perp \partial \mathbf{m}/\partial y$. This leads to the mixed components of the dissipation tensor being zero, i.e., $D_{xy} = D_{yx} = 0$, while the diagonal elements are equal, $D_{xx} = D_{yy} = D$. Under these assumptions, and using the gyrovector definition for a topologically non-trivial texture, the gyrovector magnitude is given by $G = -\frac{M_s t}{\gamma} 4\pi N_{\text{sk}}$. As a result, the tensor in the Thiele equation simplify to

$$\mathbf{G} = \begin{pmatrix} 0 \\ 0 \\ G \end{pmatrix}, \qquad G = -4\pi \frac{\mu_0 M_s t}{\gamma} p, \tag{5.4}$$

$$\boldsymbol{\mathcal{D}} = \begin{pmatrix} D & 0 \\ 0 & D \end{pmatrix}, \qquad D = \frac{\mu_0 M_s t}{\gamma} \iint dx\, dy \left(\frac{\partial \mathbf{m}}{\partial x} \right)^2. \tag{5.5}$$

By substituting Eqs. (5.4) and (5.5) into Eq. (5.1) and assuming a current density $\boldsymbol{J}$ applied along the $-x$ direction (i.e., $\boldsymbol{u} = (u, 0)$), we can determine the explicit forms of the longitudinal (v_x) and transverse (v_y) components of the skyrmion velocity as

$$v_x = u\, \frac{\alpha\beta D^2 + G^2}{\alpha^2 D^2 + G^2}, \tag{5.6}$$

$$v_y = u\, \frac{(\alpha - \beta) D G}{\alpha^2 D^2 + G^2}. \tag{5.7}$$

From Eqs. (5.6) and (5.7), we can identify two fundamental mechanisms that determine the trajectory of a skyrmion: (i) the polarity of the skyrmion p, and (ii) the relationship between the damping coefficient α and the non-adiabatic term β.

To illustrate the first mechanism, let us fix α and β such that $\alpha > \beta$. In this configuration, the transverse component of the skyrmion velocity (along the y-direction) is determined by the polarity p. That is, skyrmions with $p = +1$ are deflected towards the $+y$ direction, while those with $p = -1$ are deflected in the opposite direction (see Fig. 5.1). This deflection of the skyrmion with respect to the current direction is a consequence of the Magnus force, which arises from the topological coupling between the magnetic texture and the spin current.

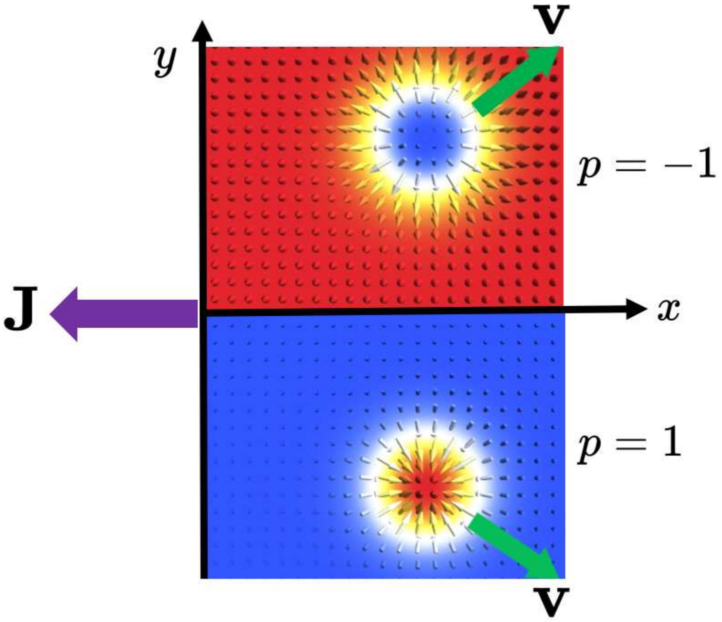

Fig. 5.1: Dependence of the skyrmion motion direction on the polarity p. For $p = +1$ and $p = -1$, the transverse direction of the velocity $\boldsymbol{v}$ changes sign, highlighting the topological nature of the SkHE.

This transverse force exists due to the skyrmion's nontrivial topology and depends directly on the topological charge N_{sk}. Such behavior is analogous to the conventional Hall effect for charged particles, where the direction of the Lorentz force depends on the sign of the charge. For this reason, it is also referred to as the skyrmion Hall effect (SkHE).

To analyze the second mechanism, we fix the skyrmion polarity to $p = -1$ and examine how the dynamics are affected by the relationship between α and β. As shown in Fig. 5.2, when $\alpha > \beta$, the skyrmion exhibits a positive transverse velocity component (SkHE towards $+y$); when $\alpha = \beta$, the motion is just longitudinal in the direction opposite to the current (with no transverse deflection); and when $\alpha < \beta$, the SkHE is reversed, and the skyrmion is deflected towards $-y$. Therefore, this mechanism also governs the direction of the SkHE.

Although the condition $\alpha = \beta$ appears theoretically attractive for spintronic applications such as racetrack memories, this equality is rarely achieved in real materials. Theoretical studies indicate that this condition is satisfied only in idealized models, which never apply to real materials due to the unavoidable presence of spin-orbit coupling and disorder effects [45].

This naturally raises the question: what happens to these two mechanisms of motion when the skyrmion is no longer moving on a flat plane, but along a curved track? We investigate this question in the next section.

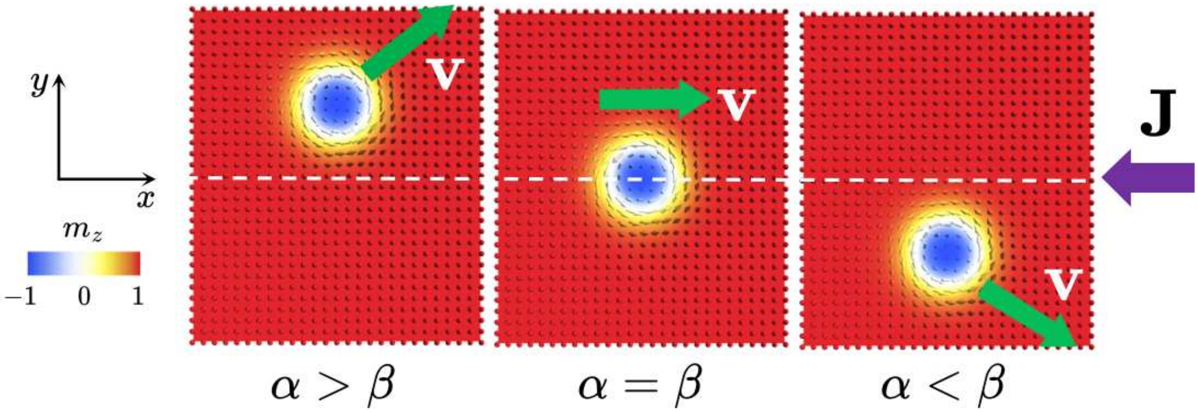

Fig. 5.2: Relative influence of the dissipation coefficients α and β on the skyrmion dynamics with fixed polarity $p = -1$. Three regimes are observed: positive deflection, pure longitudinal motion, and negative deflection.

5.2 Generalized Thiele equation in curved surfaces

The dynamics of skyrmions in different curved geometries have attracted considerable attention due to the unique interactions that arise in such systems. For example, studies of cylindrical films with a sinusoidal directrix (Fig. 5.3(a)) have demonstrated that skyrmions experience curvature-induced drift even in the absence of external stimuli [40]. In their work, the curvature gradient acts as an effective potential that drives the skyrmions toward regions of lower energy. Similarly, for curved tracks with Gaussian bumps (Fig. 5.3(b)), skyrmion propagation is controlled by a curvature-induced force (CIF) originating from the gradient of the geometry-induced potential energy [46]. This force can either accelerate or block the skyrmion motion depending on the applied current density. Their micromagnetic simulations revealed critical current thresholds required to overcome geometric barriers. Meanwhile, in straight nanotubes (Fig. 5.3(c)), the system thickness has been shown to significantly influence the skyrmion velocity under applied currents, thereby requiring corrections to traditional flat models [16].

While the aforementioned works provide valuable insight into curvature-induced effects in specific systems, there is no unified theory capable of predicting the skyrmion motion across general geometries while accounting for the Zhang–Li torque.

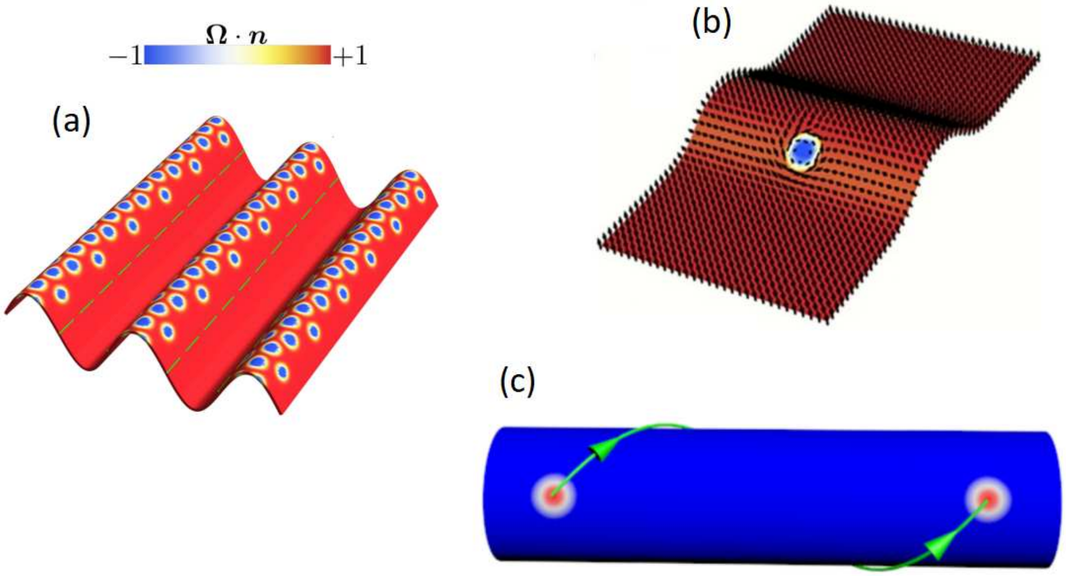

Fig. 5.3: Skyrmion dynamics in various curved geometries: (a) Cylindrical film with a sinusoidal directrix, (b) surface with a Gaussian bump and (c) straight magnetic nanotube. Figure adapted from [16, 40, 46]

In this work, we generalize the Thiele equation by incorporating the Zhang–Li torque in arbitrarily curved systems. Our derivation provides a unified description of current-driven skyrmion motion in curvilinear geometries, combining the effects of curvature and STT.

Let us consider a very thin magnetic shell parametrized by $\boldsymbol{\sigma}(\xi^1, \xi^2, \xi^3)$, where $\xi^3 \in [-h/2,\, h/2]$ denotes the coordinate across the shell thickness. The geometry of the system is described by its mid-surface, defined at $\xi^3 = 0$, which represents a curved two-dimensional surface embedded in three-dimensional space.

The surface geometry is characterized by the tangent basis vectors $\boldsymbol{g}_\alpha = \partial\boldsymbol{\sigma}/\partial\xi^\alpha$ $(\alpha = 1, 2)$, the corresponding unit vectors $\boldsymbol{e}_\alpha = \boldsymbol{g}_\alpha/|\boldsymbol{g}_\alpha|$, and the associated metric tensor $g_{\alpha\beta} = \boldsymbol{g}_\alpha \cdot \boldsymbol{g}_\beta$, which fully describes the intrinsic geometry of the curved surface. The unit normal vector $\boldsymbol{n} \equiv \boldsymbol{e}_1 \times \boldsymbol{e}_2$ defines the extrinsic orientation, as depicted in Fig. 5.4. To exploit the magnetic properties of a curved system, the magnetization unit vector can be parametrized in a local basis as $\boldsymbol{m} = m^\alpha \boldsymbol{e}_\alpha + m^n \boldsymbol{n}$, where the Einstein sum convention (repeated index represents sums) has been adopted.

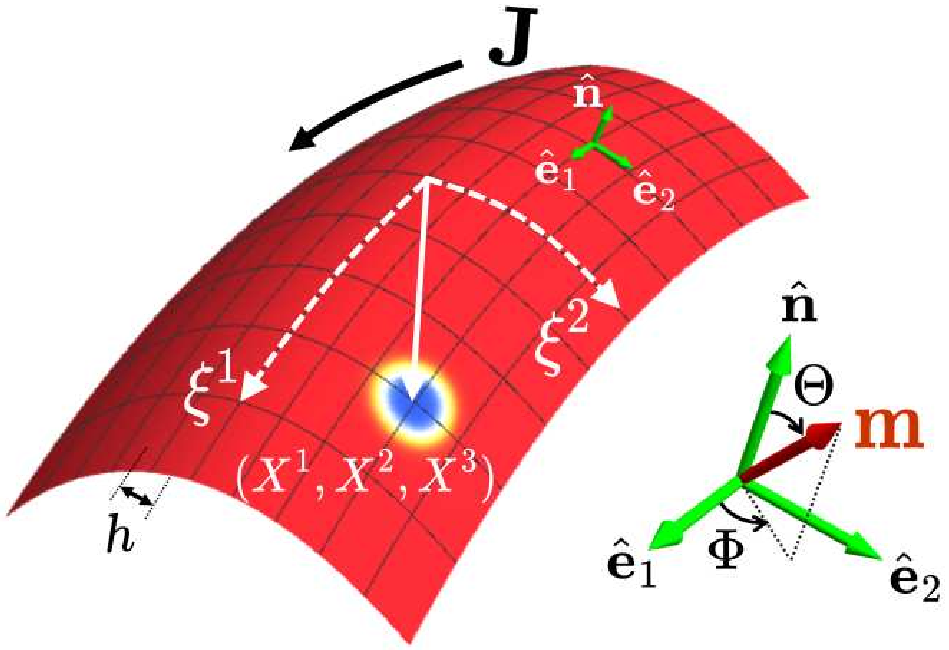

Fig. 5.4: Parametrization of a curvilinear shell. The skyrmion position is given by (X^1, X^2), and the magnetization vector $\mathbf{m}$ is described by the spherical angles (Θ, Φ) in the local frame. A current $\mathbf{j}$ is applied tangentially to the surface.

We define the skyrmion center as

$$\boldsymbol{\mathcal{R}} = \boldsymbol{\sigma}(X^1(t), X^2(t), X^3(t)), \tag{5.8}$$

then the velocity of the skyrmion is given by

$$\frac{\partial \boldsymbol{\mathcal{R}}}{\partial t} = \widetilde{g}_i \dot{X}^i. \tag{5.9}$$

Here $\widetilde{g}_{kl} = \widetilde{\boldsymbol{g}}_k \cdot \widetilde{\boldsymbol{g}}_l$ is the metric tensor with $\widetilde{\boldsymbol{g}} = \det(\widetilde{g}_{kl})$. Assuming the skyrmion maintains its shape throughout its motion and the magnetization is located at (ξ^1, ξ^2, ξ^3). The skyrmion center as a function of time can be expressed as

$$\boldsymbol{m} = \boldsymbol{m}(\xi^1 - X^1, \xi^2 - X^2, \xi^3 - X^3). \tag{5.10}$$

This enables us to express the derivatives with respect to the collective coordinates $\partial \boldsymbol{m}/\partial X^j$ and the time derivative $\partial \boldsymbol{m}/\partial t$ in terms of the curvilinear coordinates (ξ^1, ξ^2, ξ^3) as

$$\frac{\partial \boldsymbol{m}}{\partial X^i} = -\partial_j m^\lambda \tilde{\boldsymbol{g}}_\lambda, \tag{5.11}$$

$$\frac{\partial \boldsymbol{m}}{\partial t} = -\partial_j m^\lambda \partial_t X^j \tilde{\boldsymbol{g}}_\lambda \tag{5.12}$$

with $\frac{\partial m^\lambda}{\partial \xi^j} = \partial_j m^\lambda$. To calculate the dynamics of the skyrmions, we solve the LLG equation incorporating the τ_{stt} term, which represents the influence of the current within the magnetic material, as given by

$$\frac{\partial \boldsymbol{m}}{\partial t} = \gamma \boldsymbol{m} \times \boldsymbol{H}_{\text{eff}} + \alpha \boldsymbol{m} \times \frac{\partial \boldsymbol{m}}{\partial t} + \boldsymbol{\tau}_{\text{stt}}. \tag{5.13}$$

The $\boldsymbol{\tau}_{\text{stt}}$ can be written as

$$\boldsymbol{\tau}_{\text{stt}} = -(\boldsymbol{u} \cdot \nabla)\boldsymbol{m} + \beta \boldsymbol{m} \times (\boldsymbol{u} \cdot \nabla)\boldsymbol{m}. \tag{5.14}$$

To solve Eq. (5.13), we follow the Thiele formalism [44], which describes the dynamics of a rigid magnetic texture by expressing all torque contributions as effective forces, leading to the following condition:

$$\boldsymbol{H}^{\text{g}} + \boldsymbol{H}^{\text{c}} + \boldsymbol{H}^{\text{d}} + \boldsymbol{H}^{\text{AD}} + \boldsymbol{H}^{\text{nAD}} = 0, \tag{5.15}$$

where

$$\boldsymbol{H}^{\text{g}} = -\boldsymbol{m} \times \frac{\partial \boldsymbol{m}}{\partial t}, \tag{5.16}$$

$$\boldsymbol{H}^{\text{c}} = \gamma \boldsymbol{m} \times \boldsymbol{m} \times \boldsymbol{H}_{\text{eff}}, \tag{5.17}$$

$$\boldsymbol{H}^{\text{d}} = \frac{\alpha}{\gamma} \boldsymbol{m} \times \frac{\partial \boldsymbol{m}}{\partial t}, \tag{5.18}$$

$$\boldsymbol{H}^{\text{AD}} = -\frac{1}{\gamma} \boldsymbol{m} \times (\boldsymbol{u} \cdot \nabla)\boldsymbol{m}, \tag{5.19}$$

$$\boldsymbol{H}^{\text{nAD}} = \frac{\beta}{\gamma} \boldsymbol{m} \times \boldsymbol{m} \times (\boldsymbol{u} \cdot \nabla)\boldsymbol{m}. \tag{5.20}$$

Here, $\boldsymbol{H}^{\text{g}}$ is the gyroscopic effective field, $\boldsymbol{H}^{\text{c}}$ represents the conservative (energy contributions) effective field, and $\boldsymbol{H}^{\text{d}}$ corresponds to the dissipative field. The terms $\boldsymbol{H}^{\text{AD}}$ and $\boldsymbol{H}^{\text{nAD}}$ account for the adiabatic and non-adiabatic components of the STT , respectively.

According to Tretiakov *et al.* [47], the generalized force associated with each of these effective fields can be calculated by integrating the corresponding torque over space. In this way, the total force acting on the rigid magnetic texture can be written as

$$\boldsymbol{F} = F_i \hat{\boldsymbol{e}}_i, \quad F_i = -\mu_0 M_s \int_V \boldsymbol{H} \cdot \frac{\partial \boldsymbol{m}}{\partial X^i}\, dV, \tag{5.21}$$

with $dV = \sqrt{g(\xi^1, \xi^2, \xi^3)}$. The vector $\boldsymbol{F}$ represents the generalized force acting on the magnetic texture due to the effective field $\boldsymbol{H}$.

Gyroscopic tensor

We calculate the force contribution associated with the gyroscopic term, which arises from the time-dependent dynamics of the magnetization. This force is directly related to the gyrovector in the planar case. By substituting Eq. (5.16) into Eq. (5.21), and using the time and spatial derivatives given in Eqs. (5.11) and (5.12), the gyroscopic force can be expressed as

$$F^g_a = -\frac{\mu_0 M_s}{\gamma}\dot{X}^b \int_V \varepsilon_{k\lambda l} m^k \partial_i m^\lambda \partial_j m^l \, dV. \tag{5.22}$$

Here, $\varepsilon_{kln} = \sqrt{|\tilde{g}|}\,\epsilon_{kln}$ is the Levi-Civita tensor, with $\tilde{g} = \det||\tilde{g}_{ij}||$ denoting the determinant of the three-dimensional metric tensor. Considering a general surface parametrized by $\boldsymbol{\sigma}(\xi^1, \xi^2)$ and adopting the planar approximation (i.e., $g_{\alpha\beta}(\xi^1, \xi^2) \approx g_{\alpha\beta}(X^1, X^2)$), it has been shown that, in the limit where the curvature radii are much larger than the skyrmion size, Eq. (5.22) approaches its flat-film value as [38]

$$F^g_i = -G_{ab}\dot{X}^j, \tag{5.23}$$

where G_{ab} is the gyroscopic tensor, defined as

$$G_{ab} = \frac{\mu_0 M_s h}{\gamma}\,\epsilon_{ab}\,4\pi N_{\text{sk}}. \tag{5.24}$$

The gyrovector can also be expressed in vector form as $\boldsymbol{G} = (0, 0, -G)$ with $G = \frac{\mu_0 M_s h}{\gamma} 4\pi N_{\text{sk}}$, pointing along the surface normal [38]. However, in this work we adopt the tensor formulation, which captures the relevant physics without loss of generality.

Dissipative tensor

Following similar reasoning, the general dissipative force is given by

$$F^d_i = \alpha\frac{\mu_0 M_s}{\gamma}\dot{X}^j \int_V g_{l\lambda}\,\partial_i m^\lambda\,\partial_j m^l\,dV, \tag{5.25}$$

which, for a surface and under the planar approximation [38], becomes

$$F^d_a = -\alpha D_{ab}\dot{X}^b, \tag{5.26}$$

where the dissipative tensor is defined as

$$D_{ab} = \frac{\mu_0 M_s h}{\gamma}\int_S \left[g_{\gamma\eta}\partial_a m^\eta \partial_b m^\gamma + \partial_a m^3 \partial_b m^3\right] dS. \tag{5.27}$$

Here, $i, j, k, \lambda, l, p, q \in \{1, 2, 3\}$ and $a, b, \gamma, \eta \in \{1, 2\}$, with $dS = \sqrt{g(\xi^1, \xi^2)}\,d\xi^1 d\xi^2$.

Curvature-current tensors

We calculate the forces associated with the fields $\boldsymbol{H}^{\mathrm{AD}}$ and $\boldsymbol{H}^{\mathrm{nAD}}$. First, we derive the effective field associated with the $\boldsymbol{H}^{\mathrm{AD}}$ in a curved system:

$$\begin{aligned} \boldsymbol{H}^{\mathrm{AD}} &= -\frac{1}{\gamma}\boldsymbol{m} \times \big[(\boldsymbol{u}\cdot\nabla)\boldsymbol{m}\big] \\ &= -u^j[m^l \partial_j m^p \varepsilon_{klp} \widetilde{\boldsymbol{g}}^k + m^p m^l \widetilde{\boldsymbol{g}}_l \times \partial_j \widetilde{\boldsymbol{g}}_p]. \end{aligned} \tag{5.28}$$

Projecting this field along $\partial\boldsymbol{m}/\partial X^i$, we obtain:

$$\begin{aligned} \boldsymbol{H}^{\mathrm{AD}} \cdot \frac{\partial \boldsymbol{m}}{\partial X^i} = u^j \Big[&\varepsilon_{l\lambda p}\, m^l\, \partial_i m^\lambda\, \partial_j m^p \\ &- \varepsilon_{l\lambda q}\, m^l\, \partial_i m^\lambda\, \widetilde{\boldsymbol{g}}^q \cdot \big(\{m^\alpha \Gamma^\gamma_{j\alpha} - m^3 b^\gamma_j\}\boldsymbol{g}_\gamma + m^\alpha b_{j\alpha}\, \hat{\boldsymbol{n}}\big)\Big]. \end{aligned} \tag{5.29}$$

Substituting Eq. (5.29) into Eq. (5.21) and considering the planar approximation, the force associated with $\boldsymbol{H}^{\mathrm{AD}}$ can be expressed as

$$F^{\mathrm{AD}}_a = u^b G_{ab} + u^b \frac{\mu_0 M_s h}{\gamma} \int_S \sqrt{g} \begin{vmatrix} m^1 & \partial_a m^1 & (m^\gamma \Gamma^1_{b\gamma} - m^3 b^1_b) \\ m^2 & \partial_a m^2 & (m^\gamma \Gamma^2_{b\gamma} - m^3 b^2_b) \\ m^3 & \partial_a m^3 & m^\gamma b_{b\gamma} \end{vmatrix} dS. \tag{5.30}$$

We note that the second term on the right-hand side of Eq. (5.30) depends on the Christoffel symbols and the curvature tensor. Therefore, in a planar system this term vanishes, showing that a new contribution to the force associated with the field $\boldsymbol{H}^{\mathrm{AD}}$ arises in curved systems. We define this curvature-induced contribution as the tensor G^u_{ab}:

$$G^u_{ab} = \frac{\mu_0 M_s h}{\gamma} \int_S \sqrt{g} \begin{vmatrix} m^1 & \partial_a m^1 & (m^\gamma \Gamma^1_{b\gamma} - m^3 b^1_b) \\ m^2 & \partial_a m^2 & (m^\gamma \Gamma^2_{b\gamma} - m^3 b^2_b) \\ m^3 & \partial_a m^3 & m^\gamma b_{b\gamma} \end{vmatrix} dS. \tag{5.31}$$

We now turn to the force generated by $\boldsymbol{H}^{\mathrm{nAD}}$ in curved geometries. Although the derivation follows the same general framework as in the adiabatic case, the resulting force exhibits a different structure due to its dissipative nature.

The effective field associated with the non-adiabatic term is given by

$$\boldsymbol{H}^{\mathrm{nAD}} = -\frac{\beta}{\gamma}\, u^j \left(\partial_j m^l\, \widetilde{\boldsymbol{g}}_l + m^l\, \partial_j \widetilde{\boldsymbol{g}}_l\right). \tag{5.32}$$

To evaluate the corresponding force, this field is projected onto the collective coordinate derivative $\partial \boldsymbol{m}/\partial X^i$, yielding

$$\begin{aligned}\boldsymbol{H}^{\mathrm{nAD}} \cdot \frac{\partial \boldsymbol{m}}{\partial X^i} = \frac{\beta}{\gamma}\, u^j \Big[& \widetilde{g}_{l\lambda}\, \partial_j m^l\, \partial_i m^\lambda \\ & + \partial_i m^\lambda\, \widetilde{\boldsymbol{g}}_\lambda \cdot \big(m^\alpha \Gamma^\gamma_{j\alpha} - m^3 b^\gamma_j\big) \boldsymbol{g}_\gamma + \partial_i m^\lambda\, m^\alpha b_{j\alpha} \hat{\boldsymbol{n}} \Big].\end{aligned} \tag{5.33}$$

Introducing this expression into Eq. (5.21) and assuming the planar approximation, the force produced by the non-adiabatic term can be written as

$$F_a^{\mathrm{nAD}} = -\beta\, u^b D_{ab} - \beta\, u^b \frac{\mu_0 M_s h}{\gamma} \int_S \Big[g_{\eta\gamma}\, \partial_a m^\eta \left(m^\omega \Gamma^\gamma_{\omega b} - m^3 b^\gamma_b\right) + m^\omega\, \partial_a m^3\, b_{b\omega} \Big] dS. \tag{5.34}$$

In analogy with Eq. (5.30), the second term on the right-hand side of Eq. (5.34) explicitly depends on the Christoffel symbols and the curvature tensor. Consequently, this contribution vanishes in planar geometries. This observation allows us to identify a curvature-induced to the non-adiabatic force. We therefore define this contribution as a geometry-dependent dissipative tensor D^u_{ab}:

$$D^{\mathrm{u}}_{ab} = \frac{\mu_0 M_s h}{\gamma} \int_S \Big[g_{\eta\gamma}\, \partial_a m^\eta \left(m^\omega \Gamma^\gamma_{\omega b} - m^3 b^\gamma_b\right) + m^\omega\, \partial_a m^3\, b_{b\omega} \Big] dS. \tag{5.35}$$

Therefore, the additional tensors G^{u}_{ab} and D^{u}_{ab} arise solely from the curvature of the magnetic surface, giving rise to a novel curvature-induced interaction that directly affects the magnetization dynamics.

By summing all force contributions associated with the dynamics, as given by Eqs. (5.23), (5.26), (5.29), and (5.34), and including the energy gradient $\partial E/\partial X^a$, the resulting equation of motion can be written as

$$G_{ab}(\dot{X}^b - u^b) = \frac{\partial E}{\partial X^a} + D_{ab}(\alpha \dot{X}^b - \beta u^b) + (G^u_{ab} - \beta D^u_{ab}) u^b. \tag{5.36}$$

Equation (5.36) coincides with the Thiele equation generalized for the case of STT [48]. However, the last two terms, G^u_{ab} and D^u_{ab}, are new contributions incorporated into the generalized Thiele equation and depend on the curvature. Since these terms are multiplied by the drift velocity of the conduction electrons, u^b, which is in turn proportional to the current density $\boldsymbol{J}$, they enable a combined action between STT and curvature. Importantly, (5.36) is not restricted to skyrmions but is generally applicable to rigid magnetic textures driven by spin-polarized currents in curvilinear geometries. Our derivation therefore provides a unified description of current-driven magnetic texture dynamics in curved systems, capturing the interplay between curvature and STT.

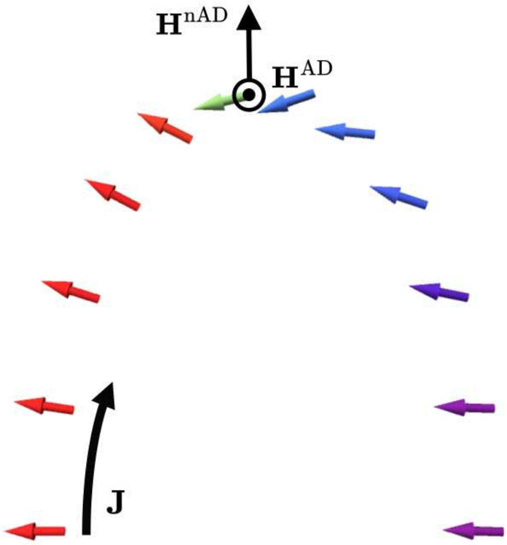

Fig. 5.5: Schematic representation of the effective fields $\boldsymbol{H}^{\mathrm{AD}}$ and $\boldsymbol{H}^{\mathrm{nAD}}$ acting on a magnetization texture under a current density $\boldsymbol{J}$ on a curved surface. The field $\boldsymbol{H}^{\mathrm{AD}}$ lies in the local tangential plane, while $\boldsymbol{H}^{\mathrm{nAD}}$ points along the surface normal.

It is well established that, in quasi-one-dimensional systems, curvature modifies the effective spin-transfer torque (STT) [40], while in geometries with curvature gradients it leads to chiral symmetry breaking and direction-dependent depinning currents [49]. Despite these advances, the role of curvature in current-driven transport on two-dimensional magnetic shells remains largely unexplored. In this context, Eq. (5.36) can be regarded as a natural extension of these one-dimensional curvature-induced effects to two-dimensional curved manifolds. This generalized formulation provides a suitable framework to investigate skyrmion dynamics in curved magnetic shells and to elucidate the impact of the curvature-induced tensors on their current-driven motion.

To clarify the origin of the additional tensors, we analyze the orientation of the effective fields $\boldsymbol{H}^{\mathrm{AD}}$ and $\boldsymbol{H}^{\mathrm{nAD}}$ on a curved surface. As illustrated in Fig. 5.5, when an electric current $\boldsymbol{J}$ is applied to a magnetic texture such as a skyrmion, it induces a collective motion of the magnetization. In this configuration, the field $\boldsymbol{H}^{\mathrm{AD}}$ is oriented along the local surface normal, whereas $\boldsymbol{H}^{\mathrm{nAD}}$ lies within the tangential plane. In curved geometries, both the normal and tangential directions vary spatially along the surface. As a result, the effective fields acquire geometry-dependent contributions, which manifest as curvature-induced tensors in the effective equations of motion.

Chapter 6

Results and discussion

In this chapter, we apply the generalized Thiele equation to a bent nanotube. First, we analyze how the curvature is modified when bending the nanotube. Then, we calculate the skyrmion energy under the influence of these curvatures, and finally, we study how curvature affects the dynamics of skyrmions.

6.1 Mean and Gaussian curvature in a bent nanotube

A bent nanotube of total length $L = 1130\,\mathrm{nm}$ and inner radius $r = 50\,\mathrm{nm}$ is analyzed. The influence of the curvature control angle ψ on the mean $\mathscr{H}(\xi^2)$ and Gaussian $\mathcal{K}(\xi^2)$ curvatures is examined, as described in Eq. (4.5). Three representative geometries are considered, corresponding to different values of ψ: $\psi = \pi/32$, describing an almost straight nanotube; $\psi = \pi/2$, representing a semicircular bent nanotube; and $\psi = 10\pi/11$, corresponding to an almost fully closed nanotube.

As shown in Fig. 6.1(a), for the nearly straight nanotube ($\psi = \pi/32$), the Gaussian curvature exhibits only minor variations and remains close to zero along the entire angular coordinate. At higher bending angles, such as $\psi = \pi/2$ and $\psi = 10\pi/11$, the Gaussian curvature $\mathcal{K}$ becomes negative in the inner region ($\xi^2/r \in [-\pi, 0]$), reaching a minimum at $\xi^2/r = -\pi/2$, and positive in the outer region ($\xi^2/r \in [0, \pi]$), where it attains a maximum at $\xi^2/r = \pi/2$.

In contrast, as shown in Fig. 6.1(b), the mean curvature $\mathscr{H}$ displays a markedly different behavior. For $\psi = \pi/32$, it remains nearly constant at a value close to $-1/r$ over the entire geometry. As the bending angle increases ($\psi = \pi/2$ and $\psi = 10\pi/11$), the mean curvature stays negative throughout the nanotube, reaching a maximum (least negative value) at $\xi^2/r = -\pi/2$ and a minimum (most negative value) at $\xi^2/r = \pi/2$, corresponding to the stretched outer side.

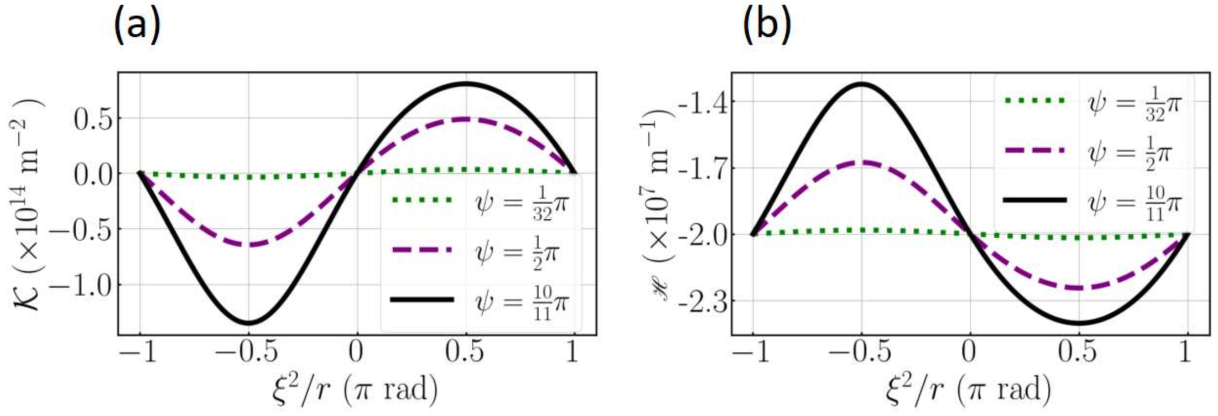

Fig. 6.1: Curvature analysis of a bent nanotube showing (a) Gaussian curvature $\mathcal{K}$ and (b) mean curvature $\mathscr{H}$. The angular coordinate ξ^2/r represents the normalized angular coordinate.

6.2 Skyrmion energy on a bent nanotube

The energy of a skyrmion in a bent nanotube can be obtained using an analytical expression derived under the planar approximation. This allows the energy to be expressed as a function of the skyrmion center position (X^1, X^2) along the bent nanotube.

The energy of Néel skyrmion on a bent nanotube is given by (see Appendix A)

$$\begin{aligned} E^{(\mathrm{N})}(X^2) = 2\pi h \Bigg[A \left(C_0 - \frac{\mathscr{H}^2 - 2\mathcal{K}}{2} C_1 - \mathscr{H} C_2 + \frac{\mathbb{N}}{2\pi} \right) \\ + D^{(i)} \left(C_2 + \frac{\mathscr{H} C_1}{2} - \frac{\mathbb{M}}{2\pi} \right) + K C_1 \Bigg]. \end{aligned} \tag{6.1}$$

when C_0, C_1 and C_2 are constants that depend on the material parameters, while $\mathbb{N}$ and $\mathbb{M}$ are functionals that depend on the curvature but are independent of the skyrmion position. All of these quantities are defined as

$$C_0 = \int_0^\infty \left(\left(\frac{\partial \Theta}{\partial \rho} \right)^2 + \frac{\sin^2 \Theta}{\rho^2} \right) \rho d\rho, \tag{6.2}$$

$$C_1 = \int_0^\infty \sin^2 \Theta \rho d\rho, \tag{6.3}$$

$$C_2 = \int_0^\infty \left(\frac{\partial \Theta}{\partial \rho} + \frac{\sin \Theta \cos \Theta}{\rho} \right) \rho d\rho, \tag{6.4}$$

$$\mathbb{N} = \int_{-L/2}^{L/2} \int_{-\pi}^{\pi} [\mathscr{H}^2(\xi^2) - 2\mathcal{K}(\xi^2)] \sqrt{g}\, d\xi^1\, d\xi^2, \tag{6.5}$$

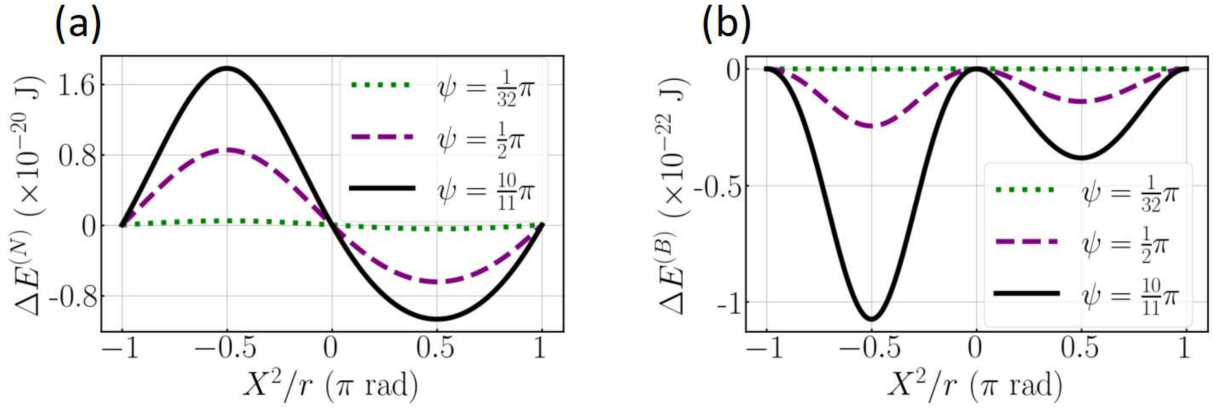

Fig. 6.2: Total energy $E^{(N)}$ of a (a) Néel skyrmion and (b) Bloch skyrmion as a function of the poloidal coordinate direction X^2/r for different curvature control angles ψ.

$$\mathbb{M} = \int_{-L/2}^{L/2} \int_{-\pi}^{\pi} \mathscr{H}(\xi^2)\sqrt{g}\, d\xi^1 d\xi^2. \tag{6.6}$$

The functionals $\mathbb{N}$ and $\mathbb{M}$ cause a shift in the energies depending on the curvature, and therefore can be neglected in the context of our dynamical analysis. By defining $E'' = E - E'$, where E' is the energy independent of $\mathscr{H}$ and $\mathcal{K}$, that is, $\Delta E(X^2) = E''(X^2) - E''(\pi)$, we have obtained the skyrmion energy for each considered open angle.

We can now determine the energy $\Delta E(X^2)$ for a Néel skyrmion hosted on a bent nanotube. We consider the material Pt/Co/AlOx, which presents the following material parameters [38]: saturation magnetization $M_s = 1.09817 \times 10^6$ A/m, exchange stiffness $A = 1.6 \times 10^{-11}$ J/m, uniaxial anisotropy constant $K_u = 1.4 \times 10^6$ J/m^3 and the DMI interfacial constant $D^{(i)} = 2.8 \times 10^{-3}$ J/m^2. The film thickness was $h = 1$ nm. The fixed geometrical parameters are $L = 1130$ nm and $r = 50$ nm. To determine the role that the curvature plays. we consider three values for the open angle: $\psi = \pi/32$, $\psi = \pi/2$ and $\psi = 10\pi/11$.

Figure 6.2(a) shows the energy $\Delta E^{(N)}$ of a Néel skyrmion as a function of the poloidal coordinate X^2/r. For $\psi = \pi/32$, the skyrmion energy remains nearly constant along the poloidal direction, indicating that the geometry has a negligible influence on the energy. For larger curvatures, such as $\psi = \pi/2$ and $\psi = 10\pi/11$, a clear trend emerges, indicating that the skyrmion becomes sensitive to the tube geometry. In both cases, curvature promotes the spontaneous localization of the skyrmion around $X^2/r \approx \pi/2$, where the energy attains a global minimum.

To ensure a direct comparison with the Néel skyrmion energy, the Bloch skyrmion is considered within the same material parameters. The corresponding energy expression is given as (see Appendix A)

$$E^{(\mathrm{B})}(X^2) = 2\pi h \left[A \left(C_0 - \left(\frac{\mathscr{H}^2 - 2\mathcal{K}}{2} \right) C_1 + \frac{\mathbb{N}}{2\pi} \right) + D^{(b)} C_2 + K C_1 \right] \tag{6.7}$$

Figure. 6.2.(b) shows the energy $\Delta E^{(B)}$ of a Bloch skyrmion as a function of the poloidal coordinate. For small curvature, specifically $\psi = \frac{1}{32}\pi$, the skyrmion energy remains nearly constant along the bent nanotube. As the curvature increases, we observe a modulation with well-defined energy minima located around $X^2/r \approx -\frac{\pi}{2}$ and $\frac{\pi}{2}$, and maxima at the extremes and the center $(X^2/r = \pm\pi, 0)$.

When comparing with the Néel skyrmion case, we find that both types exhibit similar qualitative behavior: curvature induces energy modulation along the tube. Notably, both Bloch and Néel skyrmions reach a low-energy state at $X^2/r = \pi/2$; however, this minimum is local for the Bloch skyrmion and global for the Néel skyrmion. Furthermore, at $X^2/r = -\pi/2$, the Bloch skyrmion reaches its global energy minimum, whereas this same point corresponds to a global energy maximum for the Néel skyrmion.

An important difference lies in the amplitude of the energy variation. The Néel skyrmion exhibits a significantly larger energy modulation compared to the Bloch skyrmion, indicating that it is more sensitive to the curvature. This increased sensitivity is attributed to the contribution of the term $\mathscr{H}C_2$, which is dominant compared to the other terms. Moreover, this $\mathscr{H}C_2$ term is absent in the energy expression of the Bloch skyrmion because the intrinsic DMI in this case is isotropic. Therefore, the Néel skyrmion in a bent nanotube is more sensitive to curvature, with the mean curvature being the main geometric contribution responsible for this effect.

6.3 Curvature-induced force

Due to the energy gradients caused by curvature, skyrmions experience a force that drives them toward regions where their energy is minimized. This force is known as the curvature-induced force and can be calculated as [50]

$$\begin{aligned} \mathscr{F} &= -\nabla E \\ &= -(g_{\alpha\alpha}(X^1, X^2))^{-1/2} \frac{\partial E}{\partial X^\alpha} \hat{\mathbf{e}}_\alpha. \end{aligned} \tag{6.8}$$

For the Néel skyrmion case, the curvature-induced force is given by

$$\mathscr{F}^{(\mathrm{N})}(X^2) = \pi h \left[A F_1(X^2) C_1 - 2A F_2(X^2) C_2 + D^{(i)} F_2(X^2) C_1 \right], \tag{6.9}$$

where

$$F_1(X^2) = \frac{2R\sin(X^2)\cos(X^2)}{r(R + r\sin(X^2))^3}, \tag{6.10}$$

$$F_2(X^2) = -\frac{R\cos(X^2)}{r(R + r\sin(X^2))^2}. \tag{6.11}$$

Figure. 6.3.(a) shows the curvature-induced force $\mathscr{F}^{(N)}$ acting on a Néel skyrmion. For larger curvature values, such as $\psi = \frac{10}{11}\pi$, the force profile becomes significantly stronger and more asymmetric.

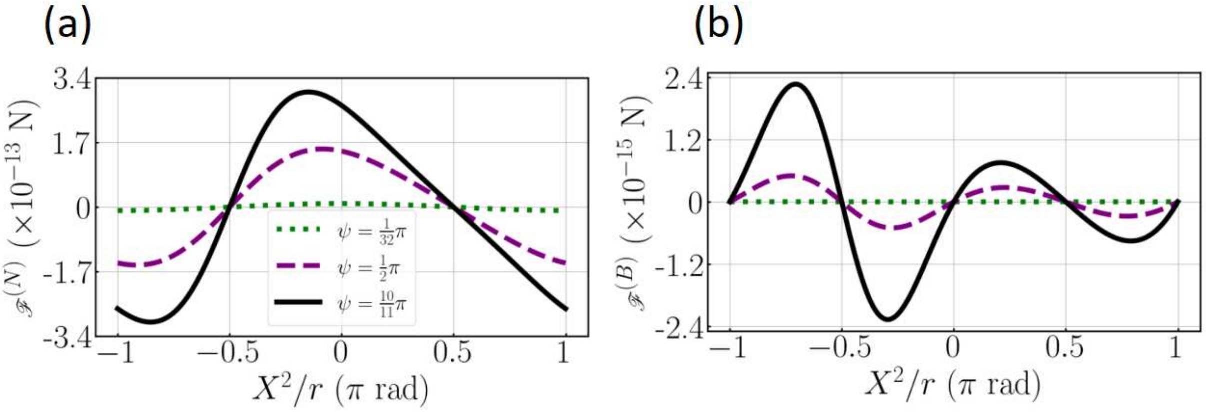

Fig. 6.3: Curvature-induced force acting on a (a) Néel skyrmion and (b) Bloch skyrmion along the poloidal direction X^2/r for different curvature values ψ.

The maximum of the force is located near the center ($\chi^2/r = 0$), where the skyrmion experiences a pronounced driving force toward the positive poloidal direction. We also observe that the force profile is not symmetric around the peak, indicating that the skyrmion is more readily accelerated in a preferred direction, namely for positive values of X^2/r.

The curvature-induced force of the Bloch skyrmion is

$$\mathscr{F}^{(\mathrm{B})}(X^2) = \pi h A F_1(X^2). \tag{6.12}$$

As shown in Fig. 6.3(b), the force acting on the Bloch skyrmion is about two orders of magnitude smaller than that on the Néel skyrmion, suggesting a reduced sensitivity to curvature in this case.

6.4 Dynamic of skyrmion on a bent nanotube

To calculate the skyrmion velocity, we first need to obtain the tensors appearing in Eq. (5.36). Since curvature has little effect on the Bloch skyrmion, the dynamical analysis will be restricted to the Néel skyrmion. However, the corresponding equations of motion for the Bloch skyrmion are provided in Appendix B.

In a bent nanotube, the tensors of the generalized Thiele equation for a Néel skyrmion are given by (see Appendix B)

$$G_{ab} = \begin{pmatrix} 0 & G \\ -G & 0 \end{pmatrix}, \quad G = \frac{4\pi\mu_0 M_s h N_{\text{sk}}}{\gamma} \tag{6.13}$$

$$D_{ab} = \begin{pmatrix} D & 0 \\ 0 & D \end{pmatrix}, \quad D = \frac{\pi\mu_0 M_s h}{\gamma} \int_0^\infty \left[\left(\frac{\partial \Theta}{\partial \rho} \right)^2 + \frac{\sin^2 \Theta}{\rho^2} \right] \rho d\rho \tag{6.14}$$

$$G^u_{ab} = \begin{pmatrix} 0 & -G^u_{12} \\ G^u_{21} & 0 \end{pmatrix}, \quad G^u_{\alpha\beta} = \frac{\pi\mu_0 M_s h}{\gamma} b^\alpha_\beta \int_0^\infty \left[\cos\Theta \frac{\partial \Theta}{\partial \rho} + \frac{\sin\Theta}{\rho} \right] \rho d\rho \tag{6.15}$$

$$D^u_{ab} = \begin{pmatrix} -D^u_{11} & 0 \\ 0 & -D^u_{22} \end{pmatrix}, \quad D^u_{\alpha\beta} = \frac{\pi\mu_0 M_s h}{\gamma} b_{\alpha\beta} \int_0^\infty \left[\frac{\partial \Theta}{\partial \rho} + \frac{\sin\Theta\cos\Theta}{\rho} \right] \rho d\rho \tag{6.16}$$

The Néel skyrmion experiences an energy gradient $\partial E / \partial X^2$, which is directly related to the curvature-induced force defined in Eq. (6.9). In addition, the skyrmion is driven by an applied current density along the toroidal direction, i.e., $\boldsymbol{u} = u^1 \boldsymbol{g}_1$. Taking all these contributions into account and substituting the corresponding tensors into Eq. (5.36), the time evolution of the Néel skyrmion position (X^1, X^2) is given by

$$\dot{X}^1 = \frac{G(G - G^{\mathrm{u}}_{21}) + \alpha\beta D(D + D^u_{11})}{\alpha^2 D^2 + G^2} u^1 - \frac{G}{\alpha^2 D^2 + G^2} \frac{\partial E}{\partial X^2}, \tag{6.17}$$

$$\dot{X}^2 = \frac{\alpha D(G - G^u_{21}) - \beta G(D + D^u_{11})}{\alpha^2 D^2 + G^2} u^1 - \frac{\alpha D}{\alpha^2 D^2 + G^2} \frac{\partial E}{\partial X^2}. \tag{6.18}$$

In contrast to the skyrmion velocities in planar geometry, we observe the emergence of additional terms. These terms clearly vanish in the planar limit, such that the final expression reduces to Eqs. (5.6) and (5.7).

Based on these equations, we analyze how the position of the skyrmion evolves over time, i.e. $(\dot{X}^1, \dot{X}^2)$. Due to the complexity of the system of equations, the dynamics were solved numerically. Since the contribution of the tensor G^u_{21} is negligible in this geometry, its influence on the dynamics will not be discussed. This is primarily because the associated field $\boldsymbol{H}^{\mathrm{AD}}$ lies in-plane, resulting in minimal effects on the system's dynamics.

6.4.1 Effects of curvature on the current

For the purpose of analyzing the effects of the additional terms in Eqs. (6.17) and (6.18), we consider a skyrmion propagating in a fully closed bent nanotube under an applied current density along the toroidal direction, ξ^1. The current density is fixed to $J =$

100×10^{11} A/m^2, and we focus on the specific case $\alpha = \beta = 0.5$.

We find that the term G^{u}_{21} does not significantly influence the dynamics. However, the term D^{u}_{11} does modify the motion under these conditions. As shown in Fig. 6.4(a) by the black dashed line, when the D^{u}_{11} term is neglected, the skyrmion should follow a straight trajectory along the toroidal direction, which is typical behavior in flat systems. Nevertheless, when this additional term is taken into account, the skyrmion exhibits a deviation from its initial position along the poloidal direction, ξ^2, during the first 50 ns (purple line). Subsequently, the skyrmion recovers a straight-line trajectory in the time interval between 50 ns and 100 ns. This behavior is reflected in the skyrmion trajectory, which is illustrated in Fig. 6.4(b) by the solid and dashed yellow lines.

This behavior indicates that the skyrmion experiences a new effect induced by the interplay between the applied current and the curvature, arising from the term D^{u}_{11}. This contribution originates from the effective field $\boldsymbol{H}^{\mathrm{nAD}}$, which, in curved geometries, points along the surface normal and is therefore strongly influenced by the local curvature. Consequently, it is reasonable to expect this term to play a more significant role in the skyrmion dynamics.

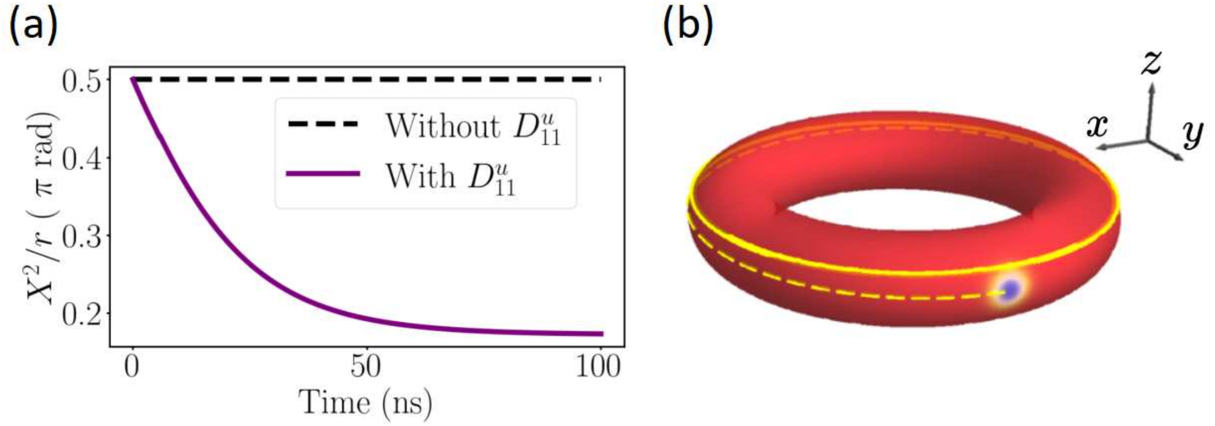

Fig. 6.4: Time dependence of the skyrmion position X^2/r with and without the term D^{u}_{11}. (b) Schematic representation of the skyrmion trajectory on a toroidal nanotube during the first 100 ns.

We now analyze what happens to the poloidal position of the skyrmion when the damping constant α is varied around a fixed value of $\beta = 0.5$, for different current intensities. As shown in Fig. 6.5(a), for a current density of $J = 100 \times 10^{11}$ A/m^2, the skyrmion becomes trapped in different regions whenever $\alpha \in [0.49, 0.51]$. This indicates that the SkHE is suppressed even for values where $\alpha \neq \beta$.

Although the range of α where this suppression occurs is close to β, decreasing the current leads to a considerable expansion of the interval. In Fig. 6.5(b), the case for $J = 30 \times 10^{11}$ A/m^2 is shown, where the range of α for which the SkHE is suppressed broadens to $\alpha \in [0.48, 0.53]$. Finally, for a current of $J = 10 \times 10^{11}$ A/m^2, shown in

Fig. 6.5(c), this range significantly increases to $\alpha \in [0.43, 0.62]$, with the suppression being more favorable when $\alpha > \beta$. This result is particularly important because, given that it is experimentally challenging to obtain materials with $\alpha = \beta$ to suppress the SkHE, it would be sufficient to curve the system using realistic experimental parameters to achieve this effect. These results demonstrate that the SkHE can be suppressed purely through curvature, even under conditions of relatively high currents. This opens an experimentally viable pathway for controlling the topological transport of skyrmions in curved systems, without requiring fine-tuning of material parameters, and with direct potential for spintronic applications.

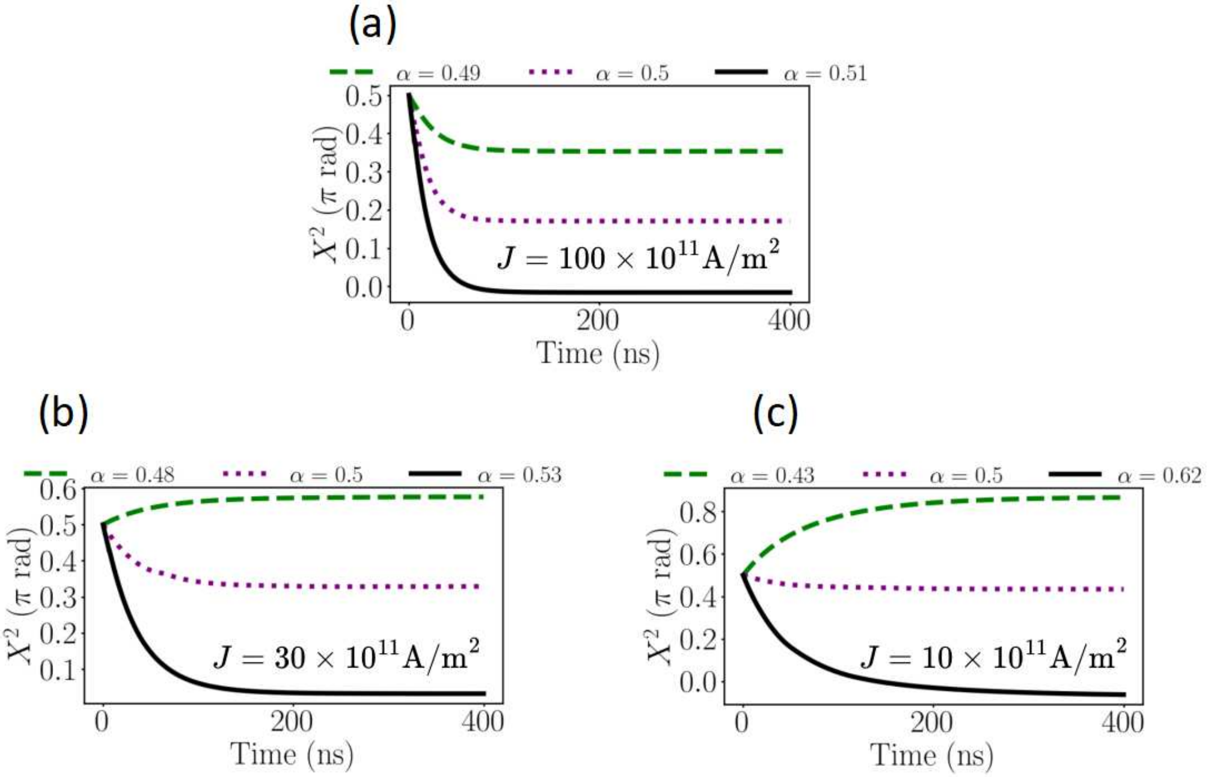

Fig. 6.5: Time evolution of the poloidal position X^2 for different values of damping constant α, considering three current densities: (a) $J = 100 \times 10^{11}$ A/m^2, (b) $J = 30 \times 10^{11}$ A/m^2, and (c) $J = 10 \times 10^{11}$ A/m^2. The results show that the suppression of the SkHE.

6.4.2 Nonlinear dynamical regime

For a low damping value of $\alpha = 0.02$ and $\beta = 0.5$, the terms D^{u}_{ab} and G^{u}_{ab} have a negligible influence on the skyrmion dynamics. Consequently, the motion is primarily governed by the competition between the SkHE and the energy gradient, $\partial E/\partial X^a$. We apply a fixed current density of $J = 3 \times 10^{11}$ A/m^2 to nanotubes with different bending configurations. As shown in Fig. 6.6(a), we analyze the skyrmion displacement along the toroidal direction, ΔX^1. For $\psi = \pi/32$, the skyrmion follows a helical-type trajectory,

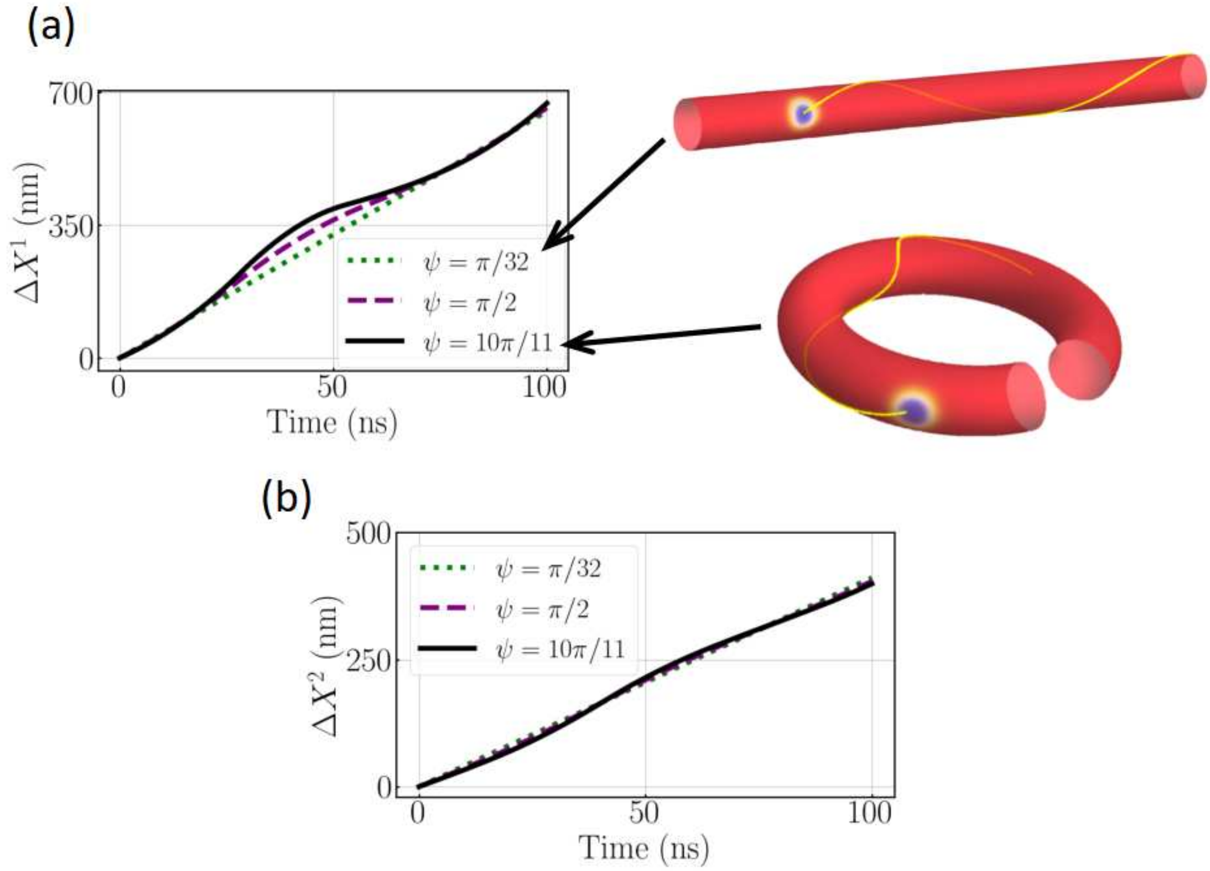

Fig. 6.6: (a) Time evolution of the skyrmion displacement ΔX^1 for different curvature parameters ψ, with the corresponding skyrmion trajectories on the nanotube shown in the insets. (b) Skyrmion displacement ΔX^2 along the poloidal direction.

characterized by a linear relationship between position and time. However, as the curvature increases up to $\psi = 10\pi/11$, the skyrmion exhibits a nonlinear time evolution, with the nonlinear behavior becoming pronounced at approximately 40 ns.

Moreover, Fig. 6.6(b) shows that increasing the curvature does not lead to a noticeable variation in the skyrmion displacement along the poloidal direction, indicating that the skyrmion Hall effect remains essentially independent of curvature in this regime.

We now fix the parameters α and β, and consider a constant curvature of $\psi = \frac{10\pi}{11}$. Under this configuration, we analyze the effects of three different current densities: $J = 1 \times 10^{11}$ A/m^2, $J = 3 \times 10^{11}$ A/m^2, and $J = 5 \times 10^{11}$ A/m^2. As shown in Fig. 6.7(a), for a current of $J = 5 \times 10^{11}$ A/m^2, the skyrmion undergoes two rebounds, while for $J = 1 \times 10^{11}$ A/m^2, no rebound is observed within the first 100 ns. This indicates that, for a fixed curvature, increasing the current enhances the rebound frequency.

Moreover, Fig. 6.7(b) shows that the skyrmion velocity in the poloidal direction decreases as the current is reduced, and increases with higher current. This behavior highlights the direct dependence between current magnitude and the skyrmion's propagation speed in this direction.

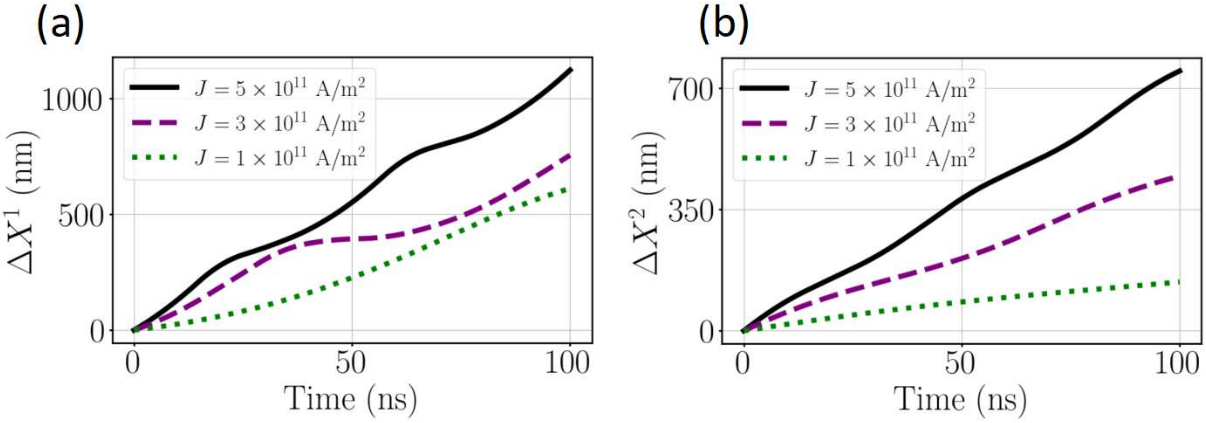

Fig. 6.7: Time evolution of the Néel skyrmion position under different current densities in a bent nanotube with curvature $\psi = \frac{10\pi}{11}$. (a) Toroidal direction X^1; (b) Poloidal direction X^2.

6.5 Micromagnetic simulations

6.5.1 Software

To validate our results, we perform micromagnetic simulations using the *open-source* software `tetmag` [51]. `tetmag` is a finite-element micromagnetic solver specifically designed for simulations in complex geometries, including curved and three-dimensional nanostructures. This makes it particularly well-suited for studying magnetization dynamics in geometries such as nanotubes and toroidal surfaces (see Fig. 6.8), where curvature plays a fundamental role in the physical behavior.

Fig. 6.8: Discretized representation of a cylindrical magnetic nanotube geometry used in `tetmag`. Figure adapted from [52].

In micromagnetic simulations, the spatial discretization method plays a central role in determining the accuracy and efficiency of the numerical solution. The two most widely used approaches are the Finite Difference Method (FDM) and the Finite Element Method (FEM), each with its own strengths and limitations.

Micromagnetic solvers like Mumax^3 [53] or Boris [54] are based on FDM, which assumes a regular, rectangular grid of uniformly spaced cells (see Fig. 6.9) This method is simple, computationally efficient, and easy to parallelize on GPUs. However, FDM suffers from important limitations when dealing with nontrivial geometries, such as curved or irregular surfaces. In such cases, the underlying grid cannot conform to the sample shape, leading to inaccuracies near boundaries or interfaces.

In contrast, `tetmag` uses FEM, which discretizes the system into irregular tetrahedral elements (see Fig. 6.9), allowing precise representation of arbitrary three-dimensional geometries and curvature. This geometric flexibility is crucial for studying systems like nanotubes or toroidal structures, where the curvature directly affects the magnetization dynamics.

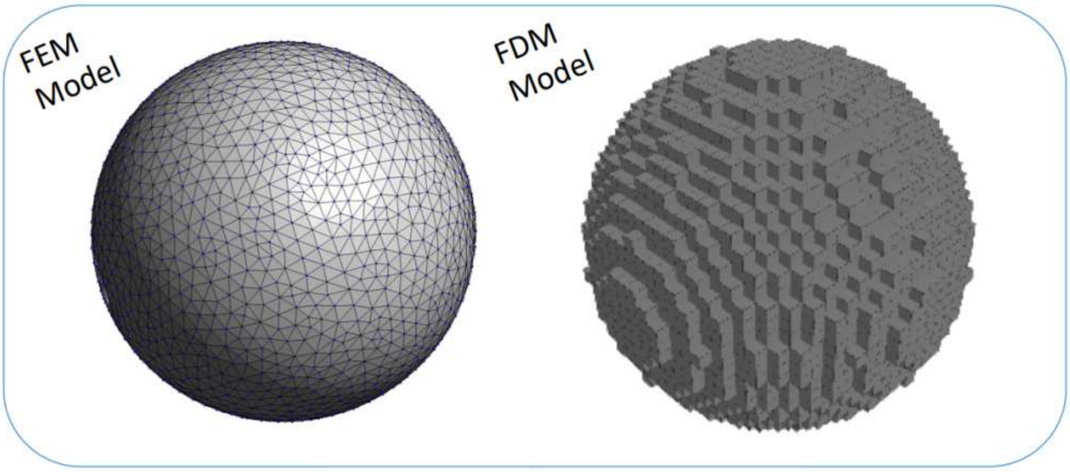

Fig. 6.9: Comparison between two discretization methods commonly used in micromagnetism. The FEM model (left) allows smooth and accurate representation of curved geometries, while the FDM model (right) approximates the surface using a staircase-like grid. Figure adapted from [52].

6.5.2 Simulation

In our simulations, we used the parameters established for the Co/Pt/AOx system: saturation magnetization $M_s = 1.09817\times10^6$ A/m, exchange stiffness $A = 1.6\times10^{-11}$ J/m, and interfacial DMI constant $D^{(i)} = 2.8 \times 10^{-3}$ J/m^2.

Due to the long simulation times (around 100 ns), the demagnetization energy was not included. Therefore, the uniaxial anisotropy constant was adjusted from $K_u = 1.4 \times 10^6$ J/m^3 to $K_u = 5.6 \times 10^5$ J/m^3 in the simulations. A thickness of 2 nm was considered.

Figure 6.10 shows the comparison between the theoretical results and those obtained from simulations for the skyrmion position (X^1 and X^2) as a function of time, under different current densities J, with $\alpha = 0.02$, $\beta = 0.5$, and $P = 0.5$.

As shown in Fig. 6.10(a), for $J = 3 \times 10^{11}$ A/m^2, theoretical and numerical results are in excellent agreement for both ΔX^1 and ΔX^2. A similar agreement is observed for $J = 5 \times 10^{11}$ A/m^2, as shown in Fig. 6.10(b).

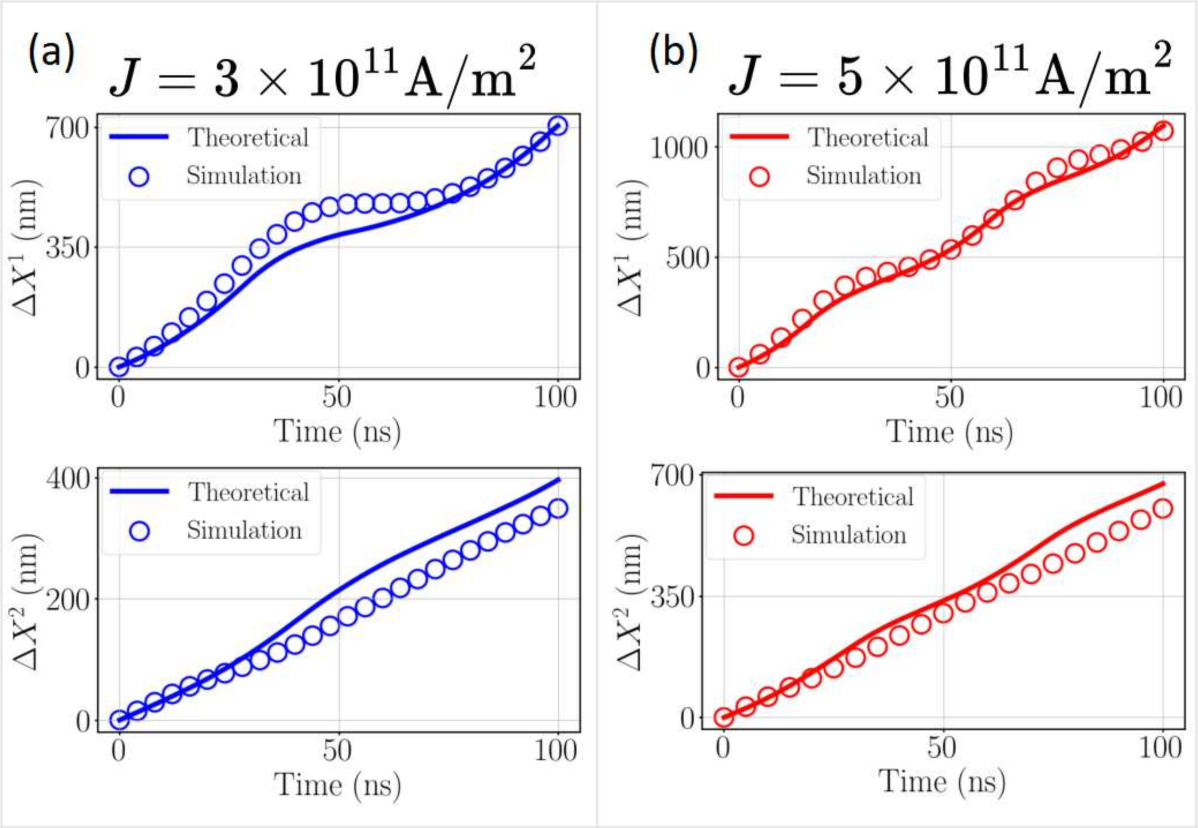

Fig. 6.10: Comparison between theoretical and simulation results for the skyrmion displacament ΔX^1 and ΔX^2 as a function of time. (a) $J = 3 \times 10^{11}$ A/m^2 and (b) $J = 5 \times 10^{11}$ A/m^2

We also performed simulations to investigate the combined effects of current and curvature. The parameters were fixed to $\alpha = \beta = 0.5$, for which theory predicts purely toroidal skyrmion motion. However, as shown in Fig. 6.11, our simulations reveal a clear deviation from the toroidal trajectory when a current density of 100×10^{11} A/m^2 is applied, thereby confirming the emergence of a curvature–current–induced effect on the skyrmion dynamics.

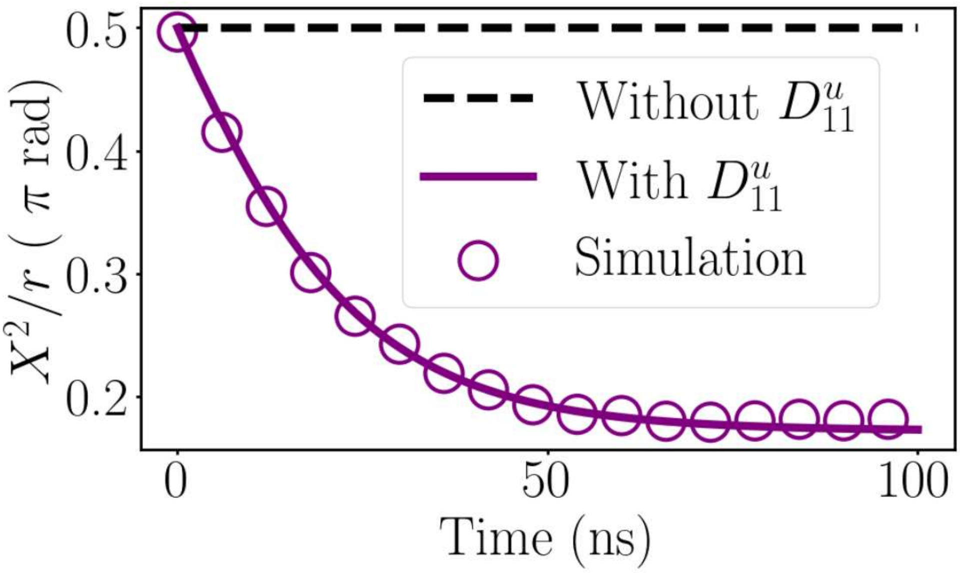

Fig. 6.11: Deviation of skyrmion trajectory from the toroidal direction under a current density $J = 100 \times 10^{11}$ A/m^2 with $\alpha = \beta = 0.5$.

Chapter 7

Conclusions and perspectives

7.1 Conclusions

In this work, we have developed a generalized version of the Thiele equation to describe the dynamics of skyrmions on arbitrarily curved surfaces under the influence of STT. This formulation incorporates geometric effects through the emergence of new curvature–current coupling terms, represented by the tensors G^{u}_{ab} and D^{u}_{ab}.

Our static analysis shows that curvature significantly alters the properties of skyrmions, with distinct effects for Néel and Bloch configurations. In particular, Néel skyrmions exhibit a much higher sensitivity to curvature compared to Bloch skyrmions, making them more stable in a bent nanotube.

In the dynamical regime, at a current density of $J = 100 \times 10^{11}\,\mathrm{A/m^2}$, we identify a curvature-induced effect governed by the tensor D^{u}_{ab}, which leads to a deviation of the skyrmion trajectory along the poloidal direction. Remarkably, this deviation occurs even under the condition $\alpha = \beta$, for which no transverse motion is expected in planar systems. This result highlights the crucial role of D^{u}_{ab} in mediating the interplay between current and curvature in high-current regimes.

We further examined the influence of the damping parameter α on the poloidal position of the skyrmion. The results show that, even when $\alpha \neq \beta$, there exists a finite parameter interval in which the skyrmion Hall effect (SkHE) is suppressed. This interval broadens as the current density is reduced, spanning a wider range of α values, with the suppression being more effective for $\alpha > \beta$.

Overall, these findings demonstrate that the introduction of curvature provides an effective mechanism to suppress the SkHE in parameter regimes where such suppression cannot be achieved in planar geometries. This offers a robust and practical route for controlling topological skyrmion transport in curved magnetic systems.

In addition, for lower current densities of $J = 3 \times 10^{11}$ and $5 \times 10^{11}\,\mathrm{A/m^2}$, Néel skyrmions exhibit nonlinear dynamical behavior induced by the strong curvature of the bent nanotube with $\psi = 10\pi/11$. For a fixed high curvature, increasing the current density results in a higher rebound frequency of the skyrmion and a pronounced modification of its propagation velocity.

7.2 Perspectives

In this study, a system was analyzed where the spin-polarized current is perpendicular to the direction of curvature. However, the question arises: what would happen in systems where the current is parallel to the curvature? For example, Bittencourt *et al.* [49] demonstrated that such one-dimensional systems can induce a chiral spin-transfer torque (CSTT), which generates non-reciprocity in the domain wall motion: the direction in which the DW points determines whether its propagation is favored or blocked. Therefore, it is proposed to explore this type of geometry in the context of skyrmions, with the expectation of finding analogous effects.

Likewise, Carvalho-Santos *et al.* [46] reported that on surfaces with Gaussian bumps, skyrmions can become confined to certain positions depending on the value of the DMI. Since our theory controls motion in all directions, the question arises: what would happen if the system were closed, similar to a straight nanotube but with a modulated radius? Such a system would induce a helical motion of the skyrmions, so that specific DMI values could help confine skyrmions in certain regions, causing them to circulate indefinitely. Furthermore, as the curvature is parallel to the applied current, new effects would be induced that could be exploited to create current-dependent devices, such as skyrmion diodes.

Beyond skyrmions, the present study is applicable to other magnetic topological structures, as the equations only require modifying the corresponding ansatz. Moreover, these structures are governed by the same micromagnetic equations on curved surfaces, making this theoretical approach a powerful analytical tool.

Bibliography

[1] B. Li, T. Wang, P. Yang, M. Chen, S. Yu, and M. Hamdi, “Machine learning empowered intelligent data center networking: A survey,” 2022.

[2] I. Žutić, J. Fabian, and S. Das Sarma, “Spintronics: Fundamentals and applications,” *Rev. Mod. Phys.*, vol. 76, pp. 323–410, Apr 2004.

[3] G. Finocchio, F. Büttner, R. Tomasello, M. Carpentieri, and M. Kläui, “Magnetic skyrmions: from fundamental to applications,” *Journal of Physics D Applied Physics*, vol. 49, p. 423001, Oct. 2016.

[4] A. Fert, N. Reyren, and V. Cros, “Magnetic skyrmions: advances in physics and potential applications,” *Nature Reviews Materials*, vol. 2, p. 17031, 2017.

[5] S. Mühlbauer, B. Binz, F. Jonietz, C. Pfleiderer, A. Rosch, A. Neubauer, R. Georgii, and P. Böni, “Skyrmion lattice in a chiral magnet,” *Science*, vol. 323, no. 5916, pp. 915–919, 2009.

[6] R. Tomasello, E. Martinez, R. Zivieri, L. Torres, M. Carpentieri, and G. Finocchio, “A strategy for the design of skyrmion racetrack memories,” *Scientific Reports*, vol. 4, p. 6784, 2014.

[7] S. S. P. Parkin, M. Hayashi, and L. Thomas, “Magnetic domain-wall racetrack memory,” *Science*, vol. 320, no. 5873, pp. 190–194, 2008.

[8] S. Luo and L. You, “Skyrmion devices for memory and logic applications,” *APL Materials*, vol. 9, no. 5, p. 050901, 2021.

[9] N. Nagaosa and Y. Tokura, “Topological properties and dynamics of magnetic skyrmions,” *Nature nanotechnology*, vol. 8, pp. 899–911, 12 2013.

[10] F. Albert, V. Cros, and J. Sampaio, “Skyrmions on the track,” *Nature nanotechnology*, vol. 8, pp. 152–6, 03 2013.

[11] R. Streubel, P. Fischer, F. Kronast, V. P. Kravchuk, D. D. Sheka, Y. Gaididei, O. G. Schmidt, and D. Makarov, “Magnetism in curved geometries,” *Journal of Physics D: Applied Physics*, vol. 49, p. 363001, aug 2016.

[12] D. D. S. Denys Makarov, *Curvilinear Micromagnetism: From Fundamentals to Applications.* Topics in Applied Physics, 146, Springer, 2022.

[13] V. L. Carvalho-Santos, R. M. Corona, D. Altbir, and S. Castillo-Sepúlveda, "Shifts in the skyrmion stabilization due to curvature effects in dome- and antidome-shaped surfaces," *Phys. Rev. B*, vol. 102, p. 024444, Jul 2020.

[14] O. V. Pylypovskyi *et al.*, "Chiral skyrmion and skyrmionium states engineered by the gradient of curvature," *Phys. Rev. Appl.*, vol. 10, p. 064057, 2018.

[15] D. A. Dugato *et al.*, "Curved nanomagnets: An archetype for the skyrmionic states at ambient conditions," *Nano Letters*, 2025.

[16] X. Wang, X. S. Wang, C. Wang, H. Yang, Y. Cao, and P. Yan, "Current-induced skyrmion motion on magnetic nanotubes," *Journal of Physics D: Applied Physics*, vol. 52, p. 225001, mar 2019.

[17] Z. J. C. V. H. AF, *Topology in Magnetis.* Springer, 2018.

[18] J. Yang, C. Abert, D. Suess, *et al.*, "Intrinsic dmi-free skyrmion formation and robust dynamic behaviors in magnetic hemispherical shells," *Scientific Reports*, vol. 11, p. 3886, 2021.

[19] V. P. Kravchuk, D. D. Sheka, A. Kákay, O. M. Volkov, U. K. Rößler, J. van den Brink, D. Makarov, and Y. Gaididei, "Multiplet of skyrmion states on a curvilinear defect: Reconfigurable skyrmion lattices," *Phys. Rev. Lett.*, vol. 120, p. 067201, Feb 2018.

[20] W. Brown, *Micromagnetics, by w.f. brown.* Interscience, 1963.

[21] S. Blundell, *Magnetism in Condensed Matter.* Oxford Master Series in Condensed Matter Physics, OUP Oxford, 2001.

[22] R. Skomski, *Micromagnetic Spin Structure*, pp. 204–231. Berlin, Heidelberg: Springer Berlin Heidelberg, 2001.

[23] I. Dzyaloshinsky, "A thermodynamic theory of "weak" ferromagnetism of antiferromagnetics," *Journal of Physics and Chemistry of Solids*, vol. 4, pp. 241–255, Jan. 1958.

[24] T. Moriya, "Anisotropic superexchange interaction and weak ferromagnetism," *Phys. Rev.*, vol. 120, pp. 91–98, Oct 1960.

[25] O. M. Volkov, D. D. Sheka, Y. Gaididei, V. P. Kravchuk, U. K. Rößler, J. Fassbender, and D. Makarov, "Mesoscale Dzyaloshinskii–Moriya interaction: geometrical tailoring of the magnetochirality," *Scientific Reports*, vol. 8, no. 1, p. 866, 2018.

[26] A. Thiaville, S. Rohart, É. Jué, V. Cros, and A. Fert, "Dynamics of dzyaloshinskii domain walls in ultrathin magnetic films," *EPL (Europhysics Letters)*, vol. 100, p. 57002, dec 2012.

[27] H. Yang, A. Thiaville, S. Rohart, A. Fert, and M. Chshiev, "Anatomy of dzyaloshinskii-moriya interaction at Co/Pt interfaces," *Phys. Rev. Lett.*, vol. 115, p. 267210, Dec 2015.

[28] T. Gilbert, "A phenomenological theory of damping in ferromagnetic materials," *IEEE Transactions on Magnetics*, vol. 40, no. 6, pp. 3443–3449, 2004.

[29] L. D. Landau and E. Lifshitz, "On the theory of the dispersion of magnetic permeability in ferromagnetic bodies," *Phys. Z. Sowjetunion*, vol. 8, pp. 153–169, 1935.

[30] T. Devolder, S. Couet, J. Swerts, and G. S. Kar, "Gilbert damping of high anisotropy co/pt multilayers," *Journal of Physics D: Applied Physics*, vol. 51, p. 135002, Mar. 2018.

[31] J. A. King, A. Ganguly, D. M. Burn, S. Pal, E. A. Sallabank, T. P. A. Hase, A. T. Hindmarch, A. Barman, and D. Atkinson, "Local control of magnetic damping in ferromagnetic/non-magnetic bilayers by interfacial intermixing induced by focused ion-beam irradiation," *Applied Physics Letters*, vol. 104, p. 242410, 06 2014.

[32] X. Zhang, J. Xia, G. P. Zhao, X. Liu, and Y. Zhou, "Magnetic skyrmion transport in a nanotrack with spatially varying damping and non-adiabatic torque," *IEEE Transactions on Magnetics*, vol. 53, no. 3, pp. 1–6, 2017.

[33] S. Zhang and Z. Li, "Roles of nonequilibrium conduction electrons on the magnetization dynamics of ferromagnets," *Phys. Rev. Lett.*, vol. 93, p. 127204, Sep 2004.

[34] J.-C. Lee, K.-J. Kim, J. Ryu, K.-W. Moon, S.-J. Yun, G.-H. Gim, K.-S. Lee, K.-H. Shin, H.-W. Lee, and S.-B. Choe, "Universality classes of magnetic domain wall motion," *Phys. Rev. Lett.*, vol. 107, p. 067201, Aug 2011.

[35] K. Gilmore, I. Garate, A. H. MacDonald, and M. D. Stiles, "First-principles calculation of the nonadiabatic spin transfer torque in ni and fe," *Phys. Rev. B*, vol. 84, p. 224412, Dec 2011.

[36] D. Makarov, M. Melzer, D. Karnaushenko, and O. G. Schmidt, "Shapeable magnetoelectronics," *Applied Physics Reviews*, vol. 3, p. 011101, 01 2016.

[37] P. Grinfeld, *Introduction to Tensor Analysis and the Calculus of Moving Surfaces.* New York: Springer, 2010.

[38] A. Korniienko, A. Kákay, D. D. Sheka, and V. P. Kravchuk, "Effect of curvature on the eigenstates of magnetic skyrmions," *Phys. Rev. B*, vol. 102, p. 014432, Jul 2020.

[39] X. S. Wang, H. Y. Yuan, and X. R. Wang, "A theory on skyrmion size," *Communications Physics*, vol. 1, p. 31, July 2018.

[40] K. V. Yershov, A. Kákay, and V. P. Kravchuk, "Curvature-induced drift and deformation of magnetic skyrmions: Comparison of the ferromagnetic and antiferromagnetic cases," *Phys. Rev. B*, vol. 105, p. 054425, Feb 2022.

[41] J. Iwasaki, M. Mochizuki, and N. Nagaosa, "Current-induced skyrmion dynamics in constricted geometries," *Nature Nanotechnology*, vol. 8, pp. 742–747, 2013.

[42] X. Z. Yu, D. Morikawa, K. Nakajima, K. Shibata, N. Kanazawa, T. Arima, N. Nagaosa, and Y. Tokura, "Motion tracking of 80-nm-size skyrmions upon directional current injections," *Science Advances*, vol. 6, no. 25, p. eaaz9744, 2020.

[43] G. Qin, X. Zhang, R. Zhang, K. Pei, C. Yang, C. Xu, Y. Zhou, Y. Wu, H. Du, and R. Che, "Dynamics of magnetic skyrmions driven by a temperature gradient in a chiral magnet fege," *Phys. Rev. B*, vol. 106, p. 024415, Jul 2022.

[44] A. A. Thiele, "Steady-state motion of magnetic domains," *Phys. Rev. Lett.*, vol. 30, pp. 230–233, Feb 1973.

[45] I. Garate, K. Gilmore, M. D. Stiles, and A. H. MacDonald, "Non-adiabatic spin transfer torque in real materials," *Physical Review B*, vol. 79, no. 10, p. 104416, 2009.

[46] V. L. Carvalho-Santos, M. A. Castro, D. Salazar-Aravena, D. Laroze, R. M. Corona, S. Allende, and D. Altbir, "Skyrmion propagation along curved racetracks," *Applied Physics Letters*, vol. 118, p. 172407, 04 2021.

[47] O. A. Tretiakov, D. Clarke, G.-W. Chern, Y. B. Bazaliy, and O. Tchernyshyov, "Dynamics of domain walls in magnetic nanostrips," *Phys. Rev. Lett.*, vol. 100, p. 127204, Mar 2008.

[48] A. Thiaville, Y. Nakatani, J. Miltat, and Y. Suzuki, "Micromagnetic understanding of current-driven domain wall motion in patterned nanowires," *Europhysics Letters (EPL)*, vol. 69, no. 6, pp. 990–996, 2005.

[49] G. H. R. Bittencourt, M. Castro, A. S. Nunez, D. Altbir, S. Allende, and V. L. Carvalho-Santos, "Chiral spin-transfer torque induced by curvature gradient," *Nanoscale*, vol. 16, pp. 16844–16851, 2024.

[50] Y. Gaididei, V. P. Kravchuk, and D. D. Sheka, “Curvature effects in thin magnetic shells,” *Phys. Rev. Lett.*, vol. 112, p. 257203, Jun 2014.

[51] R. Hertel, “tetmag,” 2023. Numerical tool for topological magnetism.

[52] R. Hertel, “Tetmag - topological effects in magnetism: Part 1.” `https://scienceouverte.unistra.fr/websites/science-ouverte/science_ouverte/fichiers_23/tetmag_presentation_HERTEL_part1.pdf`, 2023. Presentation from the TETMAG doctoral school, 2023.

[53] A. Vansteenkiste, J. Leliaert, M. Dvornik, M. Helsen, F. Garcia-Sanchez, and B. Van Waeyenberge, “The design and verification of mumax3,” *AIP Advances*, vol. 4, p. 107133, 10 2014.

[54] S. Lepadatu, “Boris computational spintronics—high performance multi-mesh magnetic and spin transport modeling software,” *Journal of Applied Physics*, vol. 128, p. 243902, 12 2020.

Appendix A

Micromagnetic energy of a skyrmion in bent nanotubes

To determine the skyrmion energy on a curved system, one can adopt the planar approximation to the skyrmion profile and calculate the quantities $\frac{\partial \boldsymbol{m}}{\partial \xi^1}$ and $\frac{\partial \boldsymbol{m}}{\partial \xi^1}$. The derivatives of the magnetization with respect to the coordinates (ξ^1, ξ^2) can be obtained through the chain rule in the form

$$\frac{\partial \boldsymbol{m}}{\partial \xi^\alpha} = \frac{\partial \boldsymbol{m}}{\partial \rho}\frac{\partial \rho}{\partial \xi^\alpha} + \frac{\partial \boldsymbol{m}}{\partial \chi}\frac{\partial \chi}{\partial \xi^\alpha}, \tag{A.1}$$

where $\alpha = \{1, 2\}$, $\sqrt{g_{11}}(\xi^1 - X^1) = \rho\cos\chi$, and $\sqrt{g_{22}}(\xi^2 - X^2) = \rho\sin\chi$.

Explicitly for the case of a Néel skyrmion, we have $\Phi(\chi) = \chi$, so that

$$\begin{aligned} m^1 &= \frac{\sin\Theta(\rho)\cos\Phi(\chi)}{\sqrt{g_{11}}} &&= \frac{m_\rho\cos\chi}{\sqrt{g_{11}}} \\ m^2 &= \frac{\sin\Theta(\rho)\sin\Phi(\chi)}{\sqrt{g_{22}}} &&= \frac{m_\rho\sin\chi}{\sqrt{g_{22}}} \\ m^3 &= \cos\Theta(\rho) &&= m_z. \end{aligned} \tag{A.2}$$

Therefore, the substitution of Eqs. (A.2) in (A.1), we obtain

$$\frac{\partial \boldsymbol{m}}{\partial \xi^1} = \begin{pmatrix} \partial_1 m^1 \\ \partial_1 m^2 \\ \partial_1 m^3 \end{pmatrix} = \begin{pmatrix} \frac{\partial \boldsymbol{m}_\rho}{\partial \rho}\cos^2\chi + \frac{m_\rho}{\rho}\sin^2\chi \\ \sqrt{\frac{g_{11}}{g_{22}}}\left(\frac{\partial \boldsymbol{m}_\rho}{\partial \rho}\sin\chi\cos\chi - \frac{m_\rho}{\rho}\sin\chi\cos\chi\right) \\ \sqrt{g_{11}}\frac{\partial \boldsymbol{m}_z}{\partial \rho}\cos\chi \end{pmatrix} \tag{A.3}$$

and

$$\frac{\partial \boldsymbol{m}}{\partial \xi^2} = \begin{pmatrix} \partial_2 m^1 \\ \partial_2 m^2 \\ \partial_2 m^3 \end{pmatrix} = \begin{pmatrix} \sqrt{\frac{g_{22}}{g_{11}}}\left(\frac{\partial \boldsymbol{m}_\rho}{\partial \rho}\sin\chi\cos\chi - \frac{m_\rho}{\rho}\sin\chi\cos\chi\right) \\ \frac{\partial \boldsymbol{m}_\rho}{\partial \rho}\sin^2\chi + \frac{m_\rho}{\rho}\cos^2\chi \\ \sqrt{g_{22}}\frac{\partial \boldsymbol{m}_z}{\partial \rho}\sin\chi \end{pmatrix} \tag{A.4}$$

Exchange energy

The total exchange energy in a curved geometry can be decomposed into three distinct contributions, being written in the form

$$\begin{aligned} E^{\mathrm{X}} &= Ah \int_{-L/2}^{L/2} \int_{-\pi}^{\pi} [\mathscr{E}_0^{\mathrm{X}} + \mathscr{E}_A^{\mathrm{X}} + \mathscr{E}_D^{\mathrm{X}}] \sqrt{g} d\xi^1 d\xi^2 \\ &= Ah\, [E_0^{\mathrm{X}} + E_A^{\mathrm{X}} + E_D^{\mathrm{X}}], \end{aligned} \tag{A.5}$$

where first, second, and third terms are respectively the isotropic-like and the curvature-induced anisotropy, and the Dzyaloshinsky-Moriya interactions. The isotropic exchange density $\mathscr{E}_0^{\mathrm{X}}$ reads

$$\begin{aligned} \mathscr{E}_0^{\mathrm{X}} &= (\partial_1 m^1)^2 + g^{11} g_{22} (\partial_1 m^2)^2 + g_{11} g^{22} (\partial_2 m^1)^2 + (\partial_2 m^2)^2 \\ &\quad + g^{11} (\partial_1 m^3)^2 + g^{22} (\partial_2 m^3)^2 \,, \end{aligned} \tag{A.6}$$

from which one can derive the isotropic energy term

$$\begin{aligned} E_0^{\mathrm{X}} &= 2\pi \int_0^\infty \left[\left(\frac{\partial m_\rho}{\partial \rho} \right)^2 + \left(\frac{m_\rho}{\rho} \right)^2 + \left(\frac{\partial m_z}{\partial \rho} \right)^2 \right] \rho \; d\rho \\ &= 2\pi \int_0^\infty \left[\left(\frac{\partial \Theta}{\partial \rho} \right)^2 + \frac{\sin^2 \Theta}{\rho^2} \right] \rho \, d\rho \,. \end{aligned} \tag{A.7}$$

This contribution to the exchange energy vanishes when $\Theta = 0\,(\pi)$, what means that the magnetization points along the **n**-direction. Because **n** does not necessarily define a vector field whose vectors are parallel transported into each other on a curved manifold, the is the emergence of curvature-induced interactions, given by $\mathscr{E}_A^{\mathrm{X}}$ and $\mathscr{E}_D^{\mathrm{X}}$.

The curvature-induced anisotropy density is given by

$$\begin{aligned} \mathscr{E}_A^{\mathrm{X}} &= A b_\gamma^\alpha b_\beta^\gamma m_\alpha m^\beta + A b_\beta^\alpha b_\alpha^\beta m_3 m^3 \\ &= b_1^1 b_1^1 m_1 m^1 + b_2^2 b_2^2 m_2 m^2 + (b_1^1 b_1^1 + b_2^2 b_2^2) m_3 m^3 \,, \end{aligned} \tag{A.8}$$

which can be simplified to yield

$$\begin{aligned} E_A^{\mathrm{X}} &= \int_{-L/2}^{L/2} \int_{-\pi}^{\pi} \{ [b_1^1]^2 m_\rho^2 \sin^2 \chi + [b_2^2]^2 m_\rho^2 \cos^2 \chi + ([b_1^1]^2 + [b_2^2]^2) m_z^2 \} \sqrt{g}\, d\xi^1 d\xi^2 \\ &= \int_{-L/2}^{L/2} \int_{\pi}^{\pi} \{ -\pi [\mathscr{H}^2(\xi^2) - 2\mathcal{K}(\xi^2)] \sin^2 \Theta + \mathscr{H}^2(\xi^2) - 2\mathcal{K}(\xi^2) \} \sqrt{g}\, d\xi^1 d\xi^2 \,. \end{aligned} \tag{A.9}$$

The $\mathscr{H}(\xi^2)$ and $\mathcal{K}(\xi^2)$ are the Gaussian and mean curvatures, and can be expanded around a fixed reference point X^2 as follows

$$\mathscr{H}(\xi^2) = \mathscr{H}(X^2) + \frac{\rho \sin\chi}{\sqrt{g_{22}}}\,\mathscr{H}'(X^2) + \frac{1}{2}\left(\frac{\rho\sin\chi}{\sqrt{g_{22}}}\right)^2 \mathscr{H}''(X^2) + \cdots\,, \tag{A.10}$$

and

$$\mathcal{K}(\xi^2) = \mathcal{K}(X^2) + \frac{\rho \sin\chi}{\sqrt{g_{22}}}\,\mathcal{K}'(X^2) + \frac{1}{2}\left(\frac{\rho\sin\chi}{\sqrt{g_{22}}}\right)^2 \mathcal{K}''(X^2) + \cdots\,. \tag{A.11}$$

where prime represents derivatives with respect to X^2, and we have kept only the zeroth-order term. This is sufficient to describe the influence of curvature on the skyrmion energy. Throughout this work, we adopt the notation $\mathscr{H}(X^2) = \mathscr{H}$ and $\mathcal{K}(X^2) = \mathcal{K}$. Under this assumption, the induced anisotropy is simplified to

$$E_A^{\mathrm{X}} = -\pi[\mathscr{H}^2 - 2\mathcal{K}] \int_0^\infty \sin^2\Theta\ \rho\, d\rho\, d\chi + \mathbb{N} \tag{A.12}$$

where $\mathbb{N} = \int_{-L/2}^{L/2}\int_{-\pi}^{\pi}[\mathscr{H}^2(\xi^2) - 2\mathcal{K}(\xi^2)]\sqrt{g}\,d\xi^1\,d\xi^2$ is a function that depends on the curvature, accounting as a shift in the skyrmion position-dependent term of E_A^{X}.

Finally, the curvature-induced DMI density ($\mathscr{E}_D^{\mathrm{X}}$) is given by:

$$\begin{aligned}\mathscr{E}_D^{\mathrm{X}} &= 2b^\alpha_\beta(m^\beta\bar{\partial}_\alpha m_3 - m^3\bar{\partial}_\alpha m^\beta)\\ &= 2(b^1_1 m^1\partial_1 m^3 + b^2_2 m^2\partial_2 m^3 - b^1_1 m^3\partial_1 m^1 - b^2_2 m^3\partial_2 m^2)\,.\end{aligned} \tag{A.13}$$

After some algebraic manipulation, this contribution to the exchange energy reads

$$\begin{aligned}E_D^{\mathrm{X}} = 2\int_{-L/2}^{L/2}\int_{-\pi}^{\pi}\Bigg[& b^1_1 m_\rho \frac{\partial m_\rho}{\partial\rho}\cos^2\chi + b^2_2 m_\rho\frac{\partial m_\rho}{\partial\rho}\sin^2\chi - b^1_1 m^z\left(\frac{\partial m_\rho}{\partial\rho}\cos^2\chi + \frac{m_\rho}{\partial\rho}\sin^2\chi\right)\\ &- b^2_2 m_z\left(\frac{\partial m_\rho}{\partial\rho}\sin^2\chi + \frac{m_\rho}{\partial\rho}\cos^2\chi\right)\Bigg]\rho\ d\rho d\chi\\ = -2\pi\mathscr{H}&\int_0^\infty\left(\frac{\partial\Theta}{\partial\rho} + \frac{\sin\Theta\cos\Theta}{\rho}\right)\rho\,d\rho\,.\end{aligned} \tag{A.14}$$

Therefore, the complete expression of the exchange energy of a Néel skyrmion is

$$E^X(X^2) = 2\pi A h\left[C_0 - \frac{\mathscr{H}^2 - 2\mathcal{K}}{2}C_1 - \mathscr{H}C_2 + \frac{\mathbb{N}}{2\pi}\right] \tag{A.15}$$

where the constants C_0, C_1 and C_2 are defined as

$$C_0 = \int_0^\infty\left[\left(\frac{\partial\Theta}{\partial\rho}\right)^2 + \frac{\sin^2\Theta}{\rho^2}\right]\rho d\rho \tag{A.16}$$

$$C_1 = \int_0^\infty \sin^2\Theta \rho d\rho \tag{A.17}$$

$$C_2 = \int_0^\infty \left(\frac{\partial\Theta}{\partial\rho} + \frac{\sin\Theta\cos\Theta}{\rho} \right) \rho d\rho \tag{A.18}$$

DMI energy

To continue our analysis, we adopt the fact that the intrinsic DMI interaction also experiences curvature effects, so that the interfacial DMI energy in a curved geometry is given by two contributions, in the form

$$\begin{aligned} E^{\mathrm{DMI(i)}} &= Dh \int_{-L/2}^{L/2} \int_{-\pi}^{\pi} [\mathscr{E}_D^{\mathrm{DMI(i)}} + \mathscr{E}_A^{\mathrm{DMI(i)}}] \sqrt{g} d\xi^1 d\xi^2 \\ &= Dh\, [E_D^{\mathrm{DMI(i)}} + E_A^{\mathrm{DMI(i)}}] \,, \end{aligned} \tag{A.19}$$

where $E_D^{\mathrm{DMI(i)}}$ and $E_A^{\mathrm{DMI(i)}}$ are the isotropic-like DMI and the DMI-driven curvature-induced anisotropy. The energy density of the first contribution $\mathscr{E}_D^{\mathrm{DMI(i)}}$ can be expressed as

$$\begin{aligned} \mathscr{E}_D^{\mathrm{DMI(i)}} &= D^{(i)} (m^3 \bar{\partial}_\alpha m^\alpha - m^\alpha \bar{\partial}_\alpha m^3) \\ &= m^3(\partial_1 m^1 + \partial_2 m^2 + \Gamma_{12} m^2) - m^1 \partial_1 m^3 + m^2 \partial_2 m^3 \,, \end{aligned} \tag{A.20}$$

which, after integration over the surface, gives the typical interfacial DMI energy contribution as

$$\begin{aligned} E_D^{\mathrm{DMI(i)}} &= 2\pi D^{(i)} \int_0^\infty \int_0^{2\pi} \left(m_z \frac{\partial m_\rho}{\partial\rho} + m_z \frac{m_\rho}{\rho} - m_\rho \frac{\partial m_z}{\partial\rho} \right) \rho\, d\rho\, d\chi \\ &= 2\pi D^{(i)} \int_0^\infty \left(\frac{\partial\Theta}{\partial\rho} + \frac{\sin\Theta\cos\Theta}{\rho} \right) \rho\, d\rho. \end{aligned} \tag{A.21}$$

The anisotropy-like energy density $\mathscr{E}_A^{\mathrm{DMI(i)}}$ is given by

$$\mathscr{E}_A^{\mathrm{DMI(i)}} = -D^{(i)} \mathscr{H} m_3 m^3, \tag{A.22}$$

which, after some algebra, is evaluated to give

$$\begin{aligned} E_A^{\mathrm{DMI(i)}} &= -\int_{-L/2}^{L/2} \int_{-\pi}^{\pi} \mathscr{H}(1 - \sin^2\Theta) \sqrt{g} d\xi^1 d\xi^2 \\ &= 2\pi\mathscr{H} \int_0^\infty \sin^2\Theta \rho d\rho - \mathbb{M} \,, \end{aligned} \tag{A.23}$$

where $\mathbb{M} = \int_{-L/2}^{L/2} \int_{-\pi}^{\pi} H(\xi^2) \sqrt{g}\, d\xi^1 d\xi^2$ is also a function of the curved surface, but does not depend on the skyrmion position.

Therefore, the complete expression of the interfacial DMI energy is

$$E^{\mathrm{DMI}(i)}(X^2) = 2\pi h D^{(i)} \left(C_2 + \frac{\mathscr{H} C_1}{2} - \frac{\mathbb{M}}{2\pi} \right). \tag{A.24}$$

Finally, the contribution of the uniaxial anisotropy to the skyrmion energy is given by

$$E^{\mathrm{an}} = 2\pi h K \int_0^{\infty} \sin^2 \Theta \rho d\rho, \tag{A.25}$$

where $K = K_u - \frac{\mu_0}{2} M_s^2$ is the effective anisotropy constant that takes into account the magnetostatic energy of a thin film. By summing eqs. (A.7), (A.9), (A.14), (A.21), (A.23), and (A.25), we obtain the total energy of the Néel skyrmion, given by

$$E^{(\mathrm{N})}(X^2) = 2\pi h \left[A \left(C_0 - \left\{ \frac{\mathscr{H}^2 - 2\mathscr{K}}{2} \right\} C_1 - \mathscr{H} C_2 + \frac{\mathbb{N}}{2\pi} \right) + D^{(i)} \left(C_2 + \frac{\mathscr{H} C_1}{2} - \frac{\mathbb{M}}{2\pi} \right) + K C_1 \right]. \tag{A.26}$$

For the Bloch skyrmion, $\Phi(\chi) = \chi + \pi$, so the derivatives are given by

$$\frac{\partial \boldsymbol{m}}{\partial \xi^1} = \begin{pmatrix} \frac{\partial m^1}{\partial \xi^1} \\ \frac{\partial m^2}{\partial \xi^1} \\ \frac{\partial m^3}{\partial \xi^1} \end{pmatrix} = \begin{pmatrix} -\frac{\partial \boldsymbol{m}_\rho}{\partial \rho} \sin\chi \cos\chi + \frac{m_\rho}{\rho} \sin\chi \cos\chi \\ \sqrt{\frac{g_{11}}{g_{22}}} \left(\frac{\partial \boldsymbol{m}_\rho}{\partial \rho} \cos^2\chi + \frac{m_\rho}{\rho} \sin^2\chi \right) \\ \sqrt{g_{11}} \frac{\partial \boldsymbol{m}_z}{\partial \rho} \cos\chi. \end{pmatrix} \tag{A.27}$$

$$\frac{\partial \boldsymbol{m}}{\partial \xi^2} = \begin{pmatrix} \frac{\partial m^1}{\partial \xi^2} \\ \frac{\partial m^2}{\partial \xi^2} \\ \frac{\partial m^3}{\partial \xi^2} \end{pmatrix} = \begin{pmatrix} \sqrt{\frac{g_{22}}{g_{11}}} \left(-\frac{\partial \boldsymbol{m}_\rho}{\partial \rho} \sin^2\chi - \frac{m_\rho}{\rho} \cos^2\chi \right) \\ \frac{\partial \boldsymbol{m}_\rho}{\partial \rho} \sin\chi \cos\chi - \frac{m_\rho}{\rho} \sin\chi \cos\chi \\ \sqrt{g_{22}} \frac{\partial \boldsymbol{m}_z}{\partial \rho} \sin\chi \end{pmatrix} \tag{A.28}$$

Under these derivatives, the energy term E_D^{X} vanishes. Moreover, $E_A^{\mathrm{DMI(b)}}$ is also zero due to the isotropic nature of the bulk DMI. Therefore, the total energy of the Bloch skyrmion is given by

$$E^{(\mathrm{B})}(X^2) = 2\pi t \left[A \left(C_0 - \left(\frac{\mathscr{H}^2 - 2\mathscr{K}}{2} \right) C_1 + \frac{\mathbb{N}}{2\pi} \right) + D^{(b)} C_2 + K C_1 \right]. \tag{A.29}$$

Appendix B

Calculation of the tensors for the generalized Thiele equation

The gyrotensor G_{ab} and the damping tensor D_{ab} approach their flat-film values [38].

Gyrotensor

$$\begin{aligned} G_{12} &= G \\ G_{21} &= -G, \end{aligned} \tag{B.1}$$

where $G = h\frac{M_s}{\gamma}4\pi N_{sk}$. Since $G_{11} = G_{22} = 0$, therefore

$$G_{ab} = \begin{pmatrix} 0 & G \\ -G & 0 \end{pmatrix}. \tag{B.2}$$

Damping tensor

$$D_{11} = D_{22} = h\,\frac{M_s\pi}{\gamma}\int_0^\infty \left[\left(\frac{\partial\Theta}{\partial r}\right)^2 + \frac{\sin^2\Theta}{r^2}\right] r\,dr. \tag{B.3}$$

Since the off-diagonal components vanish, $D_{12} = D_{21} = 0$, the damping tensor is diagonal.

$$D_{ab} = \begin{pmatrix} D_{11} & 0 \\ 0 & D_{22} \end{pmatrix} \tag{B.4}$$

$\boldsymbol{D^u_{ab}}$ **tensor**

$$D^{\mathrm{u}}_{ab} = \frac{\mu_0 M_s h}{\gamma}\int_S \Big[g_{\eta\gamma}\,\partial_a m^\eta\left(m^\omega\Gamma^\gamma_{\omega b} - m^3 b^\gamma_b\right) + m^\omega\,\partial_a m^3\,b_{b\omega}\Big]dS. \tag{B.5}$$

The tensor D^{u}_{ab} can be expressed as

$$D^u_{ab} = \begin{pmatrix} D^u_{11} & D^u_{12} \\ D^u_{21} & D^u_{22}. \end{pmatrix} \tag{B.6}$$

The individual components of D^{u}_{ab} are obtained by explicit evaluation of the surface integrals.

$$\begin{aligned} D^u_{11} = {} & h\frac{M_s}{\gamma}\int_0^\infty\int_0^{2\pi}\left[\frac{g_{11}}{\sqrt{g_{22}}}\left(\frac{\partial m_\rho}{\partial\rho}m_\rho\cos^2\chi\sin\chi + z\frac{m_\rho^2}{\rho}\sin^3\chi\right)\Gamma^1_{12}\right. \\ & - g_{11}\left(\frac{\partial m_\rho}{\partial\rho}m_z\cos^2\chi + \frac{m_\rho}{\rho}m_z\sin^2\chi\right)b^1_1 + \left(m_r\frac{\partial m_z}{\partial\rho}\cos^2\chi\right)b_{11} \\ & \left. + \frac{g_{22}}{\sqrt{g_{22}}}\left(\frac{\partial m_\rho}{\partial\rho}m_\rho\cos^2\chi\sin\chi - \frac{m_\rho^2}{\rho}\cos^2\chi\sin\chi\right)\Gamma^2_{11}\right]\rho\, d\rho d\chi \\ = {} & -h\frac{M_s\pi}{\gamma}b_{11}\int_0^\infty\left[\frac{\partial\Theta}{\partial\rho} + \frac{\sin\Theta\cos\Theta}{\rho}\right]\rho d\rho, \end{aligned} \tag{B.7}$$

and

$$D^u_{22} = -h\frac{M_s\pi}{\gamma}b_{22}\int_0^\infty\left[\frac{\partial\Theta}{\partial\rho} + \frac{\sin\Theta\cos\Theta}{\rho}\right]\rho d\rho \quad . \tag{B.8}$$

Due $D^u_{12} = D^u_{21} = 0$, therefore

$$D^u_{ij} = \begin{pmatrix} D^u_{11} & 0 \\ 0 & D^u_{22} \end{pmatrix} \tag{B.9}$$

$\boldsymbol{G^u_{ij}}$ tensor

$$G^u_{ab} = \frac{\mu_0 M_s h}{\gamma}\int_S \sqrt{g}\begin{vmatrix} m^1 & \partial_a m^1 & (m^\gamma\Gamma^1_{b\gamma} - m^3 b^1_b) \\ m^2 & \partial_a m^2 & (m^\gamma\Gamma^2_{b\gamma} - m^3 b^2_b) \\ m^3 & \partial_a m^3 & m^\gamma b_{b\gamma} \end{vmatrix} dS. \tag{B.10}$$

The tensor G^{u}_{ab} can be written as

$$G^{\mathrm{u}}_{ab} = \begin{pmatrix} G^u_{11} & G^u_{12} \\ G^u_{21} & G^u_{22} \end{pmatrix}, \tag{B.11}$$

whose individual components can be evaluated within the planar approximation.

$$\begin{aligned} G^u_{21} = {} & h\frac{M_s}{\gamma}\int_0^\infty\int_0^{2\pi}\left[\left(\frac{\partial m_\rho}{\partial\rho}m_z^2\sin^2\chi + m_z^2\frac{m_\rho}{\rho}\cos^2\chi - m_z m_\rho\frac{\partial m_z}{\partial\rho}\sin^2\chi\right)b^1_1\right. \\ & \left.\frac{b_{11}}{g_{11}}\frac{m_\rho^3}{\rho}\cos^2\chi\right]\rho\, d\rho d\chi \\ = {} & h\frac{M_s\pi}{\gamma}b^1_1\int_0^\infty\left[\cos\Theta\frac{\partial\Theta}{\partial\rho} + \frac{\sin\Theta}{\rho}\right]\rho d\rho \end{aligned} \tag{B.12}$$

$$G^u_{12} = h\frac{M_s}{\gamma}\pi b^2_2\int_0^\infty\left[\cos\Theta\frac{\partial\Theta}{\partial\rho} + \frac{\sin\Theta}{\rho}\right]\rho d\rho. \tag{B.13}$$

Since $G^u_{11} = G^u_{22} = 0$, therefore

$$G^u_{ij} = \begin{pmatrix} 0 & G^u_{12} \\ G^u_{21} & 0 \end{pmatrix}. \tag{B.14}$$

If a current is applied along the toroidal direction (i.e., $\boldsymbol{u} = (u^1, 0)$), the tensors defined in Eqs. (B.2), (B.4), (B.14), and (B.9) yield a coupled system of equations for a Néel skyrmion:

$$\begin{aligned} &G_{12}\dot{X}^2 + D_{11}(\beta u^1 - \alpha \dot{X}^1)u^1\beta D^u_{11} = 0 \\ &G_{21}(\dot{X}^1 - u^1) - \alpha D_{22}\dot{X}^2 - u^1 G^u_{21} = \frac{\partial E}{\partial X^2}. \end{aligned} \tag{B.15}$$

Finally, the toroidal $\dot{X}^1$ and poloidal $\dot{X}^2$ components of the Néel skyrmion velocity are given by

$$\dot{X}^1 = \frac{G(G - G^{\mathrm{u}}_{21}) + \alpha\beta D(D + D^u_{11})}{\alpha^2 D^2 + G^2} u^1 - \frac{G}{\alpha^2 D^2 + G^2}\frac{\partial E}{\partial X^2} \tag{B.16}$$

$$\dot{X}^2 = \frac{\alpha D(G - G^u_{21}) - \beta G(D + D^u_{11})}{\alpha^2 D^2 + G^2} u^1 - \frac{\alpha D}{\alpha^2 D^2 + G^2}\frac{\partial E}{\partial X^2}. \tag{B.17}$$

For a Bloch skyrmion, the dissipative and gyroscopic tensors coincide with those of the Néel skyrmion. However, the curvature-induced contributions encoded in the tensors G^{u}_{ab} and D^{u}_{ab} differ, specifically in the placement of their diagonal elements.

D^u_{ab} tensor for a Bloch skyrmion

$$\begin{aligned} D^{\mathrm{u}}_{12} &= \frac{\pi\mu_0 M_s h}{\gamma} \int_0^\infty \int_0^{2\pi} \left[\sqrt{\frac{g_{11}}{g_{22}}} \left(\frac{\partial m_\rho}{\partial_\rho}\cos^2\chi + \frac{m_\rho}{\rho}\sin^2\chi\right) m_z b_{22}\right] \rho \, d\rho d\chi \\ &= \frac{\pi\mu_0 M_s h}{\gamma}\, b^2_2 \int_0^\infty \left[\frac{\partial\Theta}{\partial\rho} + \frac{\sin\Theta\cos\Theta}{\rho}\right] \rho d\rho, \end{aligned} \tag{B.18}$$

$$D^{\mathrm{cnAD}}_{21} = \frac{\pi\mu_0 M_s t}{\gamma}\, b^1_1 \int_0^\infty \left[\frac{\partial\Theta}{\partial\rho} + \frac{\sin\Theta\cos\Theta}{\rho}\right] \rho d\rho, \tag{B.19}$$

$$D^{\mathrm{u}}_{ab} = \begin{pmatrix} 0 & D^{\mathrm{u}}_{12} \\ D^{\mathrm{u}}_{21} & 0 \end{pmatrix}. \tag{B.20}$$

G^u_{ab} tensor for a Bloch skyrmion

$$\begin{aligned}
G^{\mathrm{u}}_{11} &= \frac{\mu_0 M_s h}{\gamma}\int_0^{\infty}\int_0^{2\pi}\frac{b_{11}}{\sqrt{g_{11}g_{22}}}\left[\frac{m_\rho^3}{\rho}\sin^2\chi - \frac{\partial m_\rho}{\partial_\rho}m_z m_\rho\cos^2\chi\right. \\
&\qquad \left. + m_z^2\frac{\partial m_\rho}{\partial_\rho}\cos^2\chi + m_z^2\frac{m_\rho}{\rho}\sin^2\chi\right]\rho\; d\rho d\chi \\
&= \frac{\pi\mu_0 M_s h}{\gamma}b_{11}\int_0^{\infty}\left[\cos\Theta\frac{\partial\Theta}{\partial\rho} + \frac{\sin\Theta}{\rho}\right]\rho d\rho,
\end{aligned} \tag{B.21}$$

$$G^{\mathrm{u}}_{22} = \frac{\pi\mu_0 M_s h}{\gamma}b_{22}\int_0^{\infty}\left[\cos\Theta\frac{\partial\Theta}{\partial\rho} + \frac{\sin\Theta}{\rho}\right]\rho d\rho, \tag{B.22}$$

$$G^{\mathrm{u}}_{ab} = \begin{pmatrix} G^{\mathrm{u}}_{11} & 0 \\ 0 & G^{\mathrm{u}}_{22} \end{pmatrix}. \tag{B.23}$$

This lead to a system of equations for a Bloch skyrmion, given by

$$\begin{aligned}
G\dot{X}^2 + D(\alpha\dot{X}^1 - \beta u^1) - u^1\beta D^{\mathrm{u}} &= 0, \\
-G(\dot{X}^1 - u^1) + D\alpha\dot{X}^2 - u^1\beta D^{\mathrm{u}}_{21} &= \frac{\partial E^{(b)}}{\partial X^2}.
\end{aligned} \tag{B.24}$$

Accordingly, the velocity components of the Bloch skyrmion in a bent nanotube, $\dot{X}^1$ and $\dot{X}^2$, read

$$\dot{X}^1 = \frac{\alpha D(\beta D + \alpha G^{\mathrm{u}}_{11}) - G(G + \beta D^{\mathrm{u}}_{21})}{\alpha^2 D^2 + G^2}u^1 - \frac{G}{\alpha^2 D^2 + G^2}\frac{\partial E^{(b)}}{\partial X^2}, \tag{B.25}$$

$$\dot{X}^2 = \frac{\alpha D(G + \beta D^{\mathrm{u}}_{21}) + G(\beta D + \alpha G^{\mathrm{u}}_{11})}{\alpha^2 D^2 + G^2}u^1 + \frac{\alpha D}{\alpha^2 D^2 + G^2}\frac{\partial E^{(b)}}{\partial X^2}. \tag{B.26}$$